Università
degli Studi
di Ferrara

DOCTORAL COURSE IN PHYSICS

CYCLE XXXIII

DIRECTOR
Prof. Eleonora Luppi

Maxwell-Boltzmann-like neutron spectrum production for Maxwellian averaged cross section measurement

Scientific/Disciplinary Sector (SDS) FIS/04

Supervisor
Prof. Diego Bettoni

(signature)

Candidate
Dott. Musacchio González Elizabeth

(signature)

Co-Supervisor
Dott. Pierfrancesco Mastinu

(signature)

Years 2017/2020

To my family!

Abstract

In the Universe, the observed elements heavier than iron (Fe) are mostly produced by neutron-capture processes in the stars. These processes are defined as s (slow) and r (rapid) processes. The experimental measurement of the neutron capture cross sections is an actively working task, since it is an essential element in the stellar reaction rates calculations and thus, the possibility of reproducing the observed abundance of the elements in the universe. In stellar interiors, the plasma is in thermodynamic equilibrium and the particle velocities are described by a Maxwell–Boltzmann distribution. To calculate the reaction rate in the neutron capture processes it is common to work with the Maxwellian Averaged Cross Section (MACS). This parameter is defined as the reaction rate scaled by the most probable velocity of the Maxwell–Boltzmann distribution. For the s-process, the MACS directly describes the reaction rate inside the stars, for a given temperature and neutron density. Hence, the importance of determining the MACS with the least possible uncertainty. A very accurate and direct MACS measurement, under certain conditions, can be performed by neutron activation analysis providing a neutron beam with the stellar spectrum i.e., a Maxwell-Boltzmann neutron spectrum (MBNS). Before any MACS measurement, a characterized neutron beam with a stellar spectrum is mandatory, and this is the main purpose of this work.

The ^{7}Li(p,n)^{7}Be nuclear reaction is employed as neutron source. In the experimental measurement, neutron time-of-flight spectrometry (nTOF) was implemented to determine the neutron spectrum, using a 600 kHz proton pulsed beam at the Van de Graaff accelerator of the Legnaro National Laboratory of the National Institute of Physics Nuclear (LNL-INFN), in Padua, Italy.

A new approach to transform TOF spectra into energy spectra was implemented, using the detector response matrix. The proposed conversion method considers not only the mean moderation time of neutrons in the detector, but also its distribution in time. Simulations with MCNPX code to validate the conversion method were performed. For the same purpose, the neutron TOF spectrum at zero degrees with 1912 keV proton energies was measured. The measured TOF spectrum was converted using the proposed method, and the obtained neutron energy spectrum compared with other experimental data found in the literature.

In order to measure directly the MACS with the activation method, a MBNS must be produced, as far as similar to the theoretical Maxwell–Boltzmann distribution. Mastinu *et al.* (2009) proposed a method to produce a high-quality Maxwell-Boltzmann neutron spectrum at different thermal temperatures (kT). The method is based on the idea of "shaping the proton beam energy distribution to shape the neutron energy beam to a desired distribution". This method avoids the use of moderators. In this thesis, the expected MBNS has been measured and the obtained results are reported.

To obtain a well reproduced MBNS with 30 keV of thermal temperature, an initial proton energy of 3170 keV and a 50 μm thickness aluminum (Al) foil, as proton energy shaper, were employed. Differential angular neutron energy distribution from 0 to 90 degrees in steps of 10° were measured in order to obtain the 0°-90° integrated neutron spectra. Four Li-glass detectors were employed, placed at a 50 cm from the lithium target. The emitted neutron energy spectrum was experimentally obtained applying the proposed conversion method using the response matrix of the Li-glass detector.

Keywords: MACS, cross section, nTOF, neutron spectrum, Time-of-Flight, MCNPX.

Riassunto

Nell'Universo, gli elementi osservati più pesanti del ferro (Fe) sono principalmente prodotti mediante processi di cattura neutronica nelle stelle. Questi possono essere processi-s, lenti, o processi-r, veloci. La misura sperimentale della sezione d'urto di cattura neutronica è un compito su cui si lavora attivamente, dal momento che rappresenta un elemento essenziale per il calcolo delle velocità di reazione stellare e quindi per la possibilità di riprodurre l'abbondanza degli elementi osservata nell'universo. All'interno delle stelle, il plasma si trova in equilibrio termodinamico e le velocità delle particelle sono descritte da una distribuzione di tipo Maxwell–Boltzmann (MB). Per calcolare la velocità di reazione nei processi di cattura neutronica si lavora solitamente con la Maxwellian Averaged Cross Section (MACS). Questo parametro è definito come la velocità di reazione scalata per la più probabile velocità della distribuzione MB. Soprattutto per i processi-s, la MACS descrive direttamente la velocità di reazione all'interno delle stelle, date una certa temperatura e una certa densità neutronica. Da qui, l'importanza di determinare la MACS con la minore incertezza possibile. Una misura diretta e molto accurata della MACS, in certe condizioni, può essere ottenuta da un'analisi di attivazione neutronica, attraverso un fascio neutronico con lo spettro stellare, ovvero un Maxwell-Boltzmann neutron spectrum (MBNS). Prima di qualsiasi misurazione di MACS, è necessario caratterizzare un fascio neutronico con uno spettro stellare, e ciò è proprio l'obiettivo del presente lavoro.

Come sorgente neutronica è stata utilizzata la reazione ^{7}Li(p,n)^{7}Be. Nelle misure sperimentali è stata implementata la spettrometria del tempo di volo neutronico (nTOF) per determinare lo spettro neutronico, utilizzando un fascio protonico pulsato da 600 kHz all'acceleratore di Van de Graaff dei Laboratori Nazionali di Legnaro dell'Istituto Nazionale di Fisica Nucleare (LNL-INFN), a Padova, Italia.

È stato sviluppato un nuovo approccio per trasformare gli spettri TOF in spettri in energia, utilizzando la matrice di risposta del rivelatore. Il metodo di conversione proposto non solo considera il tempo medio di moderazione nel rivelatore, ma anche la sua distribuzione nel tempo. Sono state eseguite simulazioni con il codice MCNPX per validare il metodo di conversione. Analogamente, è stato misurato lo spettro TOF neutronico a zero gradi con un'energia di fascio protonico pari a 1912 keV. Lo spettro TOF misurato è stato quindi convertito utilizzando il metodo proposto, e lo spettro neutronico in energia così ottenuto è stato confrontato con dati sperimentali presenti in letteratura. Per misurare direttamente la MACS con il metodo di attivazione, è necessario produrre un MBNS il più simile possibile alla distribuzione teorica di Maxwell-Boltzmann. Mastinu *et al.* (2009) ha proposto un metodo per produrre un MBNS di alta qualità, a differenti temperature termiche (kT). Il metodo è basato sull'idea di "modellare la distribuzione dell'energia del fascio protonico per modellare l'energia del fascio neutronico con una distribuzione desiderata". Con questo metodo si evita l'utilizzo di moderatori. Nel presente lavoro di tesi è stato misurato il MBNS atteso e sono quindi riportati i risultati ottenuti

Per ottenere un MBNS con una kT di 30 keV, è stata utilizzata un'energia inziale di fascio protonico pari a 3170 keV e un foglio di alluminio (Al) con uno spessore di 50 μm come modellatore dell'energia del fascio. La distribuzione angolare differenziale dell'energia dei neutroni da 0 a 90 gradi in step di 10° è stata misurata per ottenere lo spettro neutronico integrato da 0°-90°. Sono stati impiegati quattro rivelatori Li-glass, posizionati a 50 cm dal target in litio. Lo spettro neutronico in energia emesso è stato quindi ottenuto applicando il metodo di conversione proposto, utilizzando la matrice di risposta del rivelatore.

Parole chiavi: MACS, cross section, nTOF, neutron spectrum, Time-of-Flight, MCNPX.

Contents

Acknowledgements

Bibliography

List of Figures

List of Tables

Acronyms

ABNS Accelerator-Based Neutron Sources

AGB stars Asymptotic Giant Branch Stars

BBN Big Bang Nucleosynthesis

CANS Compact Accelerator-Driven Neutron Source

CERN European Organization for Nuclear Research

CFD Constant Fraction Discriminator

CLiP Cosmological Lithium Problem

CM Center-of-Mass System

CNA Centro Nacional de Aceleradores

CoMPASS CAEN Multi-Parameter Spectroscopy Software

DAQ Data Acquisition System

EXFOR Experimental Nuclear Reaction Data

FPGA Field-Programmable Gate Array

FWHM Full Width Half Maximum

GELINA Geel Electron Linear Accelerator

H-R diagram Hertzsprung-Russell Diagram

HISPANos HiSPAlis Neutron Source

HPGe High Purity Germanium

IAEA International Atomic Energy Agency

ILL Institut Laue-Langevin

JRC Joint Research Centre

KADoNiS Karlsruhe Astrophysical Database of Nucleosynthesis in Stars

LNL-INFN Legnaro National Laboratory of the Italian Institute of Nuclear Physics

MACS Maxwellian-Averaged Cross Section
MBNS Maxwell-Boltzmann Neutron Spectrum
MCNPX Monte Carlo N Particle

nTOF Neutron Time-of-Flight

PMT Photomultiplier Tube
PS Proton Synchrotron
PSD Pulse Shape Discrimination
pTOF Proton Time-of-Flight

RF Radio-Frequency
RGB Red Giant Branch
RMS Root Mean Square

SEM Scanning Electron Microscope
SRIM 2013 Stopping Power and Range of Ions in Matter

TOF Time-of-Flight

Chapter 1

Scientific motivation

1.1 Nuclear Astrophysics

Nuclear astrophysics constitutes a multidisciplinary field of knowledge that combines the achievements from theoretical astrophysics, observational astronomy, cosmo-chemistry and nuclear physics [1]. Nuclear astrophysics, in essence, is a science that attempts to understand and explain the origin of the elements in the Universe and looks for the connection between properties of atomic nuclei and the properties of planets, stars, and galaxies.

Nuclear astrophysics aims to answer some fundamental questions [2], such as:

- How can the Sun and the stars keep shining for billions of years?
- What is the origin of elements in the Universe?
- How do the nuclei formed by nucleosynthesis get dispersed into space?
- How are the heaviest chemical elements formed, such as gold, platinum and lead?

One of the earliest attempts to explain the origin of the elements was proposed by George Gamow in 1948 (the original paper was authored by Alpher, Bethe and Gamow [3] and is known as the $\alpha\beta\gamma$ paper). Here, it was speculated that all elements could be produced during the early stages of the Big Bang, through successive neutron or proton captures and photon emissions. It was not until 1957 that a more plausible explanation was put forward by Burbidge, Burbidge, Fowler and Hoyle [4] (also known as the $\mathrm{B}^2\mathrm{FH}$ paper). Their work laid the bases for the stellar nucleosynthesis theory. The authors proposed that all nuclei were produced in stars, indicated the cycles and processes, and accounted for the relative abundances observed at that time [5].

Work in nuclear astrophysics implies: (1) astronomical observations using telescopes, gravitational wave detectors, and neutrino detectors; (2) accelerator laboratory experiments using beams of stable nuclei, radioactive nuclei, neutrons, and gamma-rays; (3) laboratory analysis of interstellar grains; (4) large scale computer simulations of stellar explosions and nuclei; and (5) theoretical work in nuclear physics and astrophysics.

We now understand that nuclear processes, operating both in the early universe and in stars, are responsible for the synthesis of the elements. Over the past quarter century, impressive progress has been made in the various fields related to nuclear astrophysics. The fast development of experimental and theoretical nuclear physics, as well as in ground-based or space astronomical observations and modellings, have made possible accurate determinations of the elemental and isotopic abundances in many astronomical environments. Such studies impose increasingly stringent constraints on models of stellar evolution and nucleosynthesis and help to identify critical areas in which nuclear physics input is essential [6].

1.2 Nomenclature

Atomic nuclei consist of protons and neutrons. The symbol Z is called atomic number and denotes the number of protons inside the nucleus. The number of neutrons is denoted by the symbol N. The mass number A (sometimes also referred to as nucleon number) is defined by the quantity $A = Z + N$. Nuclei with the same number of protons and number of neutrons have the same mass and are represented as ${}^{A}_{Z}X_{N}$, where X is the element symbol. Any individual nuclear species is called a *nuclide*. Isotopes are defined as nuclides with the same number of protons, but different number of neutrons (and hence a different mass number). Isotones are defined as nuclides with the same number of neutrons, but with different number of protons. Nuclides of the same mass number, but with different numbers of protons and neutrons are called isobars. The nuclear physics properties of isotopes, isobars, and isotones are different since they have different numbers of protons or neutrons.

The chart of nuclides is a two-dimensional diagram that represents the currently existing nuclides. The number of neutrons and protons are displayed on the horizontal and vertical axes, respectively. Each square represents a different nuclide with unique nuclear physics properties. Figure 1.1 displays a section of the nuclides chart, the lightest species with $Z \leq 8$ and $N \leq 16$. The black squares represent

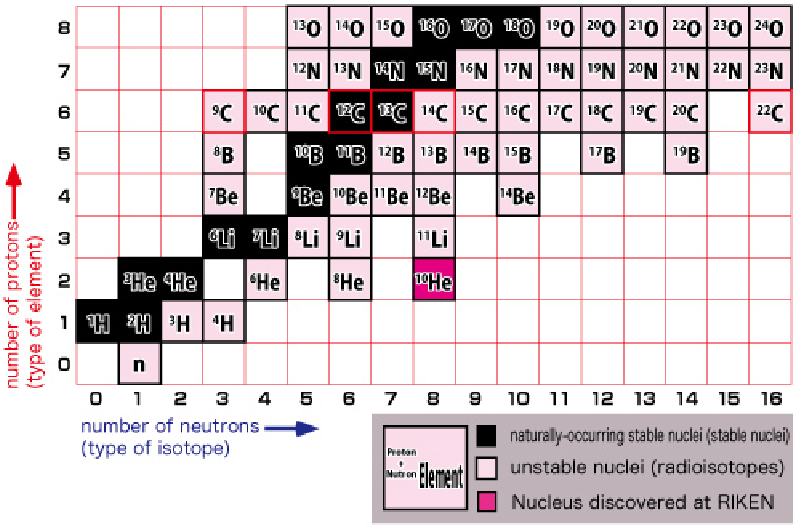

Figure 1.1: Section of the nuclides chart, the lightest species with $Z \leq 8$ and $N \leq 16$ [7].

stable nuclides, while the light pink squares correspond to the unstable ones. In nature, there are many more unstable than stable nuclides.

The binding energy $B(Z,N)$ of a nucleus is defined as the energy required to break it up into the A individual nucleons. For a nucleus made of Z protons and N neutrons, and with mass $M(Z,N)$, the binding energy is defined by:

$$B(Z,N) = N\ m_n\ c^2 + Z\ m_p\ c^2 - M(Z,N)\ c^2 \tag{1.1}$$

where m_n and m_p are the neutron and proton mass, respectively. The nuclear force makes the mass of the nucleus smaller than the sum of the individual nucleon masses. The binding energy per nucleon ($B(Z,N)/A$) is shown in Figure 1.2. In the low mass region, ^{4}He is strongly bound, usually referred as the α particle. This high binding energy explains why the $\alpha + p$ and $\alpha + \alpha$ systems (^{5}Li and ^{8}Be) are unstable: they immediately breakup. Iron is the most tightly bound nucleus, with a binding energy per nucleons of 8.8 MeV for the ^{56}Fe isotope. For $A < 56$, energy is released by increasing the mass (by capturing a nucleon or an α particle). This is the origin of fusion reactions occurring in stars and in fusion reactors. In contrast, for $A > 56$, nuclei increase their binding energy (or, equivalently, reduce their mass) by emitting particles. Spontaneous fission occurs in the uranium region ($A \approx 200$ and above).

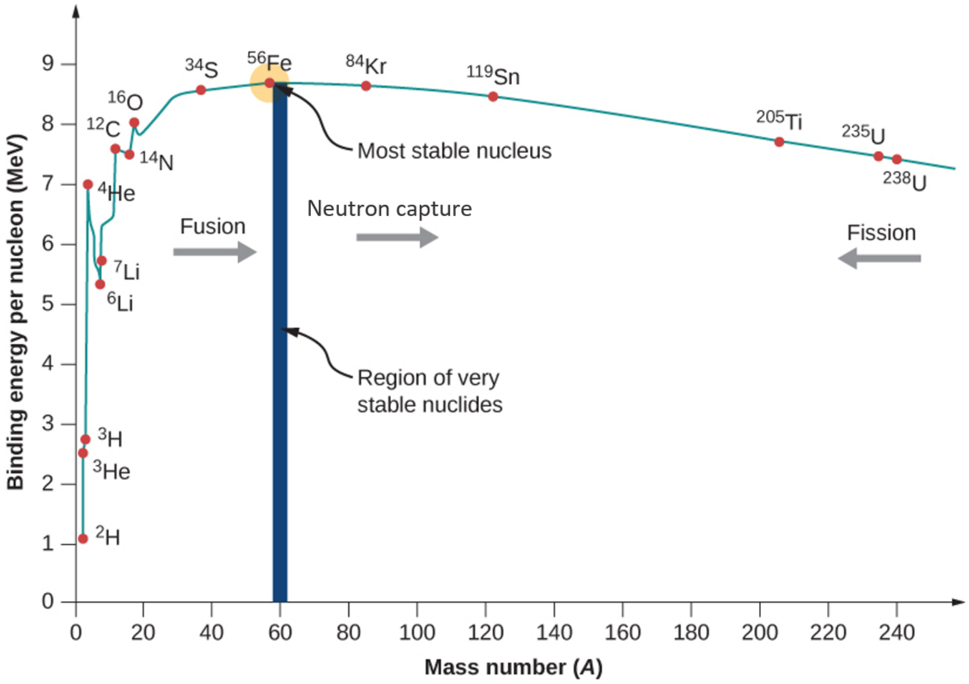

Figure 1.2: Binding energy per nucleon for stable nuclei [8].

1.3 Solar System Abundances

The theory of nucleosynthesis aims to explain the vast difference in the abundances of chemical elements and their several isotopes from the perspective of natural processes. The solar system chemical elements abundances are referred to the abundance distribution in the solar system at the time of its formation. The two main sources for studying the elemental abundance of the solar system are: (1) observations of the solar photosphere, and (2) analysis of a specific class of meteorites. The Sun contains most of the mass in the solar system and, therefore, it is representative of its overall composition [9].

The isotopic abundance distribution in the solar system is shown in Figure 1.3. This chart distribution was built from measurements and observations and presents some interesting features. On this scale, silicon (Si) is taken as the arbitrary benchmark, with an isotopic abundance value of a million, and abundances for the rest of compounds are normalized to the number of Si atoms. In particular, the most abundant species in the solar system are hydrogen (H) (71.1%) and helium (He) (27.4%). The abundances generally decrease when the mass number A increases. Exceptions to this behavior include the light elements lithium (Li), beryllium (Be) and boron (B), which are extremely underabundant in comparison

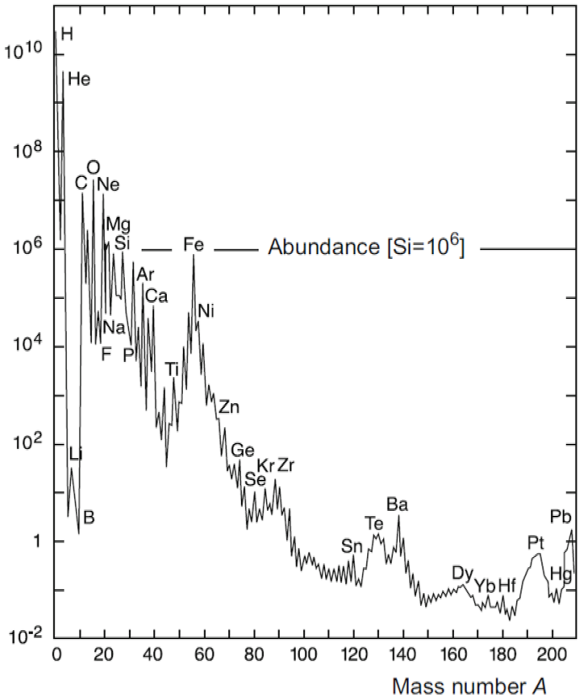

Figure 1.3: Isotopic abundance distribution in the solar system [11].

with the neighboring elements. On the top of this decrease there is a pronounced peak near iron (Fe) and several noticeable maxima in the region of A$\gtrsim$ 100. The reasons for favoring the presence of some species and for the specific pattern of abundances inferred for the solar system have spawned large debates.

It is reasonable to assume that the abundances within any group of nuclides can be primarily attributed to a specific mechanism of nucleosynthesis. Starting with the work of Suess and Urey [10], such values of solar system abundances had an enormous influence on studies of the origin of the elements and the development of nuclear astrophysics. All nuclides, with few exceptions, are synthesized in stars. Therefore, the observed solar system abundances offer powerful clues to stellar evolution and history, and by extension, to the chemical evolution of the galaxy as a whole [9].

1.4 Nucleosynthesis process and stellar evolution

1.4.1 Primordial nucleosynthesis

Our universe is thought to have formed about 14 billion years ago, with the Big Bang. The initial state was extremely dense and hot, followed by rapid expansion and cooling [6].

In the first stage relativistic particle–antiparticle pairs were created and destroyed in continuous collisions, constituting what is called today the quark–gluon plasma. Experiments in particle accelerators are helping us to understand the physics in this primordial hot stage of the universe.

The era of nuclear physics began after a microsecond (10^{-6} sec) where a soup of quarks and gluons condensed into protons and neutrons. After one second, things have cooled down enough so that elements like hydrogen can exist in some form. After another 10 seconds, the lightest nuclei could form isotopes of H, He, and a very small amount of Li. These nuclei are the ashes of the earliest element forming processes, which begin with nuclear reactions among the nuclei of these three elements. Analysis of the relative abundances of these light nuclei proves that there was an earlier state in time where temperature was over ten billion degrees [2].

Primordial nucleosynthesis, also known as Big Bang Nucleosynthesis (BBN), is believed by most cosmologists to have taken place in the interval from roughly 10 seconds to 20 minutes after the Big Bang [12]. The universe cooling below the minimal temperature threshold for fusion ended this period. Once the universe got too cold, its composition got frozen out and stopped moving. This is why deuterium can be found in interstellar space, primordial ^{4}He can be observed in the older stars and galaxies, and ^{7}Li can be observed at the surface of the oldest stars [2].

Nucleosynthesis in the Big Bang involves sequences of nuclear reactions among all the light nuclei. More accurate cross sections are needed for a number of these reactions to improve the accuracy of predicted element production in the Big Bang. For deuterium synthesis the required cross sections are: d(d,n)^{3}He, d(p,γ)^{3}He, d(d,p)^{3}H and p(n,γ)d. For ^{7}Li synthesis important reactions (in addition to those for deuterium) are: ^{3}He(^{4}He,γ)^{7}Be, ^{7}Li(p,n)^{7}Be and ^{3}He(d,p)^{4}He. We are now entering a period in which more precise predictions of BBN will be needed, presenting a real challenge to nuclear astrophysicists. The temperatures involved are sufficiently high that cross section measurements are usually performed over the entire relevant energy range, which varies from tens of keV to hundreds of keV. Such energies are available at a variety of modern experimental facilities [6].

The BBN primordial abundances predictions of hydrogen (^{1}H and ^{2}H) and helium (^{3}He and ^{4}He) are consistent with the inferred abundance from observational data. However, the BBN theory overestimates the primordial ^{7}Li abundance by a factor of three. Attempts to resolve these discrepancies using conventional nuclear physics and astrophysics have not been successful over the past few decades. This is referred in the literature as Cosmological Lithium Problem (CLiP). Several mechanisms have been put forward to explain the difference between calculations and observations:

the presence of non-canonical mixing processes in old stars, new physics beyond the standard model, errors in the inferred primordial ^{7}Li abundance and, finally, systematic uncertainties in the nuclear physics used in the BBN calculations, in particular for reactions leading to the destruction of ^{7}Be. Recent ^{7}Be(n,p)^{7}Li reaction cross section measurements exclude the possibility of an incorrect cross section as a cause for the CLiP, as reported in the work of Martín-Hernández *et al.* [13]. To investigate a possible nuclear physics solution to the CLiP, two measurements of (n,α) and (n,p) cross sections were made at n_TOF facility [14, 15]. The measured cross section lead to a minor correction of the lithium yield, thus yielding only a relatively minor improvement on the CLiP. This two neutron time-of-flight (nTOF) measurements finally exclude neutron-induced reactions, and possibly nuclear physics, as a potential explanation of the CLiP. Thus, the solution of this problem is still open [15].

1.4.2 Stellar nucleosynthesis and evolution

After about 200000 years, the primordial nuclei and electrons combined at a temperature of several thousand kelvins (K). It marked the beginning of the period in which density fluctuations could begin to grow rapidly, leading to the galaxies and clusters of galaxies that we observe today [6].

In contrast with the primordial nucleosynthesis, stellar nucleosynthesis determines the long term, slow evolution of stars, and refers to the creation of chemical elements by nuclear fusion reactions within stars. The Hertzsprung-Russell diagram (H-R diagram) is an important tool in the study of stellar evolution. The H-R diagram, shown in Figure 1.4, plots the absolute magnitudes of stars versus their spectral type (or alternatively, stellar luminosity against effective temperature). The stellar surface properties change over time, as their positions on the H-R diagram change. In the theory of stellar structure and evolution, one of the most important goals is to understand how stars produce energy synthesizing new elements and how they are injected into the interstellar medium.

The key quantity that determines how a star evolves is its mass, as it reaches the main sequence. Stars are born out of the gravitational collapse of cool and dense molecular clouds. As the cloud collapses, it fragments into smaller regions that contract to form stellar cores (protostars). The central temperature of the protostar increases to the point where nuclear reactions begin. At this point, H is converted into He in the core and the star is born onto the main sequence. For about 90% of its life, the star will continue burning H into He and will remain a main sequence star. Once the H in the core has all been burned to He, energy generation stops and the

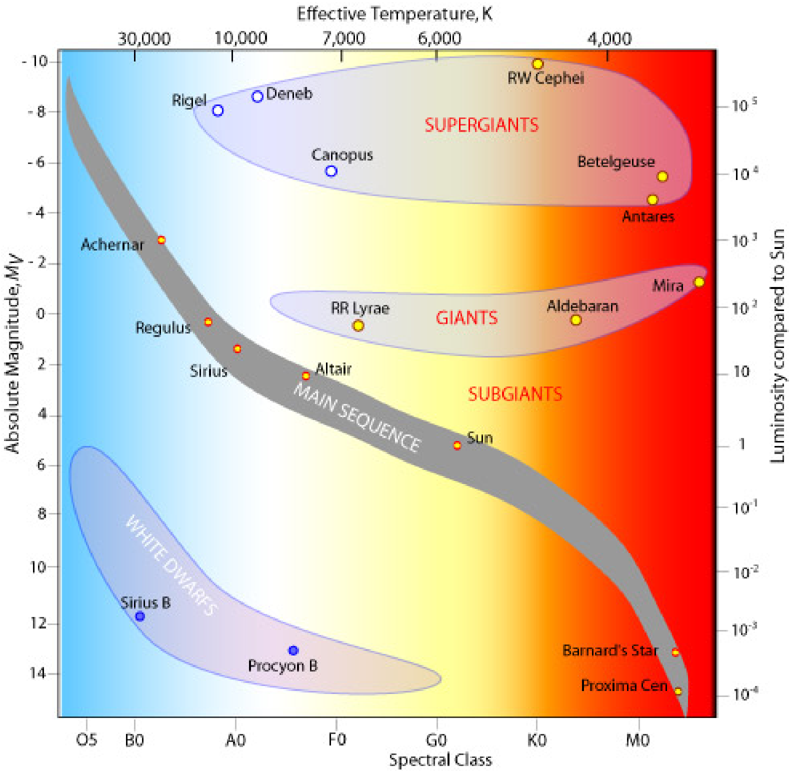

Figure 1.4: Hertzsprung-Russell diagram (H-R diagram). Absolute magnitude of stars against their spectral type (or alternatively, stellar luminosity versus effective temperature) [17].

core begins to contract. Meanwhile, the He core continues to contract and increase in temperature, increasing the energy generation rate in the H shell. This causes the star to expand enormously and to increase in luminosity. At this point, the star becomes a red giant branch (RGB). Eventually, the core reaches temperatures high enough to start a new nucleosynthesis process: the He fusion (burn) into carbon (C), known as *He burning process* [16].

For non massive stars (mass less than 8 solar masses), the inert C core continues to contract but it never reaches the sufficient temperature to initiate C burning. However, the existence of two burning shells leads to a thermally unstable situation in which H and He burning occurs out of phase with each other. This thermal pulsing is characteristic of asymptotic giant branch stars (AGB stars). In massive stars (mass greater than 8 solar masses), the contracting core will reach the temperature for C ignition, and the *carbon burning* process starts. This process of core burning followed by core contraction and shell burning, is repeated in a series of nuclear reactions producing successively heavier elements, until iron (Fe) is formed in the core. The strong electrostatic repulsion for nuclei heavier than silicon (Si) makes their fusion difficult, and in each forward step higher temperatures are required. Iron (Fe) cannot be burned to heavier elements as this reaction does not generate energy, it requires an input of energy to proceed (Equation 1.1). The star has therefore finally run out of fuel and collapses under its own gravity. The mass of the core of the star dictates what happens next. In the first case, the core becomes a neutron star, where the sudden halt in the contraction of the core produces a shock wave. This wave propagates back out through the outer layers of the star, blowing it apart in a core-collapse supernova explosion. The ejected gas expands into the interstellar medium, enriching it with all the elements synthesized during the star's lifetime and in the explosion itself. In the second case, even neutron pressure is not sufficient to withstand gravity, and it will collapse further into a stellar black hole.

1.4.3 Nucleosynthesis above iron: slow, fast and proton-processes

Nuclei from carbon to iron were found to be produced by charged particle reactions during the evolutionary phases from stellar He to Si burning. Around iron the Coulomb barrier through which the charged particles have to penetrate becomes rather large and the nucleosynthesis cannot proceed further by charged-particle capture reactions. To explain the existence of elements heavier than iron, processes different than fusion occur, as neutron captures, photo-disintegrations and fission processes, triggering the nucleosynthesis of heavy elements through the so called s (slow), r (fast) and p (proton) processes.

The chemical elements are constantly formed in stars. This fact was observed in 1952, when Paul Merril examined the light given off by red giant stars and found that that they were rich in technetium (Tc) (the spectrum was compatible with the presence of ^{99}Tc, which has a lifetime of about 200000 years). Such a discovery suggested that either (1) an unknown stable isotope exists, (2) that the stars were formed only a short time ago, or (3) that such stars generate Tc in the course of stellar evolution. Theoretical models did not predict the existence of a stable isotope in agreement with the experimental evidence for the known isotopes. Therefore, this could only mean that this element was being formed within the star itself [18].

The s and r-processes are responsible for the production of most of the heavy elements, and are characterized by successive neutron captures (type reactions (n,γ)) followed by β decays. The observed abundances of the elements and their isotopes in our solar system suggest that these processes take place at different characteristic time scales, temperatures, and neutron densities [6].

The s-process, which takes place during He (and eventually carbon) burning, is characterized by comparably low neutron densities, typically a few times 10^7 cm^{-3}. In the s-process the neutron capture times are much slower than most β decay times. This implies that the reaction path of the s-process follows the stability valley as sketched in Figure 1.5.

The s-process is believed to occur mostly in asymptotic giant branch stars (AGB stars), seeded by iron nuclei left by a supernova during a previous generation of stars. In contrast to the r-process which is believed to occur over time scales of seconds in explosive environments, the s-process is believed to occur over time scales of thousands of years, passing decades between neutron captures. The potential stellar neutron source for the s-process is associated with alpha particle capture reactions on light nuclei. While the ^{13}C(α,n)^{16}O is the major neutron source in AGB stars stars, the ^{22}Ne(α,n)^{25}Mg provides the neutrons for the synthesis of lighter species (from zinc (Zn) to strontium (Sr)) in massive stars.

On the other hand, the r-process takes place in an environment of high temperature, exceeding 10^9 K, and high neutron density, larger than 10^{20} cm^{-3}, in an event lasting a few seconds. The identification of stellar environments hosting the r-process is still a very debated topic, being neutron star mergers the only confirmed site (other potential sites are magneto-rotation driven supernovae and collapsars). There, neutron captures are much faster than β decays. The r-process allows the synthesis of isotopes very far from the beta stability valley, up to the neutron drip line.

The s-process is more easily accessible to laboratory experiments. Moreover, its

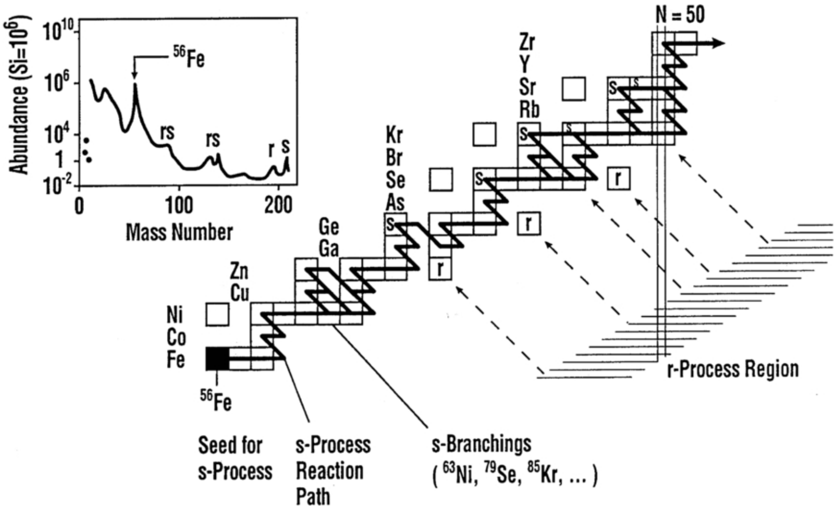

Figure 1.5: Neutron capture processes responsible for the formation of the nuclei between iron and the actinides [19].

modelling results less complicated respect to the r-process. Attempts to describe the r-process are hampered by the problems related to a detailed modelling of compact object mergers and stellar explosions. Moreover, the r-process requires the knowledge of nuclear properties of many unstable isotopes, which are difficult to be measured in laboratory. Obviously most isotopes received abundance contributions from both the s and the r-process. Moreover, there are neutron rich stable isotopes (marked as r in Figure 1.5) that are not reached by the s-process because of their short lived neighbors. Consequently, these species are almost of pure r-process origin. On the other hand, there exist isotopes, the so-called s-only isotopes, which do not receive any r-process contribution, because they are shielded by stable isobars. These isotopes, marked with s in Figure 1.5, are extremely useful tools to calibrate the s-process nucleosynthesis.

There are about 30 relatively neutron deficient nuclides with mass numbers of $A \geqslant 74$ (between ^{74}Se and ^{196}Hg) that cannot be synthesized by any of the known neutron capture processes. These species are called p nuclei, lie on the proton rich side of the valley of stability, and they all contain more protons relative to other stable isotopes of the same element. It turns out that the p nuclei are the rarest among the stable nuclides. The mechanism responsible for the synthesis of the p-nuclei is called the p-process [1].

1.5 Stellar cross sections

1.5.1 Neutron capture reactions

In neutron collisions with the atomic nuclei, a variety of nuclear reactions, depending on the neutron energy, can be produced. Generally, a distinction is made between the scattering processes (a neutron makes an elastic or inelastic collision with the nucleus) and absorption processes (a neutron disappears into the nucleus and various secondary radiations appear). The following two types of reactions can occur: *compound nucleus reactions* and *direct reactions.*

In direct reactions, the incident neutron interacts with some of the nucleons in a single quick event (10^{-21} seconds). By far, the most important direct reaction is the direct elastic scattering, where the incident neutron is deflected by the nuclear potential, but also neutron capture. In compound nucleus reaction, the incident neutron unites with the target nucleus, forming a relatively long-lived compound nucleus ($\gtrsim 10^{-17}$ seconds), whose excitation energy equals the sum of the kinetic energy and the binding energy of the captured neutron. The excitation energy of the compound nucleus can be given up with the emission of one or several γ rays (radiative capture or (n,γ) process), charged particles ((n,α), (n,p), (n,n p)) or two neutrons (n,2n). Moreover, if the neutron is emitted with energy smaller than the incident neutron energy, the residual nucleus remains in an excited state with subsequently decays by gamma ray emission (inelastic scattering). Finally, for heaviest nuclei also fission can occur. The compound nucleus formation is a resonance reaction, i.e., a compound nucleus can only be form if the sum of the binding energy and kinetic energy of the incident neutron corresponds to an excited state of the compound nucleus [20].

The main characteristic of a reaction is the cross section σ, which is a quantitative measure of the probability that an interaction occurs. Suppose that a beam of particles is incident on a target. If the interaction products are the scattered incident particles, then we are referring to elastic scattering. If the interaction products have a different identity from the incident particles, then we are referring to a reaction. The cross section is defined by [9]:

$$\sigma = \frac{N_r}{\Phi N_t} \tag{1.2}$$

where N_r is the number of interactions per time unit, Φ is the number of incident particles per area per time unit and N_t is the number of identical target nuclei within the beam. The cross section has the dimension of a surface area, as follows from the other quantities in Equation 1.2: $\Phi(\mathrm{cm}^{-2}\mathrm{s}^{-1})$, $N_t(\mathrm{cm}^{-3})$ and $N_r(\mathrm{cm}^{-3}\mathrm{s}^{-1})$. As a measure for cross sections is used the unit barn: 1 barn $= 10^{-28}$ m^2 $= 10^{-24}$ cm^2. In general, cross sections depend on the relative velocity of the target plus incident particle beam system, that is, $\sigma = \sigma(v)$ or $\sigma = \sigma(E)$.

The radiative capture process (n, γ) is important in the formation of heavy nuclei (s and r-processes discussed in Section 1.4.3). At energies where the cross section is not too small, capture cross sections can be studied in laboratory with different methods: the detection of the recoiling nucleus, the direct detection of the gamma rays and delayed decay measurements.

1.5.2 Stellar reaction rates

In stellar interiors, the plasma is considered to be in thermodynamic equilibrium. The probability for the occurrence of a nuclear reaction depends on the relative velocities between the interacting nuclei. Since the low density and high temperature of neutrons, the plasma can be considered an ideal gas, therefore, the velocities of nuclei can be described by a Maxwell–Boltzmann distribution. At thermodynamic equilibrium, if the velocity distributions of the interacting nuclei are separately described by Maxwell–Boltzmann distributions, then it follows that the relative velocities between the nuclei will also be Maxwellian [21]. Hence, particles are quickly thermalized and their velocities v_x follow a Maxwell–Boltzmann distribution, which only depends on the mass m_x of the particle and on temperature T. The probability to find a particle with a velocity between v_x and $v_x + dv_x$ can be written as:

$$\Phi(v_x)dv_x = 4\pi v_x^2 \left(\frac{m_x}{2\pi kT}\right)^{3/2} \cdot \exp\left(-\frac{m_x v_x^2}{2kT}\right) dv_x \tag{1.3}$$

where k is the Boltzmann constant.

The reaction rate (r_{XY}) is a reference parameter in nuclear astrophysics calculations and is defined as the number of reactions per cubic centimeter and per second for two reactant particles (X and Y). For a given number densities N_X and N_Y, assuming a reaction cross section $\sigma(v)$ and a relative velocity v between X and Y, the r_{XY} can be written as:

$$r_{XY} = N_X \cdot\ N_Y \cdot\ \sigma(v)\ \cdot v \tag{1.4}$$

Considering the velocity distribution, the previous equation becomes:

$$r_{XY} = N_X \cdot N_Y \cdot \langle v \cdot \sigma(v) \rangle \tag{1.5}$$

The reaction rate per particle pair $\langle \sigma v \rangle$ is an important quantity in stellar models and represents the averaged value of the cross section times the relative velocity. Employing the Equation 1.3, the $\langle \sigma v \rangle$ can be written as:

$$\langle \sigma v \rangle = \int_0^\infty \Phi(v)\sigma(v)v dv = 4\pi \left(\frac{\mu}{2\pi kT}\right)^{3/2} \int_0^\infty \sigma(v)v^3 \exp\left(-\frac{\mu v^2}{kT}\right) dv \tag{1.6}$$

where μ is the reduced mass, $\mu = m_x m_y/(m_x + m_y)$.

With $E = \mu v^2/2$ and $dE/dv = \mu v$, we may write the velocity distribution as an energy distribution:

$$\begin{aligned} \Phi(v)dv &= \Phi(E)dE = 4\pi \left(\frac{\mu}{2\pi kT}\right)^{3/2} \exp\left(-\frac{E}{kT}\right) \frac{2E}{\mu}\frac{dE}{\mu} \sqrt{\frac{\mu}{2E}} \\ &= \frac{2}{\sqrt{\pi}} \frac{1}{(kT)^{3/2}} \sqrt{E} \exp\left(-\frac{E}{kT}\right) dE \end{aligned} \tag{1.7}$$

For the reaction rate per particle pair (Equation 1.6), is obtained:

$$\begin{aligned}\langle\sigma v\rangle &= \int_0^\infty \Phi(v)\sigma(v)v dv = \int_0^\infty v\ \Phi(E)\sigma(E)dE \\ &= \left(\frac{8}{\pi\mu}\right)^{1/2}\left(\frac{1}{kT}\right)^{3/2}\int_0^\infty \sigma(E)\ E\ \exp\left(-\frac{E}{kT}\right)dE \end{aligned} \tag{1.8}$$

1.5.3 Maxwellian Averaged Cross Section

To calculate the reaction rate in the neutron capture processes it is common to work with the Maxwellian-Averaged Cross Section (MACS). The parameter is defined as the reaction rate scaled by the most probable velocity $v_T = \sqrt{2kT/\mu}$ of the Maxwell-Boltzmann distribution:

$$\text{MACS} = \langle\sigma\rangle = \frac{\langle\sigma v\rangle}{v_T} = \frac{2}{\sqrt{\pi}}\frac{1}{(kT)^2}\int_0^\infty \sigma(E)\ E\ \exp\left(-\frac{E}{kT}\right)\ dE \tag{1.9}$$

The current MACS values are collected in the Karlsruhe Astrophysical Database of Nucleosynthesis in Stars (KADoNiS) database [22], which contains the experimental data for 357 isotopes on the s-process path. KADoNiS database has been continuously updated to the present version v1.0. Charged particle reaction rates for the p-process have been also added.

Mainly for the s-process, the MACS is the only component employed to calculate the abundance of the elements. For a given temperature and neutron density, the MACS provides directly the reaction rate inside the stars and therefore, the abundances. The MACS can be calculated analytically at every stellar temperature using the cross section as a function of neutron energy or it can be measured directly, for example, with the activation method (described in the Section 2.1.2).

Current values of MACS between Fe and Pb for a characteristic thermal energy of kT = 30 keV is illustrated in Figure 1.6 [23]. For meaningful abundance predictions it is important to achieve a certain level of accuracy in the MACS data. In the past decade significant progress in experimental techniques has led to increasingly accurate data, evident from the fact that many of the data points in Figure 1.6 exhibit uncertainties smaller than the ±4% [23]. On average, cross sections should be available with an accuracy of 5% or better. For a number of key isotopes (like the 33 s-only nuclei) uncertainties as low as 1-2% are mandatory [24]. Nevertheless, additional, and more precisely measured cross sections are still needed. Figure 1.7 shows the respective uncertainties versus mass number for an energy, here, the accuracy criteria are met only in a minority of cases. Figure 1.7 refers to thermal energies of kT $= 25 - 30$ keV, characteristic for He burning temperatures, but it is

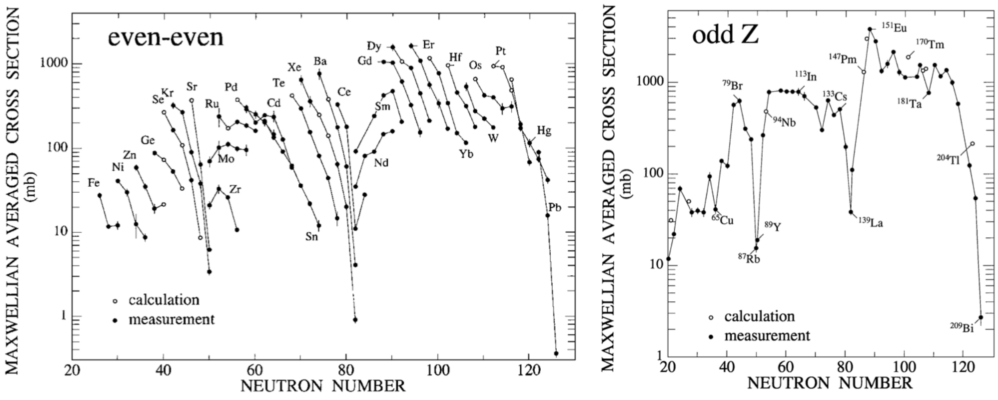

(a) (b)

Figure 1.6: The MACS along the s-process reaction path: a) even-even nuclei; b) odd Z nuclei [23].

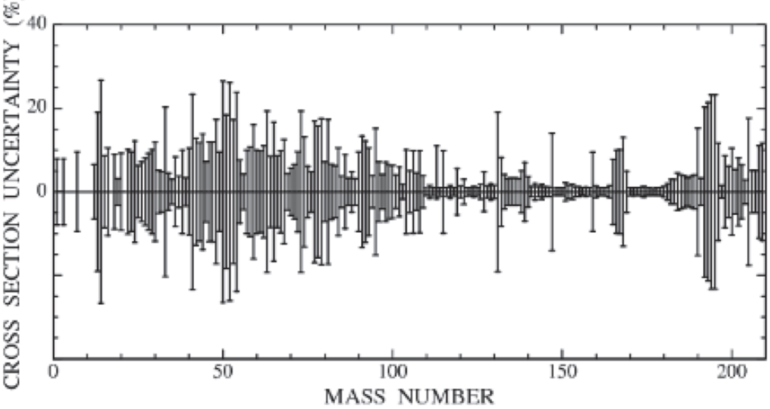

Figure 1.7: Presently uncertainties of MACS for kT = 25 keV (data from the KADoNiS compilation [25]).

generally worse for carbon shell burning in massive stars with kT = 90 keV [24].

1.6 Neutron sources

For cross section measurements, neutrons are produced using research reactors and accelerators. At present, there are still a group of special nuclear reactors that are used as neutron sources for training and research. In January 2021, there were in operation worldwide 222 reactors for training and research, according to the International Atomic Energy Agency (IAEA) [26] Research Reactor Database [27], and 15 of them for nuclear data measurements. An example of a reactor neutron source, still operational since 1971, employed in cross section measurements, is located at the Institut Laue-Langevin (ILL) [28], in France, but is going to close.

A map with the worldwide locations of the Accelerator-Based Neutron Sources (ABNS) is shown in Figure 1.8. A total of 146 ABNS are found worldwide in 32 countries. The ABNS are classified as: (1) Compact Accelerator-Driven Neutron Source (CANS), (2) Neutron Generator and (3) Spallation sources. The vast majority are Neutron Generators (86), followed by the CANS (49), while a few spallation neutron sources (11), are available. CANS loosely encompass low-energy proton-, deuteron-, and electron-accelerators, in linear or circular configurations, of moderate beam power (<30 kW) [29]. In Neutron Generators the neutron beams are produced by nuclear fusion. They use a compact linear accelerator to fuse together isotopes of hydrogen (deuterium (D) or tritium (T)). They are known as a D-D or D-T neutron generator with deuterium and tritium as target, respectively [30]. A spallation source is a high-flux neutron source in which protons that have been accelerated to high energies (greater than 0.5 GeV) hit a heavy metal target, causing the emission of neutron [31].

For high resolution cross section measurements, neutron time-of-flight (nTOF) facilities are the only practical possibility. Some examples of these ABNS facilities in Europe are: (1) the Geel Electron Linear Accelerator (GELINA) [33], at the Joint Research Centre (JRC), in Geel, Belgium; (2) the n_TOF (Neutron Time-of-Flight)

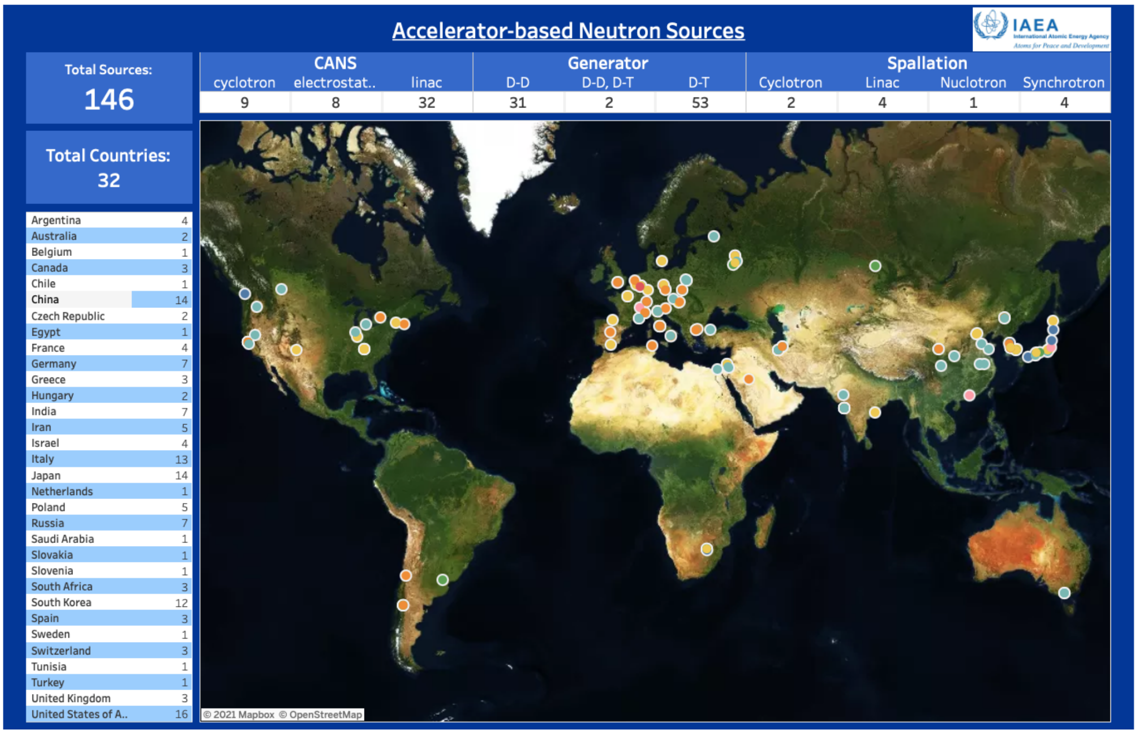

Accelerator-based Neutron Sources

Total Sources:
146

Total Countries:
32

CANS			Generator			Spallation			
cyclotron	electrostat..	linac	D-D	D-D, D-T	D-T	Cyclotron	Linac	Nuclotron	Synchrotron
9	8	32	31	2	53	2	4	1	4

Argentina	4
Australia	2
Belgium	1
Canada	3
Chile	1
China	14
Czech Republic	2
Egypt	1
France	4
Germany	7
Greece	3
Hungary	2
India	7
Iran	5
Israel	4
Italy	13
Japan	14
Netherlands	1
Poland	5
Russia	7
Saudi Arabia	1
Slovakia	1
Slovenia	1
South Africa	3
South Korea	12
Spain	3
Sweden	1
Switzerland	3
Tunisia	1
Turkey	1
United Kingdom	3
United States of A..	16

Figure 1.8: Map of accelerator-based neutron sources (ABNS) in the World [32].

facility [34] at the European Organization for Nuclear Research (CERN) [35] in Geneva, Switzerland; (3) HiSPAlis Neutron Source (HISPANos) facility [36] at the National Center of Accelerators (Centro Nacional de Aceleradores (CNA)) [37], a joint center of the University of Seville, in Seville, Spain and; (4) the nTOF line at the CN Van de Graaff accelerator, employed in this work, at the Legnaro National Laboratory of the Italian Institute of Nuclear Physics (LNL-INFN) [38], in Padua, Italy. The main characteristics of the Van de Graaff accelerator, employed in this work, are exposed in Section 4.1.

The main characteristics of the mentioned neutron generating facilities are following summarized. The GELINA facility was specially designed and built for high resolution cross section measurements. The facility has a linear electron accelerator, delivering a pulsed electron beam that impinges in a rotating mercury cooled uranium target. This source provides electrons in bunches of less than 2 ns (Full Width Half Maximum (FWHM)), and neutrons in the energy range of thermal up to 20 MeV, and a repetition rate up to 800 Hz. An array of flight paths up to 400 m long are possible (experimental locations at distances of 10, 30, 50, 60, 100, 200, 300 and 400 m), on which as many as 10 experiments can be carried out simultaneously [33]. The average neutron production rate delivered is 3.4×10^{13} neutrons/second.

The n_TOF facility at CERN entered in operation in 2001, with the aim to perform a consistent set of high accuracy cross sections measurements, extending over eight orders of magnitude in the neutron energy. This facility uses the spallation process of 20 GeV/c protons on an extended lead target and the remarkable beam density of the CERN Proton Synchrotron (PS). This PS accelerator can generate high intensities up to 7×10^{12} protons per pulse, high enough to produce 2×10^{15} neutrons per pulse, with 6 ns root mean square (RMS) width. The pulses have a repetition time that varied from 2.4 s to 16.7 s. The neutrons energies cover a range from a few MeV to 1 GeV [39]. At present, the n_TOF facility has two experimental areas. The first one, named EAR1, is located at 185 m from the target, in the horizontal direction. The large flight path makes possible to achieve a high energy resolution. The second experimental hall is named EAR2, was built in 2014 and is located in a vertical line at 20 m from the target. This area has the advantaged of higher neutron flux, by a factor of about 25, when compared with EAR1, since is located closer to the target [40]. Different detection systems have been developed by the n_TOF Collaboration for measurements of capture, neutron-induced fission, and inelastic reactions. From 2019 to 2021, the accelerators at CERN were shut down for upgrades and maintenance of the components in the accelerator complex. During this period, a new target installation in the n_TOF facility was incorporated.

The HISPANos facility is the first ABNS installed in Spain. It is located at the 3 MV tandem accelerator at the National Center of Accelerators (CNA), in Seville. The facility accelerates protons or deuterons beams up to 6 MeV of energy and current of 10 μA. Thermal, epithermal and fast neutrons can be produced by different reactions: (1) ^{7}Li(p,n)^{7}Be with thin and thick lithium targets, (2) D(d,n)^{3}He with thin deuterium targets and,(3) ^{9}Be(d,n)^{10}B with a thick beryllium targets. An upgrade of this accelerator was performed to obtain pulsed ion beams for time-of-flight measurement. The pulsing system installed allows to have proton and deuteron pulsed beams with less than 2 ns width, and variable repetition rate among 62.5 and 2000 kHz [41, 42].

Chapter 2

Maxwell-Boltzmann like neutron spectrum production

2.1 Stellar cross section measurement

Neutron cross sections measurements for nuclear astrophysics studies are determined by two complementary experimental methods: (1) time-of-flight (TOF) technique and (2) the activation method. The production of a neutron beam is require in both cases [19]. In this chapter, both methods will be briefly discussed.

2.1.1 Neutron time-of-flight experiments

Neutron time-of-flight (nTOF) technique enables cross section measurements as a function of neutron energy. With the knowledge of the neutron flight path and the flight time between the neutron production target and the capture sample, the neutron energy is determined [43].

A schematic representation of how this technique works is shown in Figure 2.1. After a pulse beam strikes a neutron producing target, neutrons with a broad energy distribution are quasi-simultaneously produced. Then, the emitted neutrons travel to the irradiation sample, located at a distance L (flight path) from the neutron producing target. In the sample to be measured, neutron induced (n,γ) reactions take place, where the γ rays (prompt radiation) produced in the interaction are detected. Knowing the neutron flight time (t), from the production target to the sample where the reaction takes place, the neutron energy can be determined as:

$$E_n = m_n c^2(\gamma - 1) \tag{2.1}$$

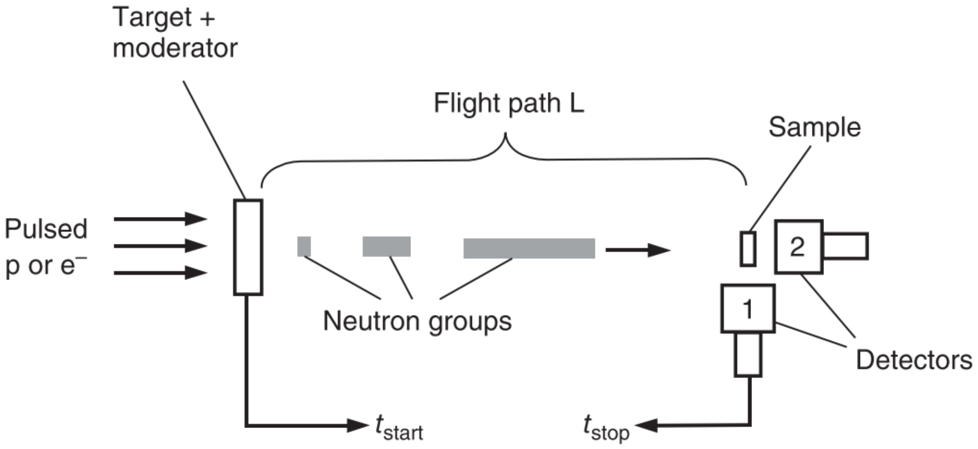

Figure 2.1: Schematic representation of the neutron time-of-flight (nTOF) technique for cross section measurements [9].

where $\gamma = (\sqrt{1 - v_n^2/c^2})^{-1} = (\sqrt{1 - (L/t)^2/c^2})^{-1}$, m_n is the neutron mass and c the speed of light. The neutron travelling times are calculated as the difference between the detection time (t_{stop}) and the time when they were generated in the target (t_{start}), $t = t_{stop} - t_{start}$. The relativistic correction γ can usually be neglected in the neutron energy range of interest in nucleosynthesis studies since introduces an error $< 0.2\%$ at $E_n = 1$ MeV. Then, the Equation 2.1 is reduced to:

$$E_n = \frac{1}{2} m_n v_n^2 = \frac{1}{2} m_n \left(\frac{L}{t}\right)^2 \tag{2.2}$$

With an adequate neutron flight path and beam time resolution, the TOF spectrum measured at a certain distance from the target is sketched in Figure 2.2. The TOF method requires that the neutrons are produced at well-defined times. The essential features in Figure 2.2 are the peak at $t = L/c$ (so called γ flash), due to prompt photons produced by the impact of an incident particle on the target, followed by a broad distribution when the neutrons reach the detector [19]. The discrimination between the γ flash peak and the neutrons depends on which value of flight path is selected and the beam time resolution.

Neutron time-of-flight facilities are mainly characterized by two features, the energy resolution ΔE_n and the flux. The uncertainties in the neutron flight time (t) determination and in the flight path (L) determine the neutron energy resolution:

$$\frac{\Delta E_n}{E_n} = 2\sqrt{\frac{\Delta t^2}{t^2} + \frac{\Delta L^2}{L^2}} \tag{2.3}$$

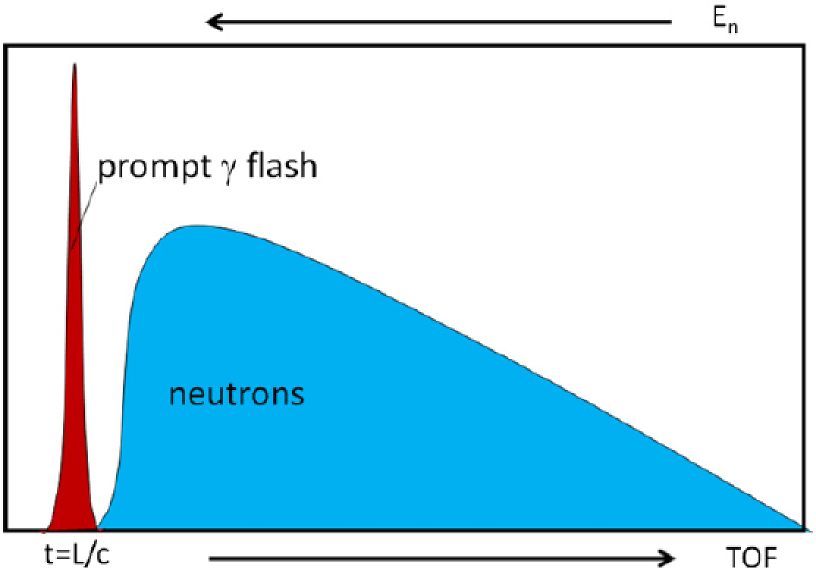

Figure 2.2: Schematic representation of the time-of-flight spectrum [19].

The uncertainty in the flight path (ΔL) is influenced by the finite sizes of the detector and the neutron producing target. The uncertainty in the time-of-flight (Δt) is influenced by the pulse rise time of the detector, and by the time width of a proton bunch. While the TOF uncertainty (Δt) influences the energy resolution of high-energy neutrons, the uncertainty in the flight path (ΔL) influences the energy resolution of low-energy neutrons. From the Equation 2.3, the energy resolution can be improved by increasing L, but only at the expense of the neutron flux, which scales with $1/L^2$. Therefore, the ideal combination of energy resolution and neutron flux is always an appropriate compromise.

In TOF capture reaction measurements, via the detection of the prompt γ ray cascade emitted in the decay of the compound nucleus, neutron capture cross sections are determined. Current TOF measurements of (n,γ) cross sections are based on two types of detectors: (1) total energy detection systems or total absorption calorimeters, (2) hydrogen-free liquid scintillators in combination with the pulse-height weighting function (PHWF). In total absorption calorimeters, the full energy sum of the γ ray cascade emitted in the decay of the compound nucleus are detected, which corresponds essentially to the neutron separation energy of the captured neutron. The most direct way to unambiguously identify (n,γ) reactions and to determine capture cross sections with good accuracy, are 4π detector arrays with an efficiency close to 100%. The main problem in using this type of detectors arises from their response to neutrons scattered in the sample. Hydrogen-free liquid scintillators in combination with the pulse-height weighting function (PHWF) solved the problem of neutron sensitivity. As an example, detectors based on deuterated benzene (C_6D_6), has been designed to minimize backgrounds due to scattered neutrons. Although the efficiency of C6D6 detectors is only about 20%, they are clearly of advantage in studies of resonance-dominated cross sections with very small capture-to-scattering ratios [24].

The TOF measurements are characterized by a low neutron flux, since it is compulsory to have a pulsed beam and since the sample is located at a certain flight path (which reduces the solid angle). Such thing limits the number of capture cross sections that can be measured. Furthermore, since the low flux, the measurements are performed with high mass samples. By the contrary, TOF measurements are essential for obtaining energy-differential neutron capture cross sections over a sufficiently large energy range. In this way, the MACS values can be calculated from these data for any stellar temperature (kT) of interest.

2.1.2 Activation technique

There are instances where reactions like $X(\mathrm{n},\gamma)Y$ will produce a radioactive nucleus Y. In this case, instead of detecting the prompt radiation like in the TOF method, it could be measured the residual radioactivity after the irradiation of the target or sample, and measuring then the experimental cross section. This technique is referred as the activation method. The experimental cross section is calculated as:

$$\sigma_{exp} = \frac{\varepsilon}{N_X}\frac{N_Y}{\Phi_n} \tag{2.4}$$

where N_Y is the number of radioactive nuclei (deduced from the measured radioactivity), Φ_n is the neutron flux received by the sample, N_X is the surface density (atoms/cm^2) and ε is the efficiency of the detector.

The schematic time evolution of the number of radioactive nuclei N_Y in the sample is shown in Figure 2.3. The irradiation of the target starts at $t = 0$ and stops at $t_0 = 6\ t_{1/2}$, where the number of radioactive nuclei $N_Y(t)$ is close to the saturation value. After some waiting period between t_0 and t_1, the activity is measured between t_1 and t_2, when $N_Y(t)$ decays exponentially. Taking into account the number of counts registered in the detector, the gamma intensity and the detector efficiency, it is possible to calculate the number of produced radioactive nuclei.

The activation method presents certain advantages respect to the TOF technique. Respect to the TOF technique, very accurate measurements can be obtained with the activation method. Counting the number of radioactive nuclei N_Y via the activity measurement, the information of astrophysical interest is directly provided (very

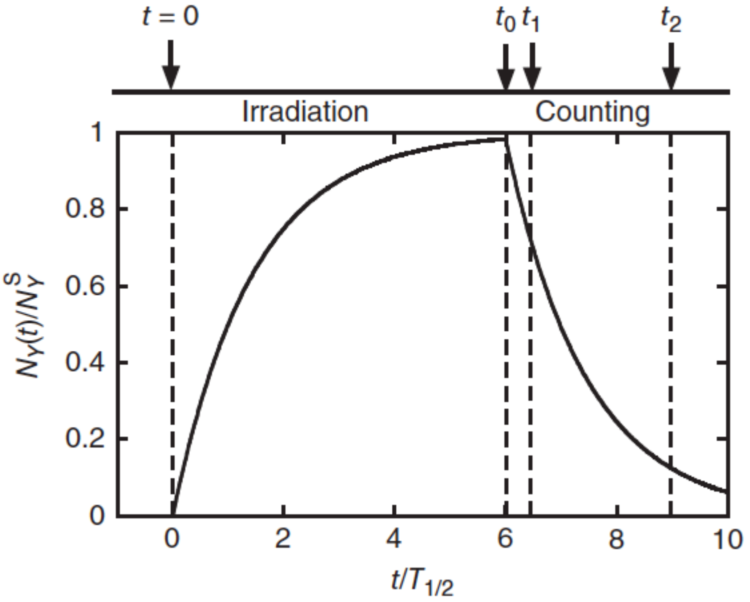

Figure 2.3: Evolution of the number of radioactive nuclei N_Y versus time (in units of the half-life, $t_{1/2}$)[9].

accurate measurements). For the activity determination a high purity germanium (HPGe) spectrometry is mostly used. One of the advantages of this method is that sometimes it is even possible to determine cross sections for several different reactions (with different samples) in a single measurement. Since no pulsed beam is needed, very high neutron flux is reached allowing to measure very low mass samples. Besides, this method allows to measure very low cross sections with high mass samples. One disadvantage of the activation method is that it is just suitable for radioactive reaction products with half-lives between a certain range (not years, not seconds). Since it is an integral cross section measurement, from a single activation measurement the MACS for a single stellar temperature (kT) is determined.

2.2 Activation with quasi-stellar neutron spectra

To obtain the Maxwell Averaged Cross Section (MACS) from an activation measurement, the neutron spectrum should correspond to the thermal spectrum in the stars . In 1988, Ratynski and Käppeler [44] published the MACS measurement with the activation method for the ^{197}Au(n,γ) reaction at kT= 25 keV, producing a quasi-stellar neutron spectrum via the ^{7}Li(p,n)^{7}Be reaction. The experimental setup employed in this experiment for the neutron spectrum determination is shown in Figure 2.4.

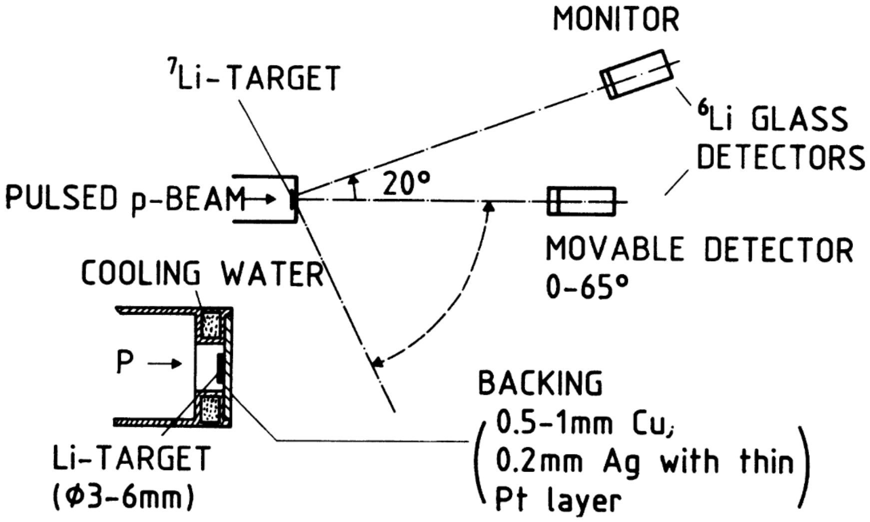

Figure 2.4: Experimental setup for neutron spectrum determination in the Ratynski and Käppeler experiment [44].

The neutron field was produced using a proton beam energy of $E_p = 1912$ keV (just 30 keV above the reaction threshold). With this proton energy, neutrons are emitted into a forward cone of 120 degrees opening angle. Lithium metallic targets and 1 mm copper backing were employed. The thickness of the lithium targets was calculated to slow down the proton beam below the reaction threshold (1880.6 keV) before being stopped in the target backing. Two lithium glass detectors were used. One detector was placed at 70 cm from the lithium target and was used as a stationary monitor to normalize the spectra obtained at various angles with the other detector. A second detector was moved around to measure the angle-dependent neutron spectra with the time-of-flight (TOF) technique. A proton pulsed beam with a repetition rate of 1 MHz and a pulse width of 1 ns was used to produce the neutrons through the ^{7}Li(p,n)^{7}Be reaction. Two flight paths (51.5 cm and 27.8 cm) were used to measure the neutron spectrum in an energy range from 1 keV to 120 keV. The TOF spectra were measured in steps of 5° form 0° to 65°. The angle-integrated neutron spectrum obtained in the work of Ratynski and Käppeler [44] is shown in Figure 2.5. The maximum neutron energy is 106 keV (limited by the kinematics). The results obtained at the short flight path (open squares) are also shown in the figure. The least squares fit to a Maxwellian distribution is represented with a solid line. There is a quite agreement with the experimental spectrum, specially for the lowest neutron energies. Around the peak there is a displacement in energy and in the tail of the spectrum the discrepancies are notable.

In the last years, some experimental works have reproduced the work of Ratynski

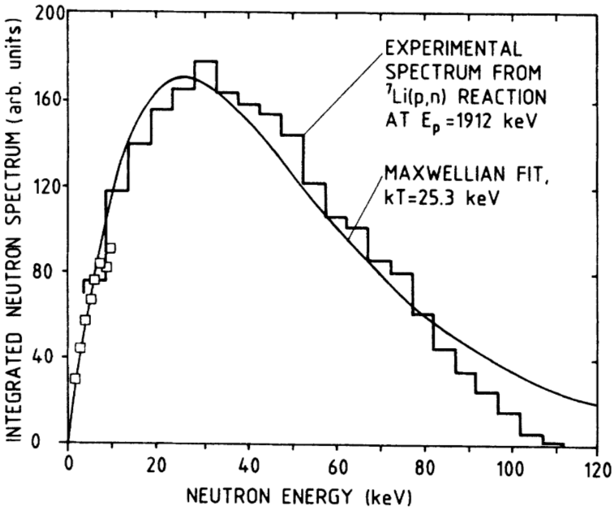

Figure 2.5: Neutron spectrum after integration over all angles, for proton energies E_p=1912 keV, in the Ratynski and Käppeler experiment [44].

and Käppeler. The consistent results obtained by Ratynski and Käppeler [44], Lederer *et al.* [45], Feinberg *et al.* [46] and Macías *et al.* [47] have shown the robustness of the method. These experiments used the TOF technique for the neutron spectrum determination.

2.3 Maxwell-Boltzmann spectrum production

In the previous section, the experimental neutron energy spectrum obtained in the work of Ratynski and Käppeler [44] was shown. The integral neutron energy spectrum from the mentioned work and the ideal Maxwell-Boltzmann neutron npectrum (MBNS) for a thermal temperature (kT) of 25.3 keV is shown in Figure 2.5. According to the authors, with protons energies of 1912 keV from the ^{7}Li(p,n)^{7}Be reaction, a good approximation to a MBNS with 25 keV of kT can be obtained. However, there is a difference in shape between the experimental neutron spectrum obtained in the Ratynski and Käppeler work and the ideal stellar spectrum. An obvious difference between these spectra can be seen in the higher energy region of the spectrum. The Maxwell-Boltzmann spectrum has a tail that theoretically extends to infinity. In that work, the obtained experimental neutron spectrum, with proton energies of 1912 keV, has an energy cutoff around 110 keV. As a consequence of these difference between the experimental neutron spectrum and the ideal one, a correction needs to be included to obtain an effective stellar cross section (MACS) from experimental measurements, when the sample is irradiated with this field. The value of said correction and, even more, its uncertainty are very difficult to determine. Hence, the importance of having a Maxwellian-like spectrum when measuring the MACS.

A possible solution or improvement to reduce these discrepancies in the neutron energy spectrum was published by Mastinu *et al.* [48], in 2009. In this article a method to obtain a MBNS at kT = 30 keV was proposed. The authors of this work proposed to modify or shape the neutron energy spectrum by shaping the projectile energy distribution in accelerator-based neutron sources (ABNS). This is done by means of a foil, placed before the neutron producing target, intercepting the projectile beam.

When a foil of some material intercepts a monochromatic beam of charged particles, the outgoing beam energy is not any more monochromatic. After the beam particles passed the foil the result is the production of a Gaussian-like energy distribution. The mean energy value and the width of the Gaussian distribution are controlled by the thickness and the material of the foil. In case the projectiles were protons coming from the ^{7}Li(p,n)^{7}Be reaction, the method is based on the idea that if the proton beam distribution is more wide, with protons that cover higher energies, the production of neutrons with higher energies will be obtained. In this way, the tail in the experimental neutron spectrum will be extended to higher energies without losing the similarity with a MBNS. A schematic representation of how this method works is shown in Figure 2.6. A monochromatic proton beam, with an energy spread of the order of 0.1% or lower, is passed throughout the proton energy shaper (properly constructed), producing a Gaussian-like proton distribution. The shaped beam impinges on a thick metallic Li target producing a neutron field that will follow a Maxwell-Boltzmann distribution. By choosing different materials, different thickness, or combinations of both of them, different thermal temperatures (kT) can be obtained.

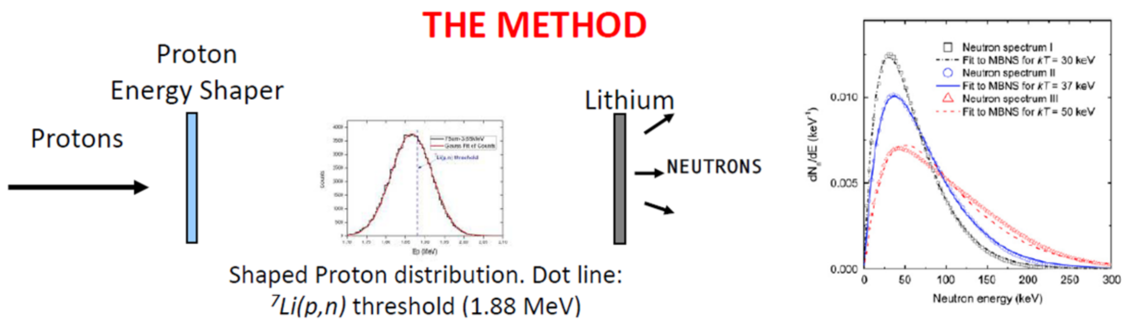

Figure 2.6: Method to produce a Maxwell-Boltzmann neutron spectrum (MBNS), proposed by Mastinu *et al.* [48].

Most neutron cross section measurements are carried out relative to the neutron cross section standards. The MACS of ^{197}Au(n,γ) at kT of 30keV is employed as a reference in cross section measurements, even though ^{197}Au is not a standard yet, in the stellar neutron energy range. The value of MACS= 582 ± 9 mb was referred in 1988 by Ratynski and Käppeler [44], in an accurate activation measurement. In more recent measurements, at n_TOF [34] and GELINA [33] facilities, discrepancies from this value of about 5% have been found. In 2011, at the n_TOF facility at CERN, measurements of the ^{197}Au(n,γ) reaction cross section employing the neutron time-of-flight (nTOF) technique were performed, and a value of MACS= 611 ± 22 mb was reported [49]. A similar value, 613 ± 9 mb, was found at GELINA facility, in 2014 [50]. A new recommended reference value of cross section at 30 keV kT of 611 ± 6 mb is referred in the KADoNiS data base version 1.0 [51]. The new standard value was derived between kT of 5-50 keV by the weighted average of the n_TOF and GELINA measurement. The new reference value reported in KADoNiS database has been indirectly supported by the Spectrum Averaged Cross Section (SACS) measurements reported by Martín-Hernández [13].

In the present work, the same method was employed to produce a MBNS with a thermal temperature of 30 keV. A study of the foil (or proton energy shaper) and its thickness was performed to ensure this condition. In the next sections, the obtained results will be presented.

2.4 ^{7}Li(p,n)^{7}Be reaction

The ^{7}Li(p,n)^{7}Be reaction has been widely used in accelerator-based neutron sources (ABNS) because of the high neutron yield. This reaction has been also widely studied in terms of cross section, neutrons energy and angle distributions and total neutron yield, as a function of target thickness and the proton energy [45].

The ^{7}Be, product of this reaction, has a half-life of 53.22 days. This unstable isotope decays by electron capture either directly to the ground state of ^{7}Li (89.5%) or via the 477.6 keV gamma rays of the de-excitation ^{7}Li (10.5%). The ^{7}Be decay level scheme is shown in Figure 2.7. Besides the gamma rays coming from the excited state of the^{7}Li, there are also the 478 keV gamma rays coming from proton inelastic scattering interaction with the target.

A completed description of the kinematics and yields of the ^{7}Li(p,n)^{7}Be reaction is required in order to choose the correct proton energy for obtaining a Maxwell-Boltzmann neutron spectrum (MBNS). These topics will be treated in the following subsections.

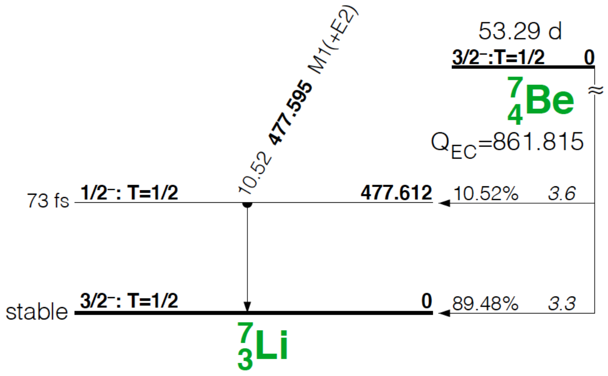

Figure 2.7: ^{7}Be decay level scheme [52].

2.4.1 Cross section

The ^{7}Li(p,n)^{7}Be cross section data, up to 3 MeV, available in Experimental Nuclear Reaction Data (EXFOR) [53] is shown in Figure 2.8. This reaction has a threshold at 1.880 MeV of proton energies. Near threshold, the cross section has a rapid rise producing large quantities of neutrons with energy ranging from a few up to hundreds keV. The cross section reaches a plateau of around 270 mb in the proton energy region from 1.92 to 2.05 MeV. A broad resonance centered at 2.25 MeV takes the cross-section up to 580 mb. For proton energies higher than 1.912 MeV, the neutrons are monoenergetic and the reaction cross section is quite large. In this energy region the ^{7}Li(p,n)^{7}Be reaction has long been used as a source of monoenergetic neutrons. Above 2.373 MeV the first excited state of ^{7}Be at 0.43 MeV may be excited, producing a second group of neutrons. For even higher proton energies, other reaction channels are open, like the three-body breakup reaction ^{7}Li(p,n^{3}He)^{4}He, or the second excited state of ^{7}Be, producing a third group of neutrons [54].

2.4.2 Kinematics

The kinematic of this reaction is very clearly described in the work of Lee and Zhou [55], in 1999. In that work, the authors developed a method for computing angular distributions, energy spectra, and total yields of this reaction for energies near the reaction threshold, using a compilation of data collected by Liskien and Paulsen [56]. A resume of the employed equations and the obtained results are followed shown in this section.

The Q value of the reaction, the energy threshold (E_{th}) and the neutron energy

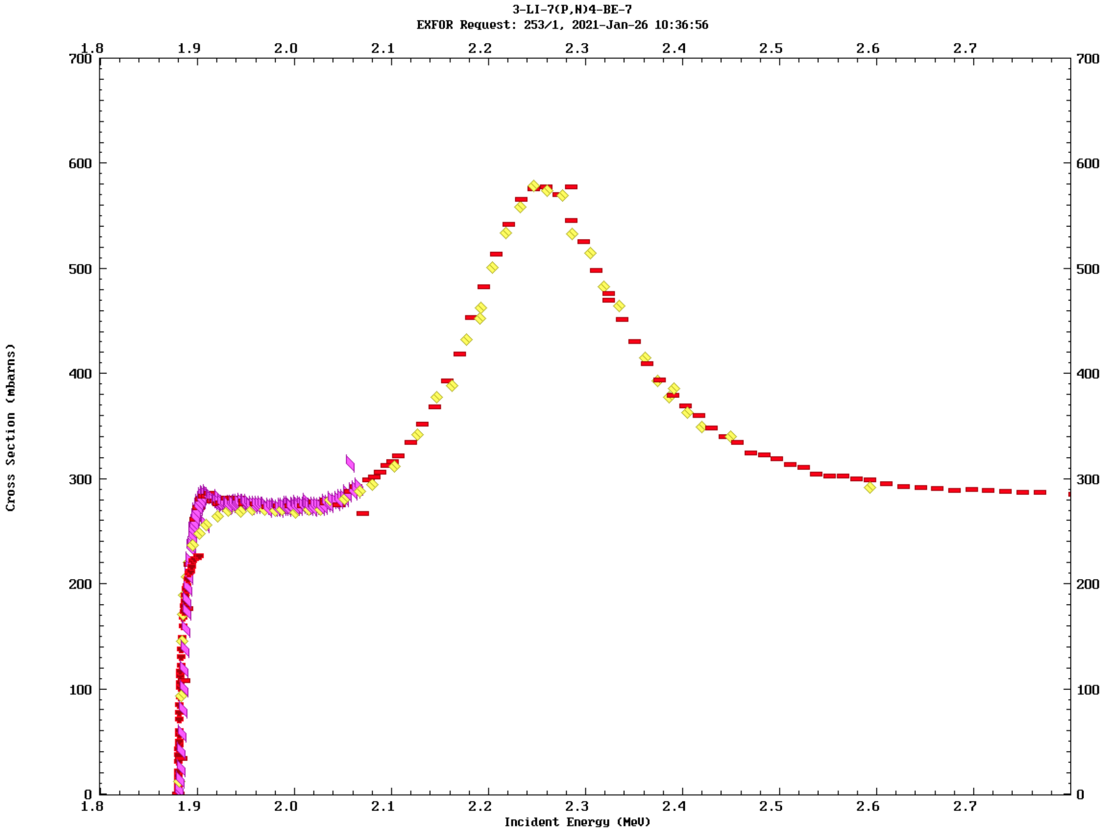

Figure 2.8: ^{7}Li(p,n)^{7}Be cross section data available in Experimental Nuclear Reaction Data (EXFOR) [53].

(E_n) at E_{th} were calculated as:

$$Q = M_p + M_{Li} - (M_n + M_{Be}) = -1644.28 \text{ keV} \tag{2.5}$$

$$E_{th} = -Q\,[1 + M_p/M_{Li} - Q/(2M_{Li})] = 1880.61 \text{ keV} \tag{2.6}$$

$$E_n(E_{th}) = M_p M_n E_{th}/(M_{Be} + M_n)^2 = 29.70 \text{ keV} \tag{2.7}$$

where M_p, M_n, and M_{Be} are the proton, neutron, and ^{7}Be nuclear masses, respectively.

The kinematic relations between E_n, the proton energy (E_p) and the neutrons emission polar angle (θ), in the laboratory system, were calculated with non-relativistic kinematics equations. The relation between these magnitudes is shown in Figure 2.9. Lines of constant values of E_p are plotted from an initial energy of 1.95 MeV to E_p equals to E_{th}. For proton energies below 1.92 MeV, neutrons are only produced in the forward direction ($\theta < 90°$). Moreover, for each angle of emission the neutron production is double-valued in the CM. But, any combination of θ and E_n gives only a value of E_p, and therefore, the differential neutron yield is a pointwise

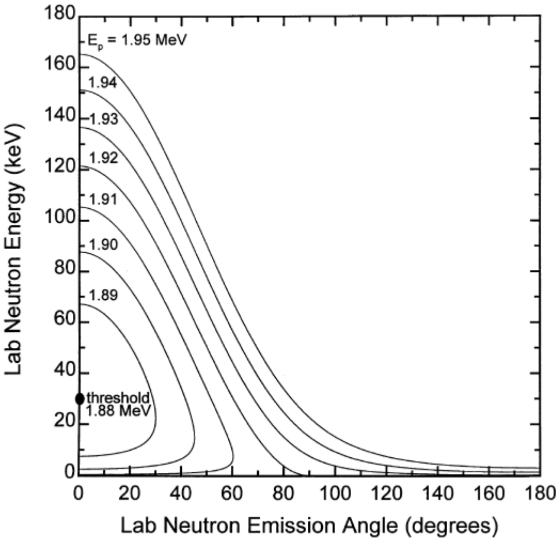

Figure 2.9: Proton energy contours for a thick lithium target [55].

function of these variables.

The differential neutron yield, in units of neutrons per keV per steradian per millicoulomb, at each proton energy is given by [55]:

$$\frac{\mathrm{d}^2Y}{\mathrm{d}\Omega\mathrm{d}E_n}(\theta,E_n)=N_{^7Li}\frac{(\mathrm{d}\sigma_{pn}/\mathrm{d}\Omega')(\mathrm{d}\Omega'/\mathrm{d}\Omega)(\mathrm{d}E_p/\mathrm{d}E_n)}{(-\mathrm{d}E_p/\mathrm{d}x)} \tag{2.8}$$

where $N_{^7Li}$ is the ^{7}Li atomic density, $\mathrm{d}\sigma_{pn}/\mathrm{d}\Omega'$ is differential (p,n) cross section in the center-of-mass system (CM), $\mathrm{d}\Omega$ and $\mathrm{d}\Omega'$ are the differential solid angles in the lab and CM system, respectively and; $-\mathrm{d}E_p/\mathrm{d}x$ is the proton stopping power in the target. With the knowledge of E_p and the introduction of the variables γ and ξ the multiplication of two of the terms in Equation 2.8 were calculated as:

$$\frac{\mathrm{d}\Omega'}{\mathrm{d}\Omega}\frac{\mathrm{d}E_p}{\mathrm{d}E_n}=\frac{\pm\left(M_{Be}+M_n\right)^2\left(\cos\theta\pm\xi\right)\gamma E_p}{M_pM_nE_p\xi\left(\cos\theta\pm\xi\right)\pm M_{Be}\left(M_{Be}+M_n-M_p\right)E_{th}} \tag{2.9}$$

$$\xi^2=1/\gamma^2-\sin^2\theta \tag{2.10}$$

$$\gamma=\sqrt{\frac{M_pM_n}{M_{Be}\left(M_{Be}+M_n-M_p\right)}\left(\frac{E_p}{E_p-E_{th}}\right)} \tag{2.11}$$

The stopping power term in Equation 2.8 from an analytic formulation to the experimental data fit was determined, using the work of Ziegler [57], but not considering the energy straggling. The last term to find in Equation 2.8, the CM differential (p,n) cross section, was determined depending on the value of E_p. For energies above 1.95 MeV cubic splines were fit through the data points given in the

Liskien and Pulsen's paper [56]. For energies between the threshold up to 1.925 MeV the cross section has the form of a board s-wave resonance, as pointed in the work of Gibbons and Macklin [58]. In this range the cross section was calculated as:

$$\frac{\mathrm{d}\sigma_{pn}}{\mathrm{d}\Omega'} = A\frac{C_0\sqrt{1 - E_{th}/E_p}}{E_p\left(1 + C_0\sqrt{1 - E_{th}/E_p}\right)^2} \tag{2.12}$$

where A and C_0 are constants. An interpolation of the obtained results with this equation in the energy range between 1.925 MeV and 1.95 MeV was performed, to find the values of cross section in this region.

By integrating the Equation 2.8 over solid angle and energy, respectively, the thick target neutron energy spectra and angular distributions, were calculated as:

$$\frac{\mathrm{d}Y}{\mathrm{d}E_\mathrm{n}}(E_\mathrm{n}) = 2\pi\int_0^{\theta_\mathrm{max}} \frac{\mathrm{d}^2Y}{\mathrm{d}\Omega\mathrm{d}E_\mathrm{n}}(\theta, E_\mathrm{n})\sin\theta\mathrm{d}\theta \tag{2.13}$$

$$\frac{\mathrm{d}Y}{\mathrm{d}\Omega}(\theta) = \int_{E_{n,min}}^{E_{n,max}} \frac{\mathrm{d}^2Y}{\mathrm{d}\Omega\mathrm{d}E_\mathrm{n}}(\theta, E_\mathrm{n})\,\mathrm{d}E_n \tag{2.14}$$

Figure 2.10a shows the solution for the thick target neutron energy spectra using the Equation 2.13. The figure shows the energy spectra for incident proton energies in steps of 10 keV between 1.89 MeV and 2.00 MeV. The angular distribution obtained using the Equation 2.14 is shown in Figure 2.10b. From this figure it is important to remark that the peak in the neutron emission spectrum is not in the forward direction. Also, there are no neutrons emitted in the 0° direction.

2.5 Study of proton energy shaper

An important constraint in the proton energy shaper determination was that no neutrons were produced by the employed materials. This condition ensures that only neutrons coming from the ^{7}Li(p,n)^{7}Be reaction were generated and detected in the measurement. A second condition was that the materials should produce the lowest possible amount of gamma rays after the proton beam passed the shaper. To this purpose, different materials and their isotopes were studied: carbon (C), aluminum (Al), titanium (Ti), copper (Cu) and lead (Pb). For the analysis, different aspects were taken in consideration: (1) the energy threshold for neutron production, (2) the value of the (p,n) cross section, (3) the neutron yield and, (4) the gamma yield. Some characteristic of the studied isotopes are presented in the Table 2.1. Proton induced thick target γ ray yields were reported in Savidou *et al.* [59].

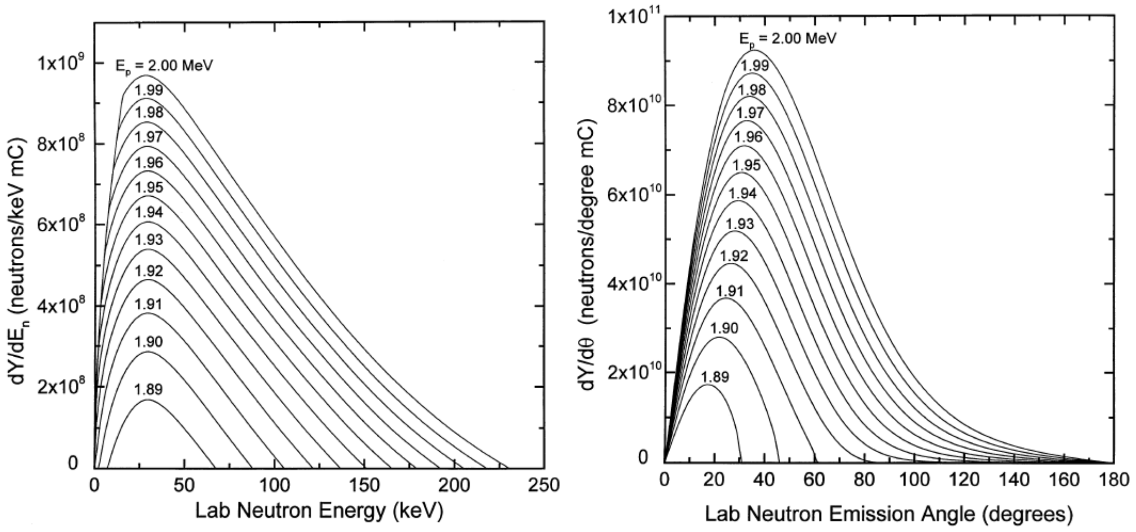

(a) (b)

Figure 2.10: For natural lithium metal target, near threshold thick target a) neutron energy spectra; b) neutron angular yields [55].

Lee and Zhou [55], in 1999, studied the kinematics and yield of the near threshold ^{7}Li(p,n)^{7}Be reaction. Following the same procedure employed by these authors and already explained in Section 2.4, a computer code was developed to solve the differential neutron yield. The double differential neutron yield is calculated with 1° and 1 keV intervals from 0° to 90 ° for θ, from 0 keV to 600 keV for E_n and from 1.88 MeV to 2.28 MeV for E_p. Considering the Gaussian-like proton distribution with a mean proton energy (E_m), the generated neutron spectrum was calculated as:

$$\frac{\mathrm{d}Y}{\mathrm{d}E_{\mathrm{n}}}\left(E_{\mathrm{n}}\right)=2\pi\frac{1}{\sigma\sqrt{2\pi}}\int_{\theta_{\min}}^{\theta_{\max}}\int_{0}^{\infty}e^{-\frac{(E_p-E_m)^2}{2\sigma^2}}\frac{\mathrm{d}^2Y}{\mathrm{d}\Omega\mathrm{d}E_{\mathrm{n}}}\left(\theta,E_{\mathrm{n}}\right)\ \sin\theta\ \mathrm{d}\theta\ \mathrm{d}E_p \qquad (2.15)$$

where θ_{min} and θ_{max} are the minimum and the maximum neutron angle for the integration, σ is the standard deviation of the Gaussian distribution, and FWHM the Full Width Half Maximum, (σ = FWHM/$(2\sqrt{2\ln 2})$). The E_m, FWHM, θ_{min} and θ_{max} were used as input parameters to compute this code. The theoretical neutron energy spectrum, calculated employing the Equation 2.15, is the outcome of this program.

A set of calculation were performed using the Stopping Power and Range of Ions in Matter (SRIM 2013) software [60], for various incident monochromatic proton energies impinging on different thicknesses of the studied materials. With a fitting

Table 2.1: Characteristics of the isotopes taken into consideration as energy shaper.

Isotope	Mass fraction	Threshold [MeV][a]	σ_1(p,n) [b][b]	Y_1 [n/μC][c]	σ_2(p,n) [b][d]	Y_2 [n/μC][e]	σ_3(p,n) [b][f]	Y_3 [n/μC][g]	σ_4(p,n) [b][h]	Y_4 [n/μC][i]
^{12}C	0.990	19.64	-	-	-	-	-	-	-	-
^{13}C	0.010	3.24	-	-	-	-	4.0×10^{-2}	1.24×10^{3}	5.0×10^{-2}	1.89×10^{3}
^{27}Al	1.000	5.80	-	-	-	-	-	-	-	-
^{46}Ti	0.083	8.01	-	-	-	-	-	-	-	-
^{47}Ti	0.074	3.79	-	-	-	-	-	-		
^{48}Ti	0.737	4.90	-	-	-	-	-	-	-	-
^{49}Ti	0.054	1.41	5.0×10^{-3}	1.85×10^{2}	4.0×10^{-2}	2.07×10^{3}	$1.0 \times 10^{-1}.0$	6.52×10^{3}	2.3×10^{-1}	1.79×10^{4}
^{50}Ti	0.052	3.05	-	-	-	-	1.0×10^{-1}	6.12×10^{3}	2.5×10^{-1}	1.83×10^{4}
^{63}Cu	0.692	4.22	-	-	-	-	-	-	-	-
^{65}Cu	0.308	2.17	-	-	5.0×10^{-4}	1.28×10^{2}	2.0×10^{-2}	6.36×10^{3}	9.0×10^{-2}	3.38×10^{4}
^{204}Pb	0.014	5.27	-	-	-	-	-	-	-	-
^{206}Pb	0.241	4.56	-	-	-	-	-	-	-	-
^{207}Pb	0.221	3.19	-	-	-	-	-	-		
^{208}Pb	0.524	3.68	-	-	-	-	-	-		

[a] Threshold energy for neutron production.
[b] Cross section (p,n) reaction between 1-2 MeV.
[c] Estimated neutron yield when protons go from 2 to 1 MeV.
[d] Cross section (p,n) reaction between 2-3 MeV.
[e] Estimated neutron yield when protons go from 3 to 2 MeV.
[f] Cross section (p,n) reaction between 3-4 MeV.
[g] Estimated neutron yield when protons go from 4 to 3 MeV.
[h] Cross section (p,n) reaction between 4-5 MeV.
[i] Estimated neutron yield when protons go from 5 to 4 MeV.

process to a Gaussian distribution, the mean proton energy (E_m) and the FWHM after the protons passed the material foil were determined, for each combination of thickness and initial proton energy. The relative errors on both parameters, obtained with the Gaussian fit, were always lower than 0.5%. The integral neutron spectra up to 90°, produced by protons with the Gaussian distributions, were calculated for every set of E_m and FWHM. Each integral neutron spectrum was then fitted with to a Maxwell-Boltzmann distribution, determining the thermal energy (kT) and the R-square coefficient of determination (R^2) for that fit. A second program was developed to find the neutron spectrum that fits best the Maxwell-Boltzmann distribution with 30 keV of kT, employing E_p and the FWHM as parameters. The R-square (R^2) coefficient of determination for each spectrum was calculated. The R^2 coefficient for a data set y_i with n values, means of $\bar{y} = 1/n \sum_i y_i$ and associated predicted value f_i, is defined as:

$$R^2 = 1 - \frac{\sum\limits_{i=1}^{n}(y_i - f_i)^2}{\sum\limits_{i=1}^{n}(y_i - \bar{y})^2} \tag{2.16}$$

A R^2 value closest 1 means a calculated neutron spectrum that fits better the Maxwellian distribution.

One of the isotopes of titanium has a low energy threshold value (1.41 MeV) for neutron production. Even if this isotope has an abundance of 5%, the Ti as shaper was discarded because of the presence of neutrons for lower proton energies. Carbon was a good candidate for the energy shaper since ^{12}C has 19 MeV as energy threshold for neutron production with an abundance in nature of 99%. To produce a MBNS with kT of 30 keV with a single carbon layer the proton energy needed is higher than the threshold for neutron production in ^{13}C. Besides, the proton energy found was near the working limits of the accelerator employed in the experiment (CN Van de Graaff accelerator at Legnaro National Laboratories of the Italian Institute of Nuclear Physics (LNL-INFN), Padua, Italy). Because of these reasons, carbon was also discarded. Different combinations of proton energies (E_p) and thickness for a foil of copper were also studied. It was not possible to find a combination of these parameters that generates a MBNS with kT of 30 keV, for proton energies lower than the threshold for neutron production (2.17 MeV for ^{65}Cu). A combination of layers from different materials was also taken into consideration. Even if a multiple layers may produce a better MBNS at 30 keV, a single layer material was chosen because it reduces the complications in the shaper construction. Lead and aluminum were a good choice, since both materials have a high energy threshold for neutron production. From the calculations performed with SRIM 2013 employing lead as material, it was found that a small variation in the foil thickness modifies drastically the produced neutron spectrum. Searching in the web, a possible tolerance (between 20-25%) in purchasable lead foil thickness was found. Taking into account the above considerations, aluminum was chosen as the material for the energy shaper.

After the SRIM 2013 and the best fit code calculations, an initial proton energy of 3.17 MeV and an aluminum foil of 50 μm thickness as proton shaper were found to be the best set of parameters. These values produced the best coefficient of determination R^2 between the generated neutron spectrum and the Maxwell-Boltzmann distribution with kT of 30 keV. Figure 2.11 shows the proton energy distribution after protons with an initial energy of 3.17 MeV have passed the aluminum foil with 50 μm thickness. This histogram was obtained with the SRIM 2013 software output. The Gaussian distribution fit is plotted with a black line, resulting in $E_m = 1.9094$ MeV and FWHM = 0.0937 MeV. In the figure, the energy threshold of the ^{7}Li(p,n)^{7}Be reaction (at 1.88 MeV) is also represented with a blue line. Protons with energies higher than this value will produce the neutrons.

The theoretical neutron spectrum for the E_m and FWHM obtained with the 50 μm Al foil and 3.17 MeV protons is shown in Figure 2.12. The fit with the Maxwell-Boltzmann distribution is also shown in the figure. A thermal temperature

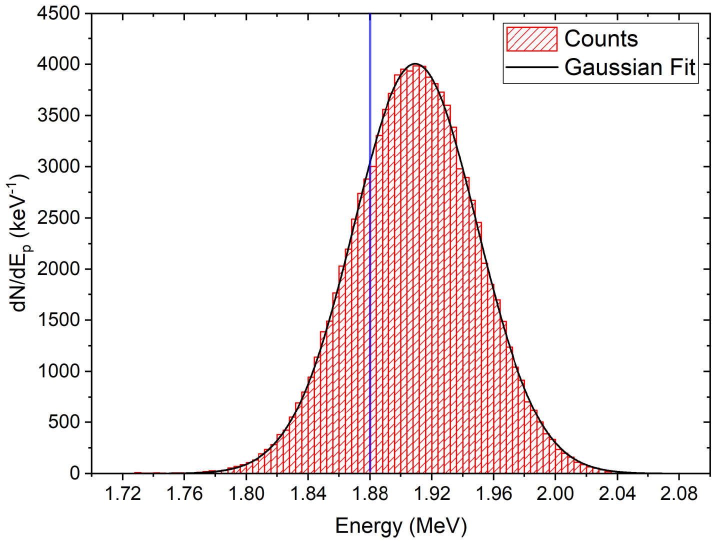

Figure 2.11: Proton energy spectrum after 3.17 MeV protons passed an aluminum foil of 50 μm thickness.

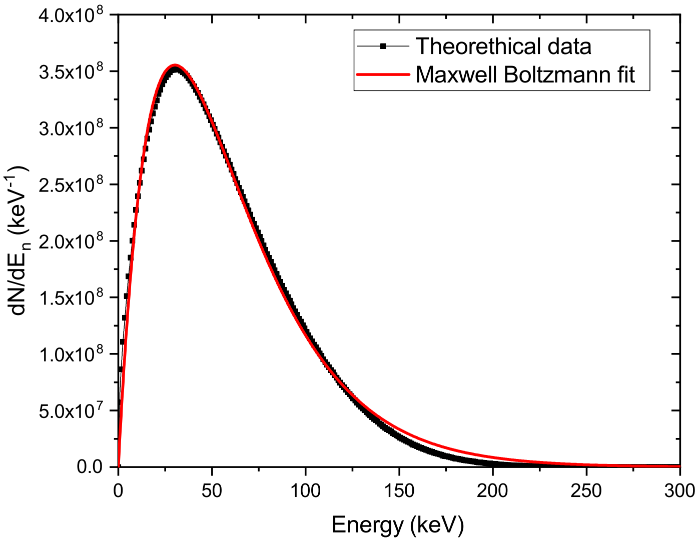

Figure 2.12: Theoretical neutron energy spectrum integrated up to 90°, for initial proton energies $E_p = 3.17$ MeV and an aluminum foil of 50 μm thickness.

of 30.18 ± 0.08 keV was obtained from this fit, with a R^2 value of 0.997.

With the determination of the involved parameters to produce a Maxwell-Boltzmann neutron spectrum (MBNS) with kT of 30 keV, the experiment was then performed. The experimental outline is shown in Figure 2.13. The experiment was carried out using the CN accelerator placed at Legnaro National Laboratories of the Italian Institute of Nuclear Physics (LNL-INFN), Padua, Italy. With an initial proton energy of 3.17 MeV and 50 μm Al foil thickness as shaper it was expected to produce a MBNS with a thermal temperature of 30 keV.

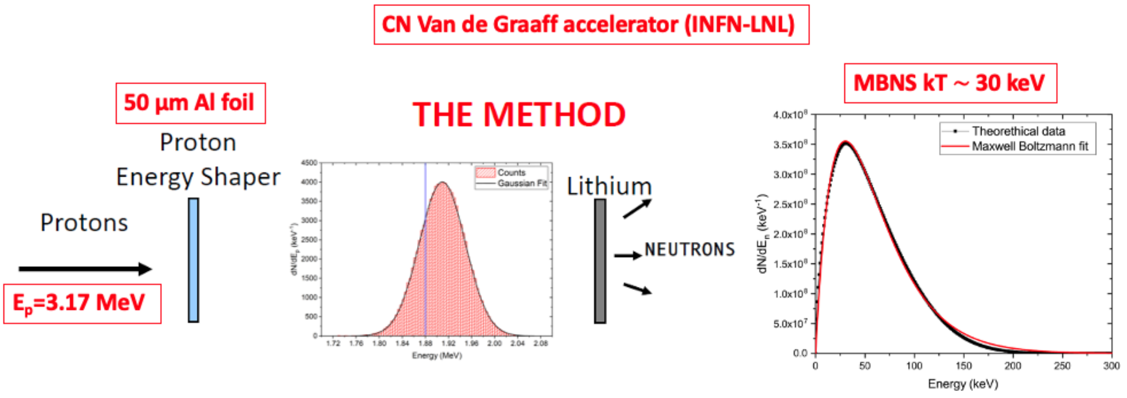

Figure 2.13: Outline of the experiment carried out to produce a Maxwell-Boltzmann neutron spectrum (MBNS) with kT of 30 keV.

Chapter 3

Neutron energy spectra conversion: from time-of-flight to energy

In this chapter, the problem of reconstructing the primary neutron spectrum from the measured one will be addressed. The method to analyze the time spectra obtained from the time-of-flight (TOF) measurement is presented.

3.1 Time-energy direct conversion and the energy resolution function

In neutron time-of-flight (nTOF) experiments, the neutron energy is determined from the time they spend traveling a specified distance (flight path). The precise knowledge of the neutron time and energy relation is essential when the nTOF technique is employed. This technique was described in the Chapter 2. In this case, the time-energy relation, for non relativistic neutrons, was determined by the Equation 2.2. A direct method to convert from TOF spectrum to an energy spectrum can be applied, using the neutron time-energy relation. Taking the values of 299.8 m/μs and 939.6 MeV/c^2 for the speed of light and the neutron mass, respectively, the Equation 2.2 is reduced to:

$$E_n \text{ [eV]} = \left(\frac{72.3 \times \text{L [m]}}{\text{TOF [}\mu\text{s]}} \right)^2 \tag{3.1}$$

where E_n is the neutron energy in electronvolts (eV), L is the flight path in meters (m), and the TOF is the neutrons time of flight in microseconds (μs).

When the time-energy relation (Equation 3.1) is employed as a direct conversion method, the number of neutrons in the TOF histogram within a time bin is directly associated to the energy bin, obtaining the detected energy spectrum. To obtain the neutron spectrum emitted by the source, the detected energy spectrum is divided by the detector efficiency.

Before being captured, neutrons travel from the production target to the detector at constant velocity. Inside the detector neutrons have interactions with all the materials in their path. Due to the detector size, neutrons are elastically or inelastically scattered before being captured. These facts increase the neutrons time of flight since there is a spread in the interaction position in the detector. Therefore, the "effective" flight path of neutrons can be defined as the sum of: (1) the geometrical length between the Li target and the detector outer face (fixed distance, L_0), (2) the moderation length inside the detector (variable distance) and, (3) the moderation in the target and backing. In this work, the thickness of the Li target plus copper backing was negligible compared to the geometrical flight path. However, the thickness of the Li glass detector (2.54 cm) was comparable to the geometrical flight path and was accounted in the effective flight path. Another factor that influences on the effective flight path is the time spread of the charged particles primary beam producing the neutron beam (the temporal distribution of the proton pulsed beam). Due to these reasons, when a single neutron energy is sampled the resulting TOF is not a single value but a distribution. Therefore, the direct conversion method is not accurate and should not be employed to convert from TOF to an energy spectrum.

With the aim of checking for discrepancies related to the direct conversion method, a random spectrum was compared with the one obtained when the direct method was applied to a TOF spectrum. As random spectrum, the theoretical neutron energy spectrum at zero degrees obtained with proton energies of 1912 keV was employed (see Figure 3.1a). For this purpose, a simulation of the neutron TOF spectrum obtained with the one inch Li glass detector was calculated using the Monte Carlo N Particle (MCNPX) [61] simulation code. In the simulation, to mimic the neutron source, placed at 72 cm from the detector outer face, the theoretical neutron energy spectrum was employed ($L = L_0 = 72$ cm). The structure and chemical composition of the Li detector was used in the simulation (see Figure 4.9 for more detail). The neutron scattering and capture cross sections are contained in the MCNPX libraries. In the detector, the neutron capture reaction (n,t) is produced and the tritium production is accounted. With the *Tally 4* and the cards *Time* and *FM*, it was possible to simulate the neutron travelling time between the neutron source and the tritium nucleus production point inside the detector crystal. As result, the neutron TOF was recorded as an histogram. The simulated TOF histogram is shown in Figure 3.1b. The detector efficiency (ratio between the number of detected

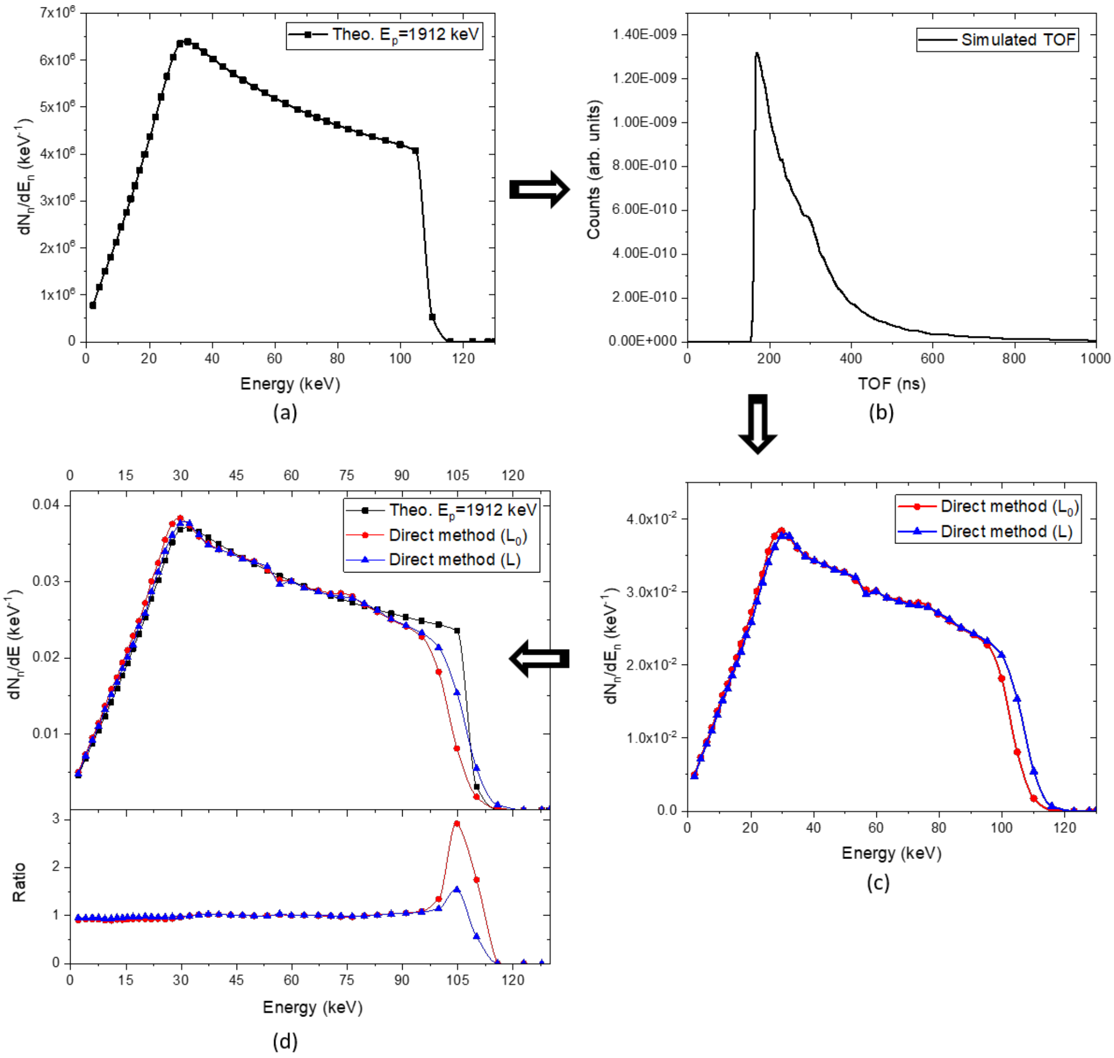

Figure 3.1: a) Neutron spectrum obtained from theoretical calculations with proton energies of 1912 keV, employed as neutron source in the MCNPX simulation. b) Simulated nTOF spectrum. c) Neutron spectrum obtained with the direct conversion of the simulated nTOF spectrum with L and L_0 as flight paths. d) Theoretical neutron spectrum compared with the neutron spectra obtained with the direct conversion method.

and incident particles) was also calculated by simulations using the MCNPX code. In the Section 4.4.1 it is explained how the detector efficiency was determined by the simulations. With the detected neutron spectrum (simulated) and the detector efficiency the emitted neutron spectrum was determined.

In Figure 3.1d it is plotted the neutron energy spectrum obtained with the direct conversion, using the energy-time relation (Equation 3.1) and the flight path L_0. The expected discrepancies between both spectra, especially in the high energy range of 80 to 120 keV, can be appreciated. A displacement of the maximum neutron energy can be observed since the moderation length was not taken into account. A first correction to the direct method can be applied by assuming the effective flight path as the distance (L_0) plus the half of the detector thickness ($\mathrm{L} = \mathrm{L}_0 + 2.54/2$). The obtained neutron spectrum is also shown in Figure 3.1, after the direct conversion method was applied with the flight path L. In this case, discrepancies between the expected values and the obtained ones are reduced, when compare to the results for L_0. In Figure 3.1d the ratio between the nominal values and the calculated ones for both spectra is shown. In this figure, the reduced discrepancies in the high energy part of the spectrum are observed. These two examples proved the fact that the direct conversion method, using the Equation 3.1, should not be employed, since the neutron moderation inside the detector is not properly accounted.

A different approach that can be found in the literature to convert from TOF spectrum to an energy spectrum, is the use of the energy resolution function. As already mentioned, due to the moderation process inside the detector, two neutrons with the same kinetic energy do not necessarily have the same measured TOF. This effect can be seen as a moderation time (t_{mod}) in the TOF or, as an effective moderation length (λ) calculated as the moderation time multiplied by the neutron velocity (v_E) when entering the detector:

$$\lambda = v_E \times t_{mod} = \sqrt{2E_n/m_n} \times t_{mod} \tag{3.2}$$

In this way a correction to the direct method is applied and the time-energy relation is then established by:

$$E_i = \left(\frac{72.3 \times (\mathrm{L}_0 + \lambda_i)}{\mathrm{TOF}_i}\right)^2 = \left(\frac{72.3 \times \mathrm{L}_0}{\mathrm{TOF}_i - (t_{mod})_i}\right)^2 \tag{3.3}$$

The distribution of the moderation length (λ) as a function of the neutron energy represents the resolution function. The resolution function is a probability density and can only be determined by an analytical approach of its components or, more commonly, by Monte Carlo simulations. The neutron production as well as the moderation process inside the detector are simulated and the neutron time distribution recorded. In the simulations, monoenergetic neutron sources with energies $E_i \pm \Delta E_i$ are sampled and, for each run, the moderation time inside the detector can be calculated from the neutron time distribution. The t_{mod} value for each energy is determined as the mean or most probable value of the simulated neutron time distribution. After the simulations, a simplification of the problem is possible if a parametrization of the resolution function (λ(E) or λ(TOF)) is found. In this case, the conversion of time to energy with Equation 3.1 is direct using the flight path as $\mathrm{L} = \mathrm{L}_0 + \lambda(E_n)$.

As reported by Colonna *et al.* [62] and Mingrone *et al.* [63], the resolution function is employed in the measurements of neutron-induced reaction cross sections at the n_TOF facility [34], at CERN, Geneva. Accurate measurements require very good knowledge of the neutron beam features in the experimental area. One of these features is its resolution function.

The method of using the resolution function corrects the direct method by adding to the analysis the effective flight path. Since only the mean value of the time distribution is taken into consideration as the moderation time and not the complete time distribution when this method is employed, a different approach was followed.

3.2 New approach with the detector response matrix

As discussed above, in the measurement of the incident neutron energy spectrum, the measured time-of-flight (TOF) spectrum in a given exposure time is in the form of an histogram, containing the detected number of particles per each temporal bin. To consider the contributions of the time distributions of different monoenergetic neutrons a numerical method was applied.

The neutron TOF spectrum is converted to an energy spectrum by convolution in form of a matrix as:

$$T_j = \sum_{i=1}^{n} N_i^{emitted} \times RM_{ij} \qquad j = 1...n, \tag{3.4}$$

or in vectors form:

$$\mathbf{T} = \mathbf{N_e} \times \mathbf{RM} \tag{3.5}$$

where **T** is the nTOF spectrum, **RM** is the convolution matrix (or detector response matrix), and $\mathbf{N_e}$ is the (yet unknown) neutron energy spectrum. In the nTOF spectrum, the scored T_j for the jth time bin is composed by tallying the components of the emitted energy spectrum $N_i^{emitted}$ times a factor equal to the contribution of the ith energy interval to the jth time bin. This factor is the corresponding element RM_{ij} of the detector response matrix **RM**. The emitted neutron spectrum is obtained with the solution of the system of n equations by multiplying the folded TOF spectrum by the inverse of the response matrix:

$$\mathbf{N_e} = \mathbf{T} \times \mathbf{RM}^{-1} \tag{3.6}$$

where $\mathbf{RM}^{-1}$ is the inverse of the **RM**. In the response matrix are included: (1) the detector efficiency and (2) the fact that the point where the neutron capture occurs (therefore, the moderation time) is known.

The response matrix is characteristic of each experimental setup, since depends on the geometry, the detectors, neutrons flight path, experimental area and properties of the neutron source. This means that the **RM** is always the same as long as none of the above parameters do not change. The **RM** is square and triangular. If only the most probable value of the TOF distribution is considered, the **RM** becomes diagonal, and the situation of Section 3.1 is verified. Each column of the matrix gives the probability that a neutron of energy $E_i \pm \Delta E_i$ undergoing an interaction into the detector will be measured as a count in the measured TOF spectrum. Thus, the response matrix contains the temporal information of the neutron travelling time and its capture inside the crystal. As is the case with the resolution function, the response matrix cannot be measured directly and, it is commonly evaluated by Monte Carlo simulations. The **RM** is formed by a set of subsequent response functions for different energies, defining the response function as the registered time distribution of a monochromatic neutron beam. The columns of the matrix denote the response functions corresponding to successive neutron energies.

In the present work, the **RM**, was determined using the Monte Carlo N Particle (MCNPX) [61] simulation code. As input in the MCNPX file a neutron source was placed at target position and the neutron time distributions in the detector were determined. The neutron source was placed at 72 cm from the outer face of the detector. For the determination of the response function, neutrons with energies $E_i \pm \Delta E_i$ were sorted in a circular surface source of 5 mm diameter. The time-energy relation (Equation 3.1) was employed with L as flight path. In the simulation, by adding a Gaussian time function into the source definition of the input MCNPX file, it is possible to take into account the beam time structure. To consider the neutron interactions with the detector materials, the one inch lithium glass detector with all its components was simulated (see Figure 4.9), accounting the detector efficiency.

Figure 3.2 shows a plot of some columns of **RM**, for the mentioned setup. In the figure, it is possible to appreciate the time spread for each neutron energy and the tail towards higher time bins due to multiple interaction events. Also notice that lower energies correspond to higher times.

In Figure 3.3 the uncertainties related to the time to energy conversion method using the calculated response matrix (some columns in Figure 3.2) are shown. The theoretical neutron spectrum for proton energies of 1912 keV (the same employed in the direct method conversion) and the neutron spectrum after this method was applied with the simulated TOF spectrum are shown in the figure. As can be observed, big fluctuations between positive and negative values are present, and more accentuated in the low energy part of the spectrum.

To solve these fluctuations, a new approach was developed always applying the deconvolution method to the TOF neutron spectrum and the response matrix. For monoenergetic neutron energies, the relation between the neutron energy and the most probable moderation time value is a continuum function. Due to the energy bins continuously variation, a continuity in the temporal bins is expected. With a new time-energy relation (most probable moderation time-energy), when the deconvolution method is applied no fluctuations should be present and the obtained spectrum should reproduce exactly the experimental one (the theoretical one in this example).

After the TOF bins where chosen, the response function for different neutron energies where analyzed. Nearly 5000 MCNPX files where analyzed, for monoenergetic neutron sources with 0.05% energy uncertainties ($E_n \pm 0.05\% E_n$). For these files, the response function of the detector with a time distribution determined from the TOF binnigs was calculated. For each file, the TOF for the most probable value of the time distribution was then associated to the correspondent neutron energy of the file. Therefore, the moderation time of neutrons inside the detector was taken into account in the time-energy association, like in the resolution function method. Figure 3.4 shows a comparison of the time-energy relationship determined with this novel approach and with the direct method employing the flight path L. The main differences are for low TOF values which correspond with higher neutron energies.

Then, with the new time-energy relation and following the same procedure as previously described, the new response matrix of the setup was calculated. Once the **RM** was obtained, the inverted matrix is calculated. As before, employing the same simulated neutron TOF spectrum, the deconvolution method was applied and the neutron energy spectrum was determined. Figure 3.5 shows the neutron spectrum from the theoretical calculations for proton energies with 1912 keV compared to the

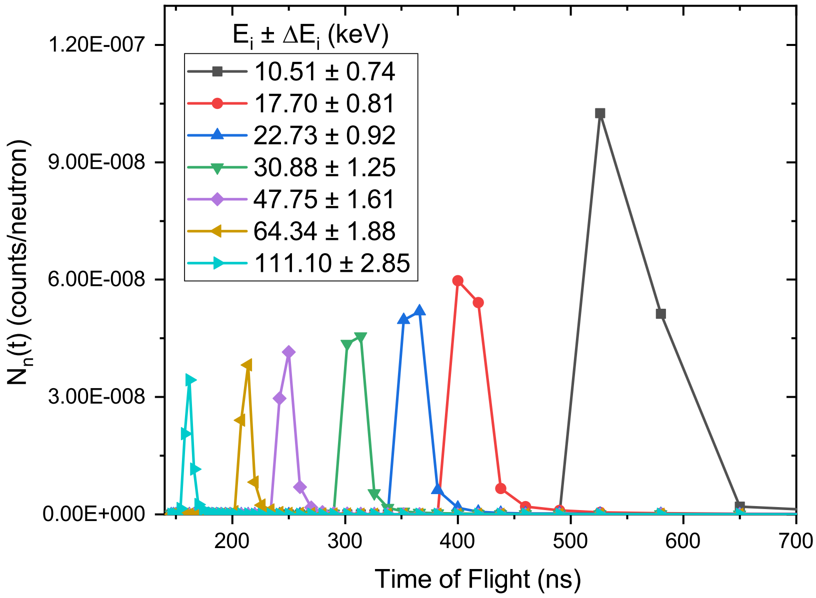

Figure 3.2: Calculated time distribution for different neutron energies, with $E_i \pm \Delta E_i$ energy widths.

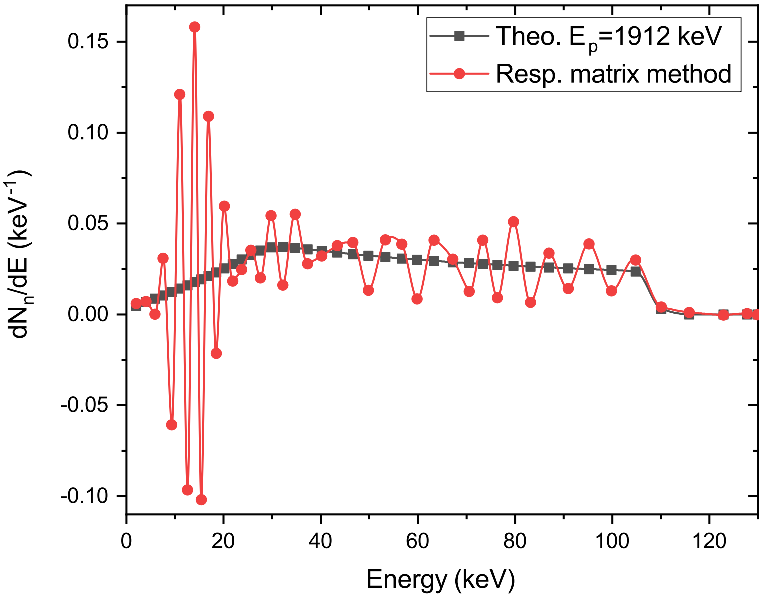

Figure 3.3: Neutron spectrum from theoretical calculations for proton energies with 1912 keV and the one obtained with the deconvolution method of the simulated nTOF spectrum (time-energy relation with Equation 3.1).

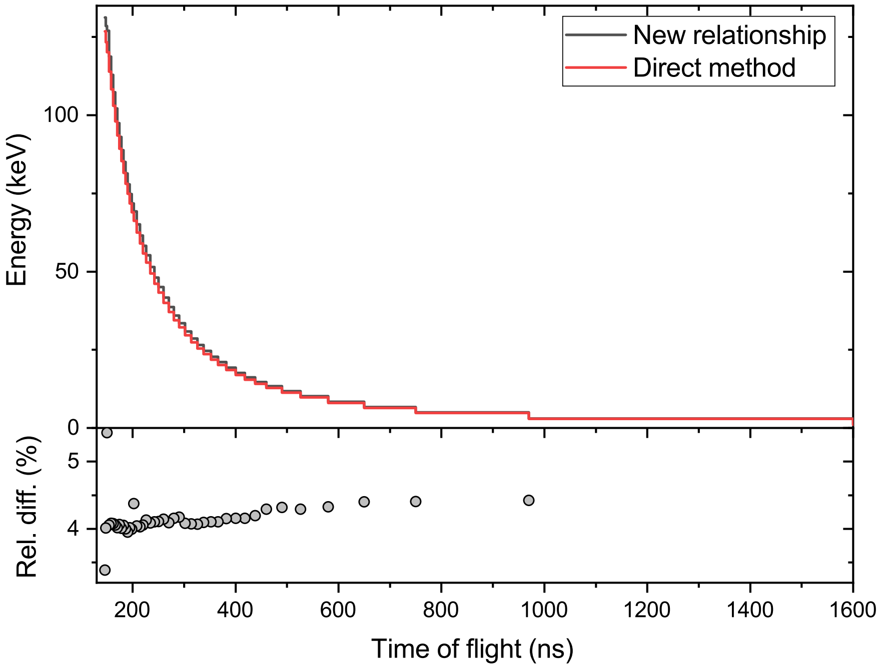

Figure 3.4: Relationship between the TOFs and energy bins determined with the response function of the experimental setup and with the direct method employing the flight path L.

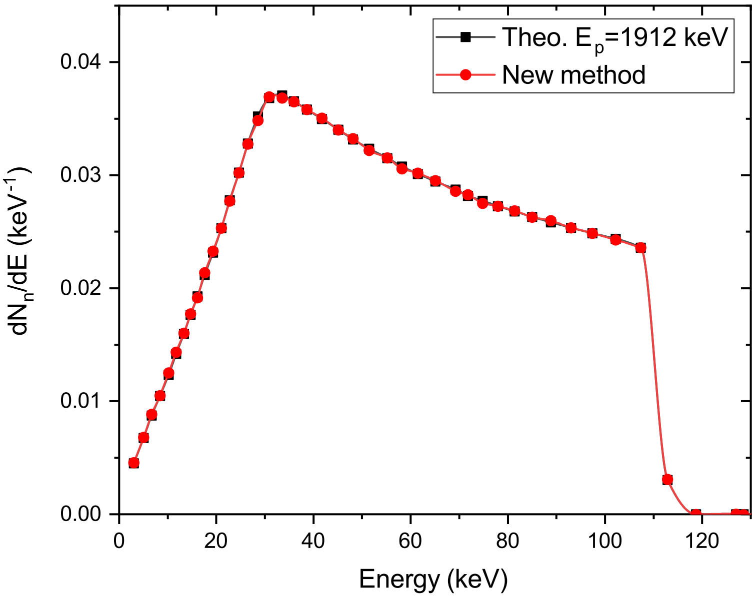

Figure 3.5: Neutron spectrum from theoretical calculations for proton energies with 1912 keV and the one obtained with the conversion method proposed in this work. Both spectra are represented with the same energy binning.

one obtained with simulated neutron TOF spectrum and the method proposed in this work, using the response matrix and a new time-energy relation. From the figure, it is possible to corroborate the good agreement between both curves. The uncertainties associated to this method are due to the precision of the Monte Carlo calculations and were taken into account in the conversion process. When this method is then applied to a TOF spectrum obtained from the experiment, the uncertainties will mainly be due to the statistical errors of the experimental spectrum. With the conversion method proposed in this work not only the mean moderation time in the detector is taken into consideration, but also its distribution in time, allowing to reproduce the emitted neutron energy spectrum from the TOF spectrum. With a system of n equations and n variables, the deconvolution of the temporal spectrum is performed and the energy spectrum is found with a unique solution of this system.

This conversion method was employed in the experimental measurement of this work in the data analysis, to obtain the emitted energy neutron spectrum from the experimental TOF measurement. The obtained results are reported in the Chapters 5 and 6.

Chapter 4

Experimental setup

4.1 CN Van de Graaff accelerator

The experiments were carried out using the CN accelerator placed at Legnaro National Laboratories of the Italian Institute of Nuclear Physics (LNL-INFN), Padua, Italy [38]. The CN accelerator is a seven meter tall (vertically installed) Van de Graaff electrostatic device. The main accelerated ion beams employed on this machine are protons, deuterium and helium, which are used in fundamental and applied nuclear physics and chemistry studies [64].

In this CN electrostatic machine, the particles are accelerated in the vertical column and directed towards the experimental beamline through a selector made by magnetic lenses and deflectors. The proton energy is established setting the voltage in the accelerator column. Via a feedback circuit, the proton energy is also established by the magnetic field from a 90° analyzing magnet. A great advantage of Van de Graaff accelerator is the excellent beam stability and high energy resolution. This CN Van de Graaff accelerator can work in continuous and in pulsed beam mode. In this work, the CN was used in pulsed beam mode.

A schematic representation of the CN accelerator control and experimental rooms is shown in Figure 4.1. There are available seven beamlines where users can perform their experiments. In our case, the beamline located at zero degrees was used. The experimental setup (represented in the figure with a green square) was placed at the end of this horizontal line, after the focalizing elements at approximately 13 m from the analyzing magnet.

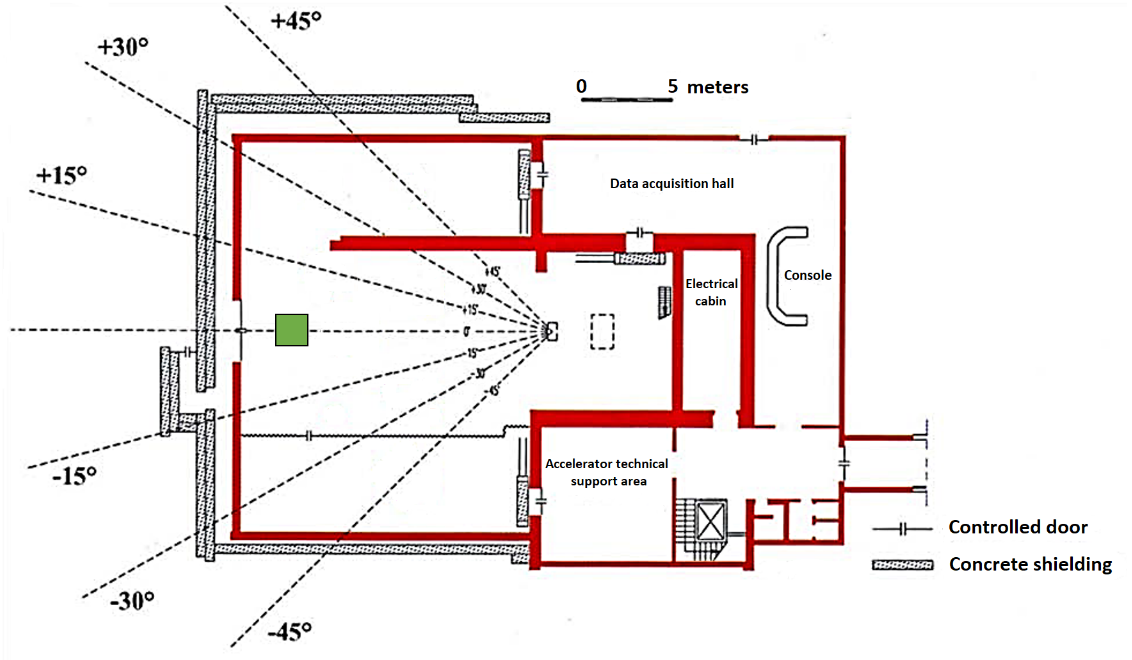

Figure 4.1: Schematic representation of the control and experimental rooms at CN accelerator.

4.2 Pulsed system

The pulsed beam is generated by introducing sinusoidal oscillations in the centering electrodes just after the ion source. The introduced oscillations cause the beam to travel following an elliptical trajectory around the hole of the beam selection diaphragm, located at the accelerating tube entrance. By moving the center of this ellipse, changing in console the Phase and Bias-Sweep parameters, its perimeter can be placed in the hole at the diaphragm. In this way, the beam leaves the terminal only for a short time interval giving rise to the pulsation.

The formation of the ellipse is calibrated at open machine. In the electrode plates, the sinusoidal oscillations are introduced in the XY plane perpendicular to the beam direction (z axis). The beam travels through the Lissajous curves by changing the amplitude and the phase of the sinusoidal waves. With the same amplitude, setting a 45° difference in phase between the oscillations the ellipse is formed. The beam generation with the wrong settings could lead to a particle bunch with the incorrect characteristics, e.g., a bunch with two peaks instead of one.

In addition to the periodic declined of the beam (which produces the pulsation), there is a buncher inside the terminal which produce a temporal compression of the pulse beam, but with a higher energy spread. The repetition rate of the generated pulsed beam is fixed at 3 MHz and, after turning on the buncher, the time resolution could be even less than 2 ns.

In general, different Lissajous curves allows to obtain pulsed beams with frequencies in sub-multiples of the main one (e.g., 1 MHz, 0.75 MHz, etc.). Since CN is an old accelerator, these frequencies are not allowed and only 3 MHz is admissible. At this repetition rate, every 333.33 ns a proton bunch arrives at the neutron production target. To travel a distance of 70 cm (flight path), neutrons of 1 keV energies spend 1600 ns. Besides, the fastest neutrons with energies of 300 keV spend 92 ns. In the detector, these time-of-flights caused an overlap of neutrons that were originated in different times (from different proton bunches); the fastest neutrons from one proton bunch with the slowest neutrons from the previous proton bunch. Due to the neutron overlap, unfortunately, 3 MHz is a high frequency to perform the desired experiment. In order to experimentally determine the neutron energy spectrum down to 1 keV, at the selected flight path, it is required a repetition rate not higher than 600 kHz (1666.67 ns period).

In order to slow down the repetition rate of the accelerator, in the zero degrees beamline a secondary pulsed beam system was developed. The secondary pulsing system is able to suppress a fraction of the main 3 MHz pulses by deflecting the unwanted ones toward a dumper. In such way it is possible to have a secondary pulsed beam with variable frequency of 1500 kHz, 1000 kHz, 750 kHz, 600 kHz, 500 kHz and lower (all multiples of 333.33 ns). The working principle of the secondary pulsed system for 600 kHz repetition rate is shown in Figure 4.2.

The outline of the secondary pulsed beam system with some of its components is shown in Figure 4.3. The system is composed by two electrodes installed into a six-way cross vacuum chamber, which provide the electric deflection of the pulsed charged particle of the beam. Each electrode is made up of an aluminum sheet properly

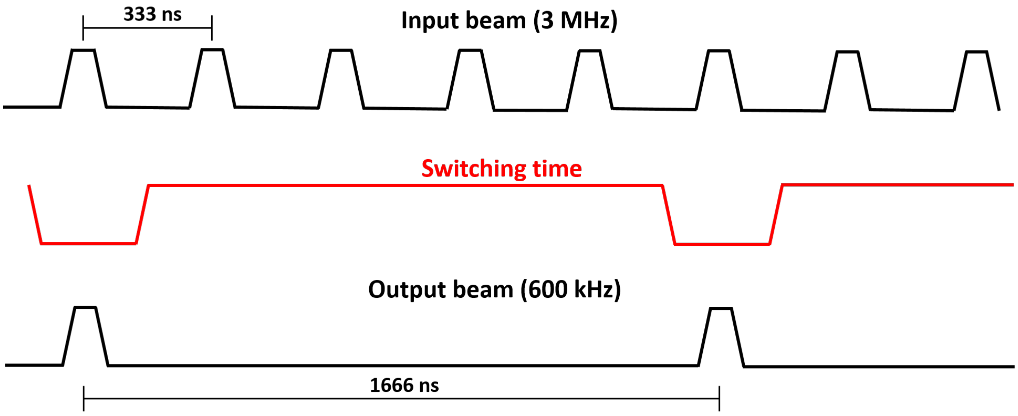

Figure 4.2: Working principle of the secondary pulsed beam system for 600 kHz repetition rate. The red line represents the timing of the used switching device.

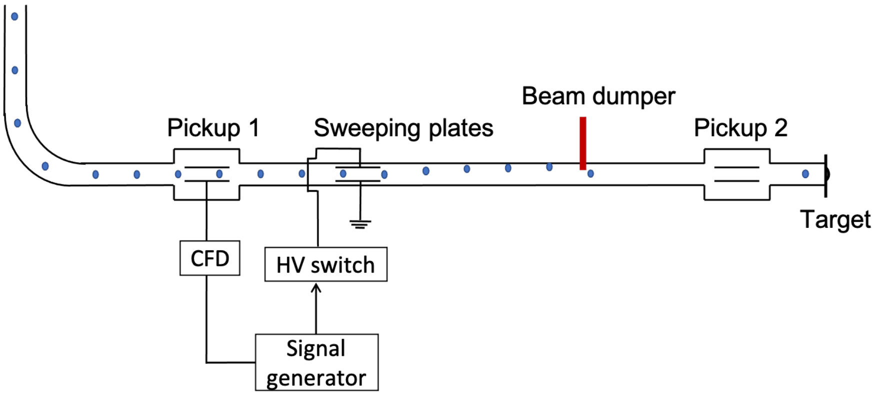

Figure 4.3: Outline of the secondary pulsed system.

shaped, in order to get the electric field inside the gap as uniform as possible. One of the electrodes is always connected to ground. The second electrode is alternatively connected to ground or to a high voltage power supply. A fast high voltage solid-state switch makes the potential alternation of the second electrode, thanks to an external trigger, following the time signal repetition rate and the duty cycle of the beam, through a Constant Fraction Discriminator (CFD) module connected to a capacitive pickup. The fast high voltage solid-state switch was supplied by the Behlke Gmbh company [65]. The main components of the secondary pulsed beam system are show in Figure 4.4 and following listed:

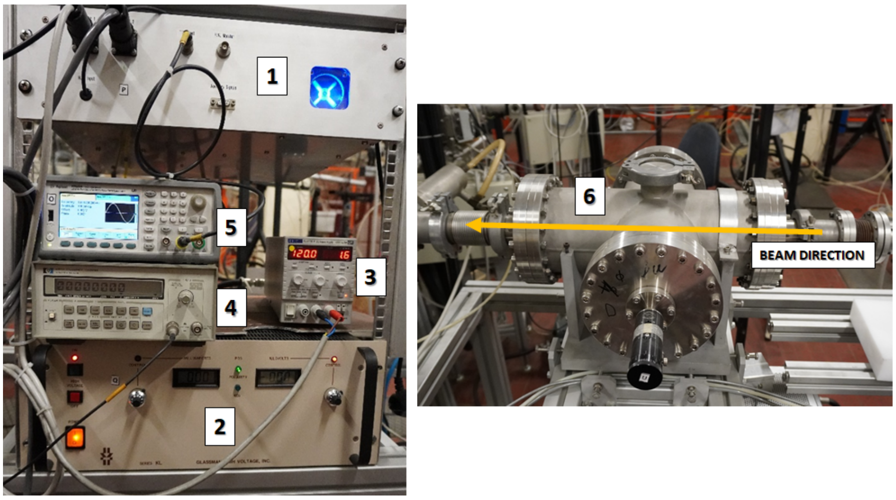

Figure 4.4: Main components of the secondary pulsed system: 1) main case with the fast switch and its cooling system, 2) high voltage power supply, 3) supplementary low voltage power supply, 4) frequency meter to check the CN accelerator 3 MHz repetition rate, 5) signal generator for time switching and synchronization; 6) Vacuum chamber where the electrostatic deflector have been assembled.

1. Main case where the switch and the related cooling system is installed;
2. High voltage power supply;
3. Low voltage (12 V) supplementary power supply;
4. Frequency meter that checks the 3 MHz repetition rate from the accelerator;
5. Signal generator to synchronize the time switching with the accelerator frequency;
6. Vacuum chamber where the electrostatic deflector is placed;
7. Beam dumper.

The waveform of the main pulsed beam (3 MHz) from the capacitive pickup 2 (Figure 4.3), seen in an oscilloscope, is shown in the upper side of Figure 4.5. In the lower side of the same figure, the 600 kHz proton pulsed beam waveform in the same pickup is shown, after the secondary pulsed beam system was turned on. In this way the good performance of the system was checked. In the figure, it is possible to observed the 1:5 relation ($1/5 \times 3$ MHz $= 0.6$ MHz, one pulse passed and arrived to the target, while four pulses were discarded).

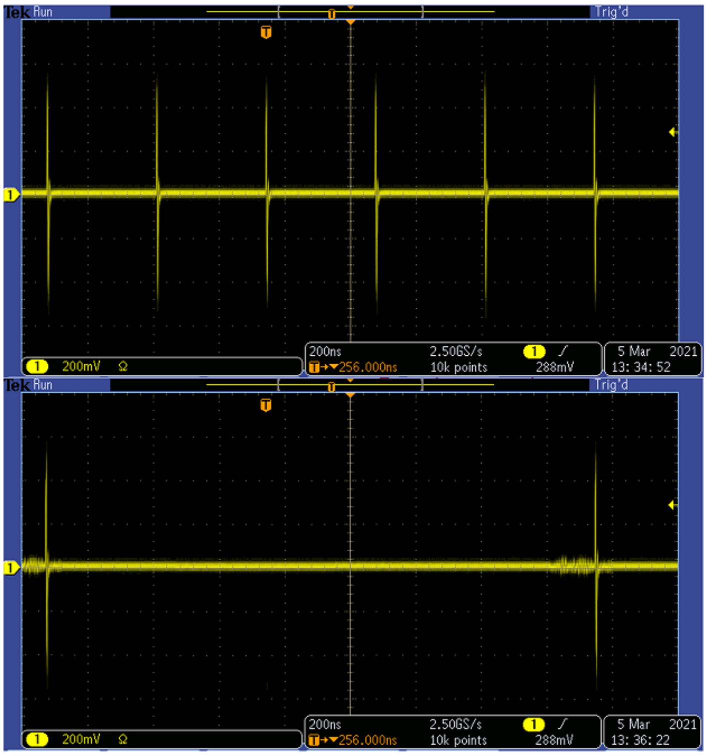

Figure 4.5: Oscilloscope view of the pickup 2 signal: (Upper) Main 3 MHz proton pulsed beam, (Lower) 600 kHz proton pulsed beam, after turned on the secondary pulsed beam system.

This secondary system was thought and developed at the Legnaro National Laboratories of the Italian Institute of Nuclear Physics (LNL-INFN). The main concern in developing such a device was related to the radio-frequency (RF) system and the needs to keep the total capacitance as low as possible. The time switch of the solid-state device depends directly on the capacitance of the load trough the time constant of the system. Moreover, the switching frequency of 600 kHz posed serious problems from the shielding point of view: the best compromise has been found to have a very compact system (to reduce capacity) and by RF noise shielding.

4.3 Li targets assembly

4.3.1 Lithium targets

All measurements were performed with metallic lithium (Li) targets. Lithium is a soft, silvery-white alkali metal that presents a low mechanical resistance and a low melting point. When lithium interacts with the air, quickly reacts with the oxygen and it is converted into lithium oxide. For this reason, is not possible to manipulate the lithium on the air atmosphere. The lithium used in the experimental setup was stored in liquid paraffin (mineral oil), and when handling and manipulation was implied, it was always processed in an argon gas filled glovebox.

A mechanical process was employed to produce the Li targets. The following steps were carefully performed inside the glovebox to obtain one target: (1) the Li was cleaned and dried, (2) the natural lithium metal bar was peeled off and cut into a small slice, (3) the slice was rolled down until the approximately desire thickness of the foil was obtained and measured with the caliper, and (4) the foil was attached to the copper (Cu) backing by pressing them, between a male and a female mold, producing a lithium layer of 100 μm. Two Li targets were produced for the experiment (Figure 4.6a). One was used for: (a) the accelerator calibration (Section 4.7) and (b) the neutron time-of-flight (nTOF) measurement with a $E_p = 1912$ keV (Chapter 5). The second one was used for the Maxwell-Boltzmann neutron spectrum measurement (Chapter 6).

Figure 4.6b shows the proton penetration inside the target, (100 μm of Li plus the first 20 μm of Cu backing). The proton penetration was calculated with the Stopping Power and Range of Ions in Matter (SRIM 2013) software [60], employing as input parameters the proton energy, the 100 μm thickness of the target material (Li) and the layer thickness of the Cu backing (300 μm). From the figure, it is visible how the proton beam is stopped approximately in the first 10 μm of the Cu backing.

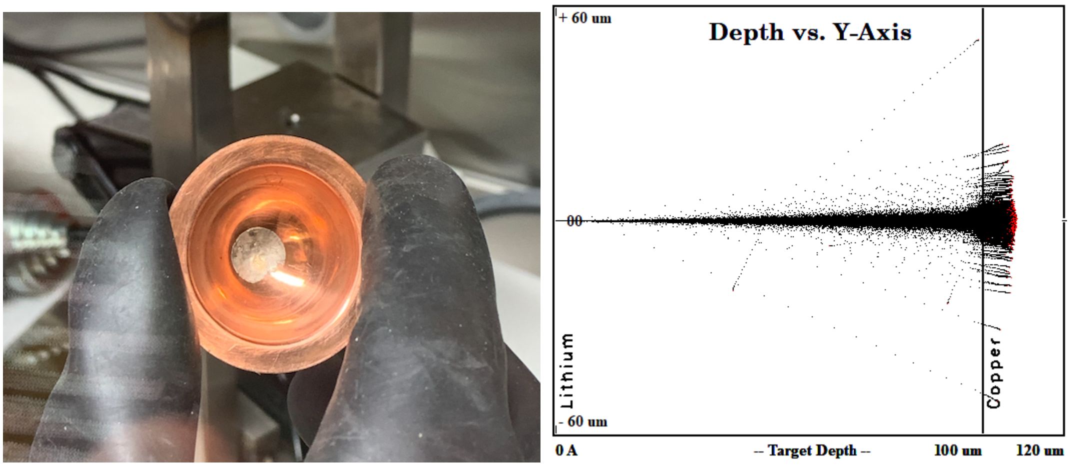

(a) (b)

Figure 4.6: a) Lithium target produced in the glovebox. b) Proton penetration inside the target calculated with the SRIM 2013 software [60] for 100 μm of Li plus the first 20 μm of Cu backup, and proton energy of $E_p = 1912$ keV.

With this thickness the protons were completely stopped in the Cu backing avoiding further power deposition inside the lithium. This is an important aspect because of the low melting point (180°C) of Li and its low thermal conductivity, compared to other metals.

4.3.2 Target assembly

The target assembly is shown in Figure 4.7. It is composed by: (1) removable Cu backing in which the Li is attached; (2) small PVC tube to isolate the target from the rest of the beam pipe; (3) collimator: made of two tantalum foils with 5 mm diameter aperture, distant 7.1 cm one of the other; (4) a micro-metric valve that allows the slow extraction of argon from the target assembly; (5) a second gate; (6) removable aluminum foil for the proton beam shaper. As shown in the figure, the gate valves are coupled to the target assembly next to the collimator, which allows the target not to be exposed to the air. The target was always kept either under argon atmosphere or in vacuum. Once finished the experiment, the radioactive target was removed and properly stored. The Cu backing was cooled by applying an air flow to its external face. During the experiment a vacuum level of 10^{-6} mbar was reached at the target position. The Cu backing, the PVC tube and the collimator were electrically isolated. The current from the target (1) and the collimator (3) were directly read in console and registered when needed in the experiment.

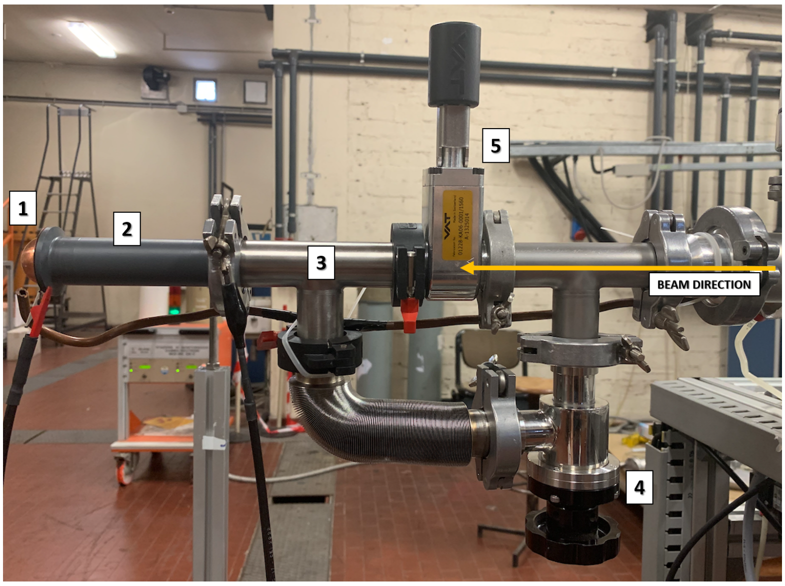

Figure 4.7: Li target assembly placed at the end of the beamline with: (1) removable Cu backing in which the Li is attached, (2) isolated small PVC tube, (3) collimator, (4) a micro-metric valve, (5) a second gate.

4.4 Detectors

Because of their weak interaction with matter and their large dynamic range in energy, in general, neutrons are more difficult to detect than γ rays. The cross section of the ^{6}Li(n,α)^{3}H reaction reaches 941 barns for thermal neutrons. Because of this, lithium (Li) loaded glass scintillation detectors have been successfully used in detecting thermal neutrons, since their development in the late 1950's. These type of detectors are silicate-based glass into which a few weight percent of lithium have been incorporated. A small percentage of an activator species, usually cerium in the form of an oxide (necessary to produce the fluorescence effect) is also present in the scintillator. Lithium-glass detectors are employed to detect the secondary charged particles derived from the ^{6}Li(n,α)^{3}H reaction. The alpha particles (2.05 MeV) and the tritium ions (2.73 MeV) lose their energy within the scintillator material in the interaction point proximity, and this gives rise to the emission of light. This output light is then detected with a photomultiplier tube (PMT). Pulses from the PMT are fed directly to the data acquisition system (DAQ).

Since Li-glass detectors do not have very good inherent energy resolution, they are not often employed for neutron spectral measurements. However, they offer the advantage of being a relatively fast scintillator, and handled reasonably high count rates. Because of these characteristics, the Li-glass detectors are widely employed in applications where the timing is crucial. In this experiment, the Li-glass detectors were chosen exactly for this purpose: measure the experimental neutron time-of-flight spectrum.

Different ^{6}Li-glass detectors were employed during the experiment. Three detectors purchased from Scionix [66] were used for time-of-flight (TOF) measurements. Two one inch (2.54 cm) thick detectors and one half inch (1.27 cm) thick were used. A fourth 3 mm thick Li-glass detector was also used, but as neutron counter monitor for normalization. This detector was also employed to check the beam and the target stability during the experimental measurement.

As oppose to the idealized one-to-one correspondence between nTOF and neutron energy (Equation 3.1), the neutron flight time can vary, mainly due to the variable moderation time inside the detector. In Chapter 3 a novel method to convert the measured neutron time-of-flight spectrum to an energy spectrum was explained. For this, the calculation of the detector response matrix is mandatory. This matrix is calculated by Monte Carlo simulations, with the MCNPX code [61], determining the neutron time distribution inside the detector for monoenergetic neutron sources. In the simulations, the detector geometry and materials composition are included. The conversion method relies on the response matrix, hence the importance of knowing precisely the geometry and materials of the detector.

The detector geometry and materials composition were provided by the manufacturing company (Scionix). Furthermore, the characteristics of the optical interface (Quartz) from the photomultiplier tube (PMT model ETL9214QKB) were provided by the company ET Enterprise [67]. In a first attempt to know the detector composition, a radiography of one Li-glass detector (one inch thickness) was realized. The detector's radiography is shown in Figure 4.8. Zooming in the radiography, some of the inside components are visible e.g., the crystal scintillator (Li-glass), the PMT components, the PMT quartz window and the magnetic shielding (μ metal). The radiography allowed to crosscheck the information provided by the Scionix company. The detector layout and chemical composition employed in the MCNPX simulations are shown in Figure 4.9 and Table 4.1, respectively.

4.4.1 Efficiency

The intrinsic efficiency of a detector is defined as the ratio between the number of detected and incident particles. The intrinsic efficiency of the Li-glass detector as a function of the neutron energy was calculated by simulations with the MCNPX code. The already mentioned geometry and detector composition (Figure 4.9 and Table 4.1) were taken into account when simulations were performed. Also, the detector support, the room floor and the Li target were included in the simulations.

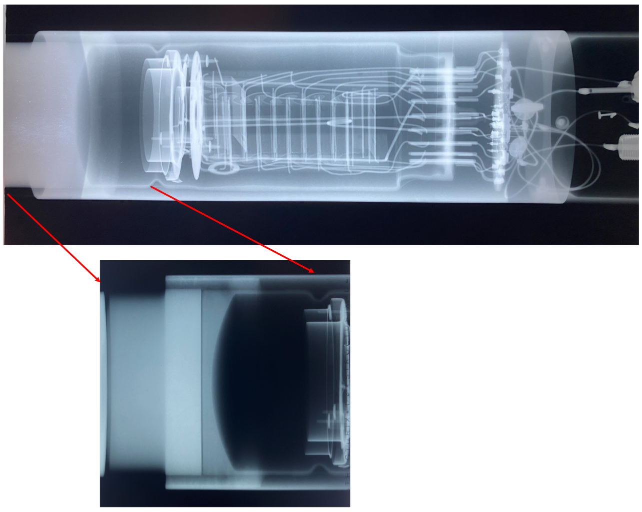

Figure 4.8: One inch thickness Li-glass detector radiography.

Table 4.1: List of materials and densities in the Li-glass detector. ^{6}Li enrichment is 96%.

Component	Chemical composition	Density (g/cm^3)
Aluminum	Al alloy	2.69
Teflon	$(C_2F_4)_n$	2.20
Glass	SiO_2 56%, MgO 4%, Ce_2O_3 4%, Al_2O_3 18%, $^6Li_2O$ 18%	2.60
Optical RTV	H 8.2%, C 32.4%, 21.6%, Si 37.8%	1.03
Quartz	SiO_2	2.65
μ-metal	C 0.02%, Mn 0.50%, Si 0.35%, Ni 80.00%, Fe 14.93%, Mo 4.20%	8.74
Glass fiber tape	SiO_2 56.0%, ZrO_2 14.5%, B_2O_3 8.0%, AL_2O_3 5.5%, F_2 5.0%, TiO_2 6.0%, Fe_2O_3 5.0%	1.00
Epoxy	$C_{18}H_{21}ClO_3$	1.20

For each detector type, monoenergetic neutrons with energies from 1 keV to 1 MeV were simulated as neutron sources. The neutron capture cross sections are contained in the MCNPX libraries (ENDF/B-V database). In the detector, the neutron capture reaction (n,t) is produced and the tritium production is accounted. With the *Tally 4* and the *FM* card, the tritium production (equivalent to the number of neutrons) counted by the detector per incident particle was recorded, together with all other charged particle neutron induced reactions in all elements. Figure 4.10 shows the results of these simulations for both detectors, one inch and half inch thickness. As observed in the figure, the neutron detection efficiency increases with the thickness of the Li-glass, due to the presence of more active material.

The efficiency of the Li-glass detector is essentially determined by the ^{6}Li(n,α)^{3}H

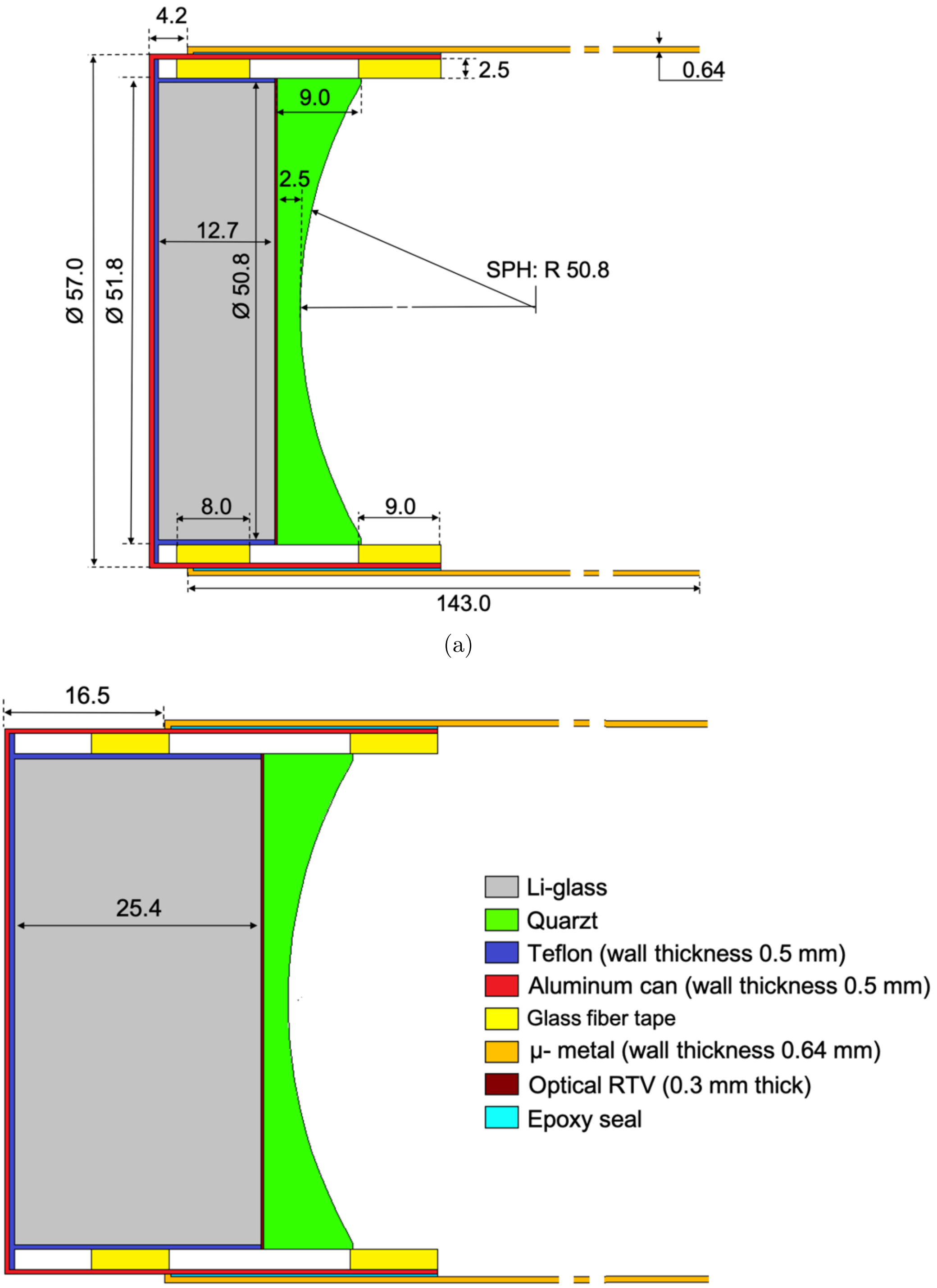

(a)

(b)

Figure 4.9: Layout of the Li-glass detectors: a) Half inch (12.7 mm) thickness glass detector; b) One inch (25.4 mm) thickness glass detector. All quantities are in millimetres.

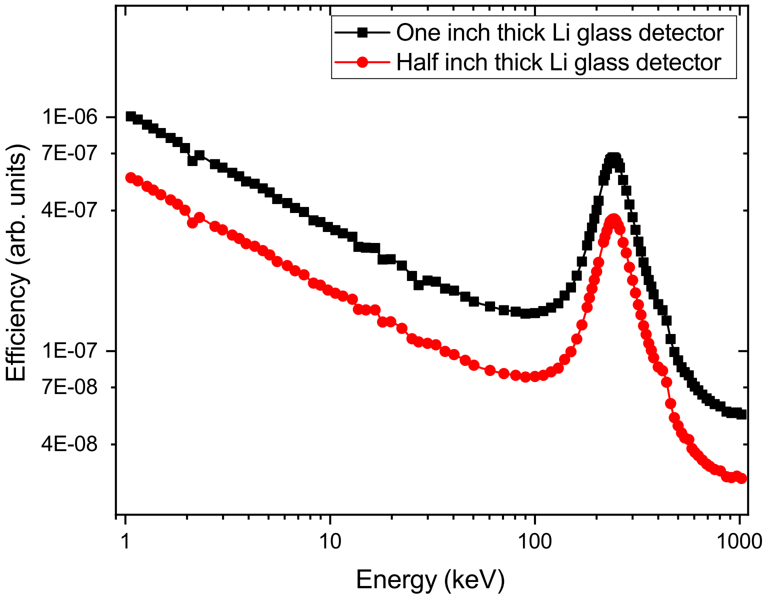

Figure 4.10: Intrinsic efficiency for neutron detection with one inch and half inch thick Li-glass detectors calculated with the MCNPX simulation code [61].

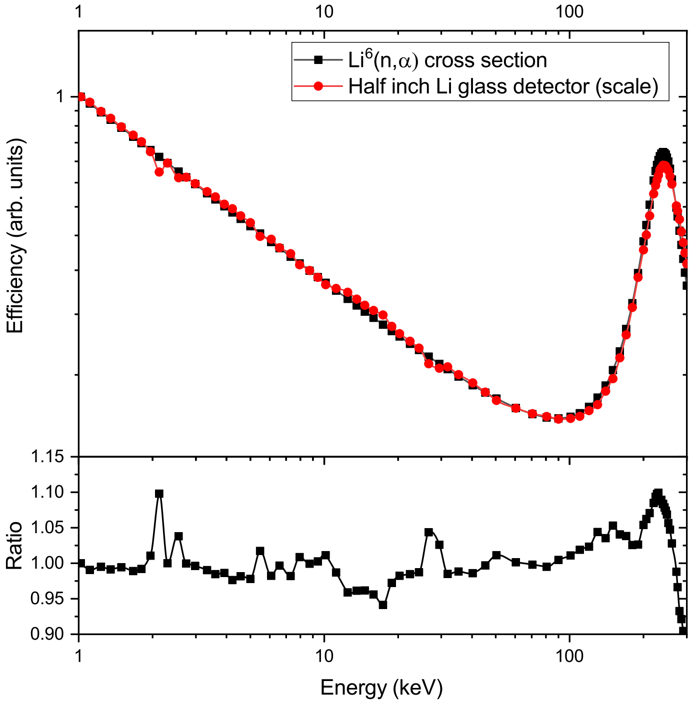

Figure 4.11: Efficiency of the half inch thick Li-glass detector calculated with the MCNPX simulation code [61] compared with the ^{6}Li(n,α)^{3}H reaction cross section [68]. The ratio of the two curves is shown in the lower panel.

reaction cross section. The cross section from this reaction and the calculated efficiency for the half inch detector, is shown in Figure 4.11. The cross section corresponds to the ENDF/B-V database [68]. The ratio between the two curves is shown in the lower panel of the figure. Some peaks appear in the region between 10-30 keV. In the TOF-energy conversion method the efficiency is contained in the response matrix. With a detailed model of the detector as input in the simulations, the effect of the structural materials in the setup were considered.

4.5 Acquisition system

Two desktop digitizers, purchased from the CAEN company [69], were employed as experimental Data acquisition system (DAQ). The digitization and real data processing of signals from detectors and pickups were carried out with these digitizers. The first DAQ is the desktop DT5751, shown in Figure 4.12a. This Waveform Desktop Digitizer is a 4 channels module, with 1 Vpp (voltage peak-to-peak) input dynamic range, 10 bits resolution and 1 GS/s sampling rate simultaneously on each channel. The second DAQ is the desktop DT5730SB, shown in Figure 4.12b. This DAQ is a 8 channels digitizer, with 14 bit resolution, and 500 MS/s sampling rate. The input dynamic range can be selected to 2 Vpp or 0.5 Vpp. In both digitizers, each channel can generate a self-trigger when the input signal goes under/over a programmable threshold.

The DT5751 module was employed to acquire and stored the experimental waveforms for the proton time-of-flight (proton time-of-flight (pTOF)) measurements (Section 4.6). The CAEN WaveDump console application [70] was used to process the waveform plots.

The DT5730SB module was employed for the neutron time-of-flight (nTOF) spectrometry measurement. To acquire the TOF data, the DAQ was coupled and controlled with the CAEN Multi-Parameter Spectroscopy Software (CoMPASS)

(a) (b)

Figure 4.12: Front view of the CAEN desktop digitizers employed in the experiment: a) DT5751; b) DT5730SB [69].

[71]. The CoMPASS software has some characteristics: (1) it is a user friendly interface; (2) can manage multiple boards; (3) can make event correlation between different channels (hardware and/or software); (4) applies energy and Pulse Shape Discrimination (PSD) cuts; (5) calculates and shows the statistics; (6) saves the output data files (raw data, lists, waveforms, spectra) and (7) uses the saved files to run off-line post-processing data [72]. The energy and timing experimental data from each detector through a field-programmable gate array (FPGA) were adquired and saved with the CoMPASS software. The use of FPGA allows a much higher acquisition rate.

The DT5730SB module has the possibility of implementing the digital Constant Fraction Discrimination (CFD). Besides, it has a better dynamic for low detectors signals and better energy resolution when compared with the DT5751 module. Due to these advantages, the DT5730SB was employed for the nTOF measurement. The higher (2 ns) sampling time, compared to the other digitizer (1 ns), is not a concern since it is comparable with the time resolution of the proton beam. This DAQ coupled with the CoMPASS software allowed to measure the nTOF spectra of four detectors at the same time, resulting in more counting statistics in the experiment. At the contrary, these specifications were not necessary when the pickup signals were processed in the pTOF measurements. Instead of using the CoMPASS software, the DT5751 module was coupled with the WaveDump console application, acquiring the pickup signal waveforms with a better time resolution.

4.6 Proton time-of-flight spectrometry

The time-of-flight spectrometry of the proton pulsed beam (pTOF) was implemented to determine the proton beam energy and its distribution. The time used by a bunch of protons to travel a distance between two points in the beamline was determined for this purpose. With this time and the distance between these two points, the velocity (and therefore the energy) of the protons flying in that bunch was calculated.

Figure 4.13 outlines the working principle of the pTOF measurement. Two beam capacitive pickups were inserted in the horizontal beamline to sense the pass of the proton bunch. One of them, called pickup 1, was inserted immediately after the analyzing magnet of the accelerator. The second one, called pickup 2, was placed at the end of the beamline, near the target. The idea with the capacitive pickups is to measure on an isolated metal plate the image current induced by the electric field of the beam particles, giving information about the pulses timing and their width without intercepting the beam [73]. The waveforms in the capacitive pickups when the proton pulsed beam passes through them were amplified and recorded by the CAEN DT5751 digitizer and later analyzed. The time difference of signals taken between both capacitive pickups was then measured and corrected for the delay time of cables and electronics.

To avoid systematic errors, the time from the capacitive pickup signal for each proton bunch was determined as the zero crossing (pointed in Figure 4.14). A lot of work has been done to find the best part of the pickup signal which is best suitable as time reference. We found that the zero crossing is the most stable time reference.

The zero crossing time was calculated with bisection method by interpolating with

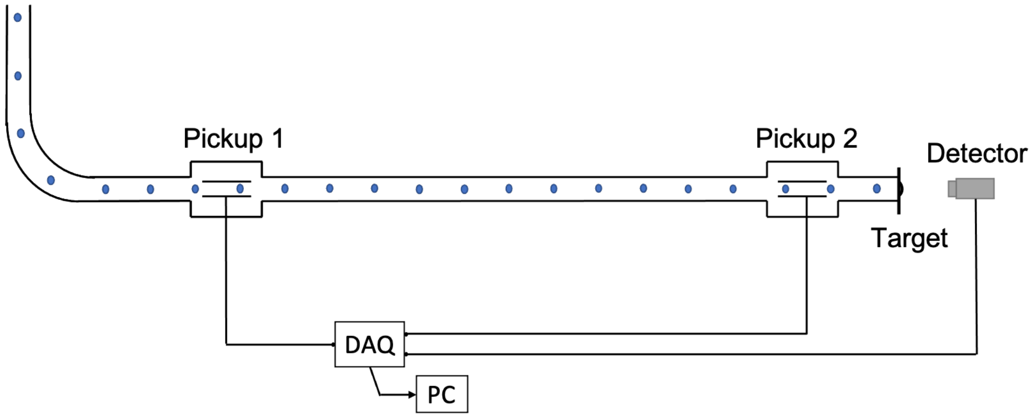

Figure 4.13: Schematics of the proton time-of-flight spectrometry (pTOF) measurement. Pickup: capacitive pickup to measure the image current induced by the electric field of the beam particles, DAQ: data acquisition system, PC: computer, Target: Li target, Detector: Li-glass detector.

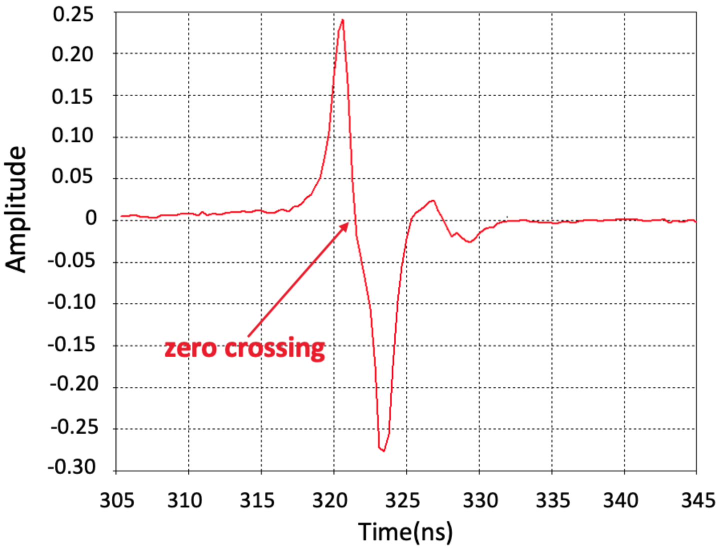

Figure 4.14: Typical signal from a pickup.

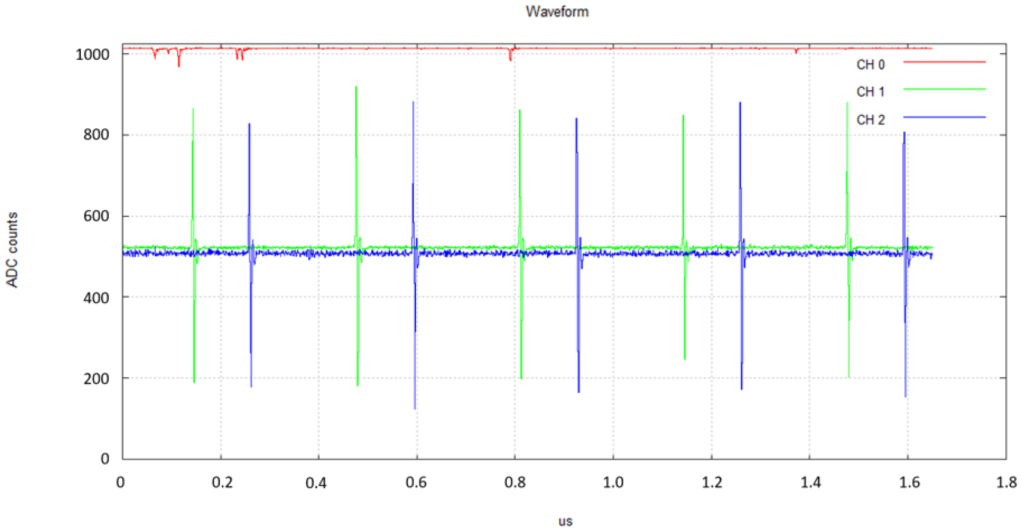

Figure 4.15: Waveforms from pickups signals during the proton time-of-flight (pTOF) measurement acquired with the CAEN WaveDump application [70]. CH0 corresponds to the trigger detector signal, CH1 and CH2 correspond to the signals from the pickups 1 and 2, respectively.

a cubic spline the voltage values from the digitized signals, imposing an accuracy of 1 ps. Figure 4.14 shows the signal from the pickup 2 as digitized. Figure 4.15 shows the digitized waveform signals from the pickups during the pTOF measurements, with a 3 MHz repetition rate, using the Gnuplot utility. In the figure, CH0 corresponds to the signal that triggers the acquisition (the signal from one of the detectors), and CH1 and CH2 correspond to signals from the pickups 1 and 2, respectively. The time difference between the signals coming from the pickups due to the travel time of the proton bunch can be observed. The TOF of a proton bunch (t) from pickup 1 to pickup 2 is equal to the difference between both signal arrival times plus the signal delay between both pickups due to the cable and the preamplifier (Figure 4.13):

$$t = t_{pickup2} - (t_{pickup_1} - t_{delay}) \tag{4.1}$$

The $t_{pickup2}$ and $t_{pickup1}$ were determined from the zero crossing time of the pickups 1 and 2 signals, respectively. The t_{delay} was precisely determined as described below. The cable with the preamplifier from pickup 1 was unplugged and taken near the pickup 2 and the DAQ. The pickup 2 signal was split and both cable plus preamplifiers (from pickup 1 and pickup 2) were simultaneously fed with this signal. Their output signals were recorded with the same digitizer (DT5751) and the time difference between the two lines was measured. Since is the same input signal for both lines, if no delay were present both signals should appear at the same time. From this measurement, a time delay of 0.133 ± 0.09 ns was determined.

The proton kinetic energy is calculated as:

$$E_p = M_p c^2 \left[\frac{1}{\sqrt{1 - \left(\frac{x}{ct}\right)^2}} - 1 \right] \tag{4.2}$$

where $M_p c^2$ is the proton mass at rest, c the speed of light, t (Equation 4.1) is the time used by the protons to travel the distance x. The presence of focusing magnets and lenses in the beamline can modify the proton beam trajectory (proton flight path). Because of that, the distance x it is not necessarily the geometrical distance between the capacitive pickups. In order to determine precisely the beam energy and thus the flight path x, a scan of the reaction threshold was performed. This procedure is described in Section 4.7.

4.7 Accelerator calibration

In the ^{7}Li(p,n)^{7}Be reaction, neutrons are produced when proton energies are higher than the reaction threshold (1880.6 keV). To properly correct the proton energy from the accelerator, a scan near the threshold of the ^{7}Li(p,n)^{7}Be reaction was performed and the neutron emission was measured. The scan was achieved decreasing the magnetic field (B) of the analyzing magnet until the neutron peak in the detector pulse height spectrum disappeared. The detector signals were analyzed with the DT5730SB digitizer (Section 4.5). The detector pulse height spectra were acquired with the CoMPASS software [71]. In this measurement, the proton pulse beam had a frequency of 600 kHz and approximately 4 ns width proton bunches.

To measure the neutron emission, a Li-glass detector (one inch thickness) was placed in front of the target at zero degrees relative to the proton beam direction (Figure 4.16). The detector was covered with 2.4 cm of lead and 2.0 cm of high-density polyethylene. The polyethylene was added to increase the detection efficiency of 29.7 keV neutrons which is the energy of neutrons at the reaction threshold. The lead layer was included to reduce the high amount of γ rays produced by the ^{7}Li(p, p'γ)^{7}Li and ^{7}Be(p,γ)^{8}Be reactions. The Li-glass detector gives two peaks in the detector pulse height spectrum, one from the detection of γ rays coming from the ^{7}Li(p, p'γ)^{7}Li reaction, and the second one correspond to the detection of the ^{6}Li(n,α)^{3}H reaction products (see Figures 2.2, 5.3 and 5.4).

A quick scan of the threshold was performed until the neutron peak in the detector pulse height spectrum disappeared. In first approximation, the value of B, where the neutrons disappeared, was taken as the magnetic field at the reaction threshold. This value was found equal to 0.27881 T. Then, the magnetic field of the accelerator analyzing magnet was changed in steps of $\sim$0.00002 T, from 0.27915 T to 0.27869 T, and the detector energy spectrum acquired. For each magnetic field measurement, the detector pulsed height spectrum, the current on target and the proton time-of-flight distribution (TOF) were simultaneously acquired and stored.

The detector pulse height spectra acquired with the CoMPASS software, for five magnetic fields, are shown in Figure 4.17. In this figure, each spectrum was normalized to the γ peak value. The first peak corresponds to γ rays and the second one to the emitted neutrons. As can be seen in the figure, the neutron peak is well separated from the gamma region, allowing a good discrimination between the particles. It is important to remark that higher magnetic field means higher proton energy and therefore, higher neutron yield. This is well represented in the figure when the number of detected neutrons is higher with the increase of the magnetic field. The background was taken as the pulse height spectrum obtained with a magnetic field equals to 0.27869 T, when no neutrons were produced. For each magnetic field measurement, the current on target was also registered. The total charge on target was calculated multiplying each value of registered current with the respective time of each measurement. After background subtractions, the area under the neutron peak was calculated and divided by the total charge on target.

The neutron yield, as referred in Equation 2.15, is a function of the (p,n) reaction cross section, the proton stopping power in the target and a term that contains the Gaussian-like proton energy distribution. The result from the scan of the reaction threshold by counting the neutron emission is reported in Figure 4.18. The first magnetic field where the neutron counts is different than zero, does not necessary means that this is the reaction threshold. Even if the mean proton energy is below

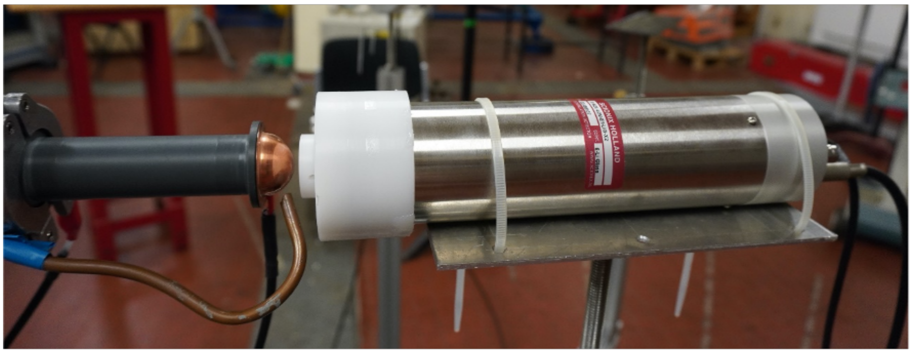

Figure 4.16: Experimental setup for the neutron emission measurement, used for the calibration of the CN Van de Graaff accelerator.

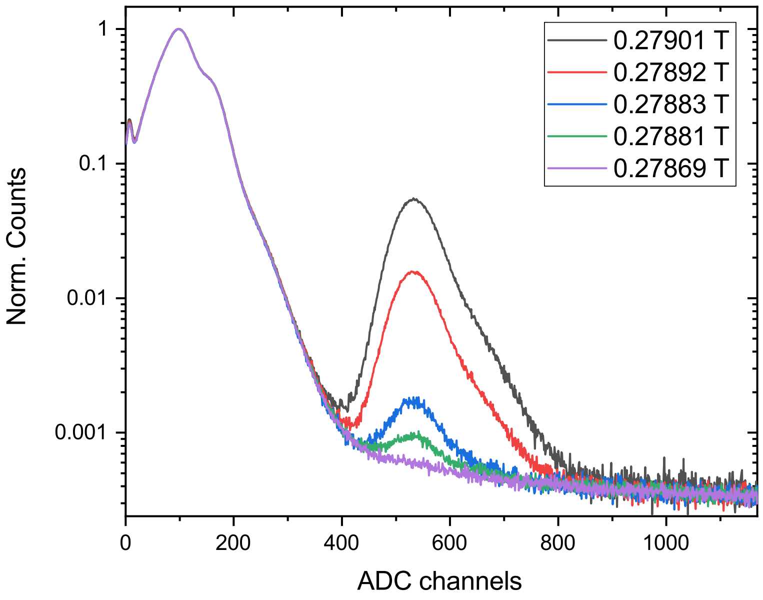

Figure 4.17: Detector pulse height spectrum acquired with the CoMPASS software for different magnetic fields of the accelerator analyzing magnet.

the reaction threshold, due to the beam energy spread, there are some protons with energy higher than the reaction threshold (protons in the tail of the distribution) and, neutrons are produced and counted by the detector. For a monoenergetic proton beam impinging on a thin lithium target, the first derivative of this curve $d\mathrm{N_n}/d\mathrm{B}$ gives directly the reaction cross section. With the second derivative $d^2\mathrm{N_n}/d\mathrm{B}^2$ the value of B at threshold is found. Since there is a contribution of a thick Li target and the energy spread of the beam, the second derivative of Figure 4.18 gives the closest reaction threshold value. The magnetic field at the reaction threshold was calculated as the maximum of the second derivative ($d^2\mathrm{N_n}/d\mathrm{B}^2$) of the curve, giving a value of $\mathrm{B} = 0.27883$ T. The red line in the figure represents the obtained value of magnetic field at the reaction threshold.

The obtained magnetic field at the reaction threshold, where the proton energy is 1880.60 keV, was used to adjust the flight path (x) in the proton time-of-flight spectrometry (pTOF) measurement. The mean value of the proton TOF distribution obtained with this B value, the speed of light, the proton mass at rest and the proton energy ($\mathrm{E}_p = 1880.60$ keV), were used as parameters in the equation for the proton energy determination (Equation 4.2). Solving this equation, the proton flight path resultant value was 9.8167 ± 0.0018 m. The proton energy distribution with pTOF, after the flight path calculation, is shown in Figure 4.19. As expected, the mean

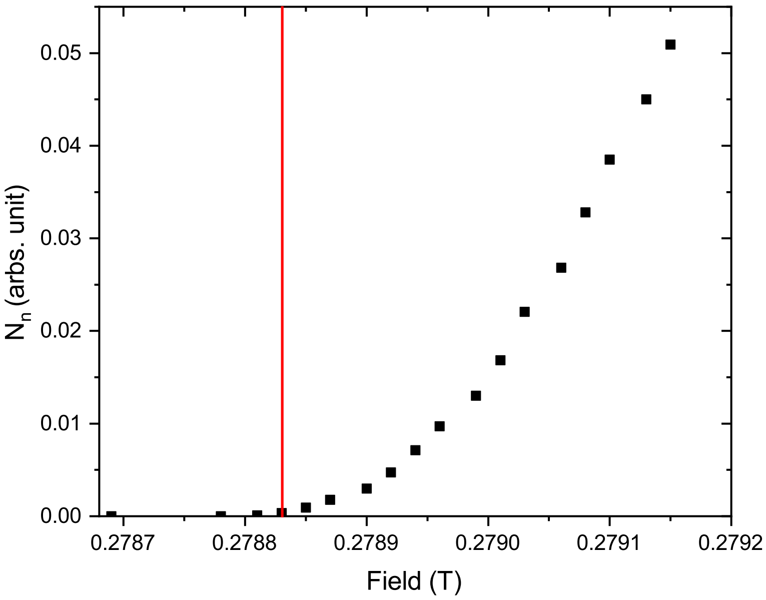

Figure 4.18: Scan of the ^{7}Li(p,n)^{7}Be reaction threshold.

proton energy for the Gaussian distribution fit was $E_p = 1880.60$ keV and the full width half maximum (FWHM) 0.69 keV.

For each magnetic field measurement the proton energy per every event was determined, evaluating in Equation 4.2 the calculated proton flight path ($x = 9.8167 \pm 0.0018$ m) and the time from the pickups 1 and 2. More than 2x10^{5} protons were collected and analyzed for each measurement. Proton energy distributions for different magnetic fields are shown in Figure 4.20a. Each proton energy spectrum was normalized to unit area. For the pulsed beam used in this determination, the FWHM of the proton distributions was around 0.8 keV. The quadratic relation between the magnetic field and the proton energy is shown in Figure 4.20b. The proton energy is calculated as the mean energy in the pTOF distribution. There is a good correlation between the experimental data and the calculated fit. The small deviations could be associated to the uncertainty on the magnetic field value determination, due to approximations in the measurement instrument (Gauss meter). The pTOF measurement allowed to measure not only the produced proton beam energy but also its distribution, which is another magnitude that plays an important role in the present experiment.

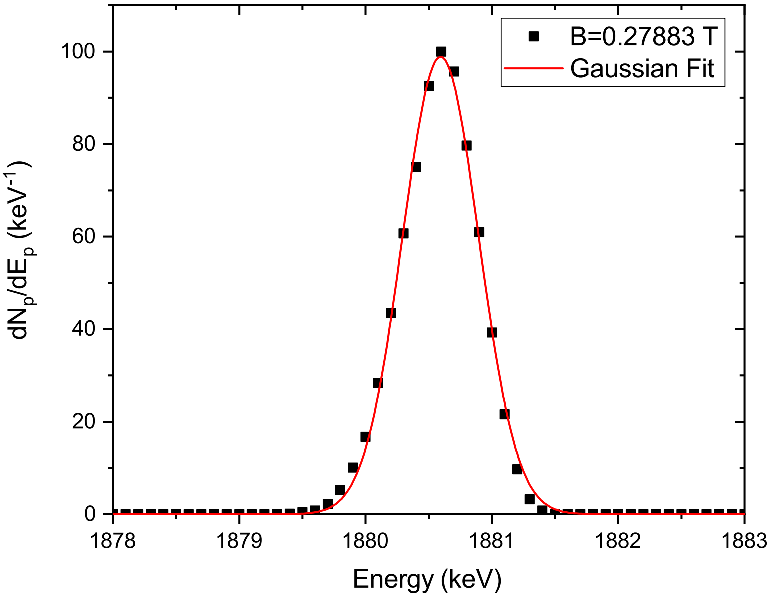

Figure 4.19: Proton energy distribution at the reaction threshold measured with proton time-of-flight spectrometry.

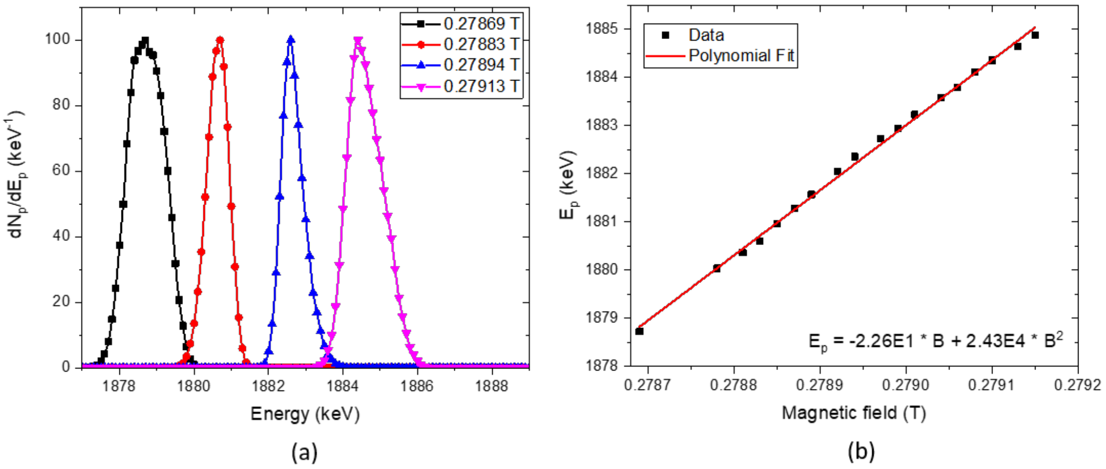

Figure 4.20: a) Proton energy distributions for different magnetic field values measured with the time-of-flight technique (pTOF). b) Relationship between magnetic field and proton energy.

Chapter 5

Neutron time-of-flight measurement with a proton energy of 1912 keV

With a similar experimental setup as Lederer *et al.* [45], the neutron spectrum at zero degrees was measured. The aims of this measurement was to compare the data generated with the method for TOF to energy conversion, proposed in this work, with some experimental data found in the literature, as well as testing the energy calibration of the accelerator.

After the accelerator calibration, the measurement was performed. The proton pulse beam had a frequency of 600 kHz. Using proton time-of-flight spectrometry (pTOF) (see Section 4.6), a proton energy of 1912 keV was set. Figure 5.1 shows the experimental setup for this measurement. A proton beam current of about 50 nA was measured in the lithium target. The neutron time-of-flight (nTOF) with the one inch thickness Li-glass detector placed at 71.99 ± 0.01 cm from the target at zero degrees relative to the proton beam direction was measured. The DT5730SB digitizer with the CoMPASS software [71] were used for data acquisition and the respective height pulse spectrum and TOF spectrum were saved for the post-processing analysis.

5.1 Proton time-of-flight spectrometry

Changing the magnetic field of the accelerator analyzing magnet, a mean proton energy of 1912 keV was set with proton time-of-flight spectrometry (pTOF) (see Section 4.6). The signals from the capacitive pickups 1 and 2 were passed to the desktop digitizer DT5751. The pTOF was calculated and the resulting time distribution of the proton energy was determined using the Equation 4.2. The proton energy distribution measured with pTOF is shown in Figure 5.2. The Gaussian fit

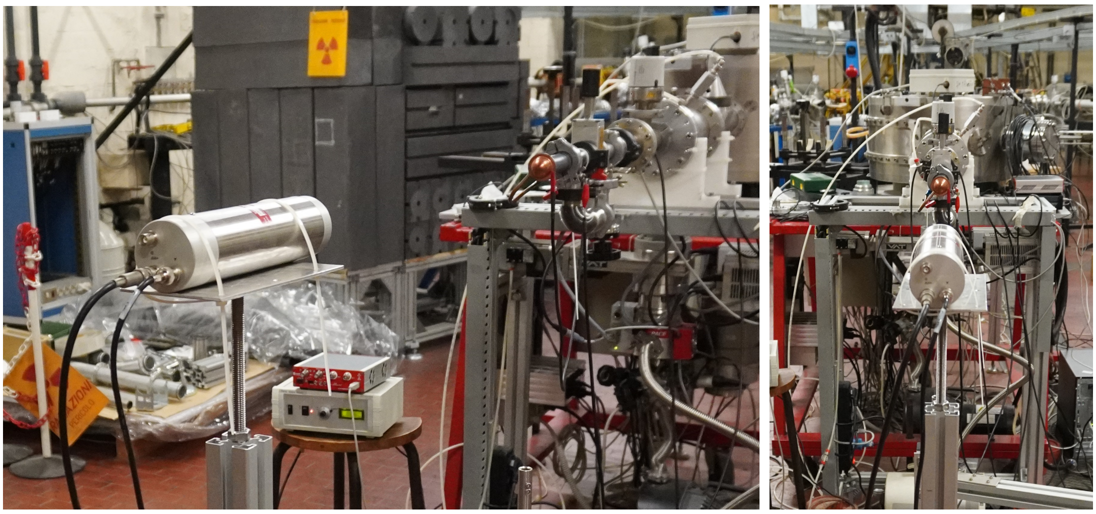

Figure 5.1: Experimental setup for neutron time-of-flight measurement with a proton energy of 1912 keV from two different points of view. Detector located at 71.99 ± 0.01 cm from the target at zero degrees relative to the beam direction.

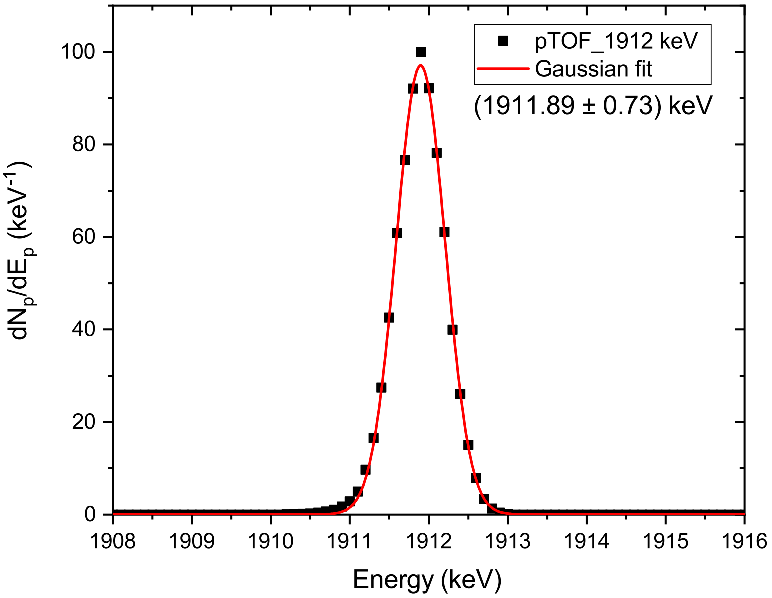

Figure 5.2: Proton energy distribution determined with proton time-of-flight spectrometry (pTOF).

for the distribution gives a mean proton energy of 1911.89 keV with a full width half maximum (FWHM) of 0.73 keV. With this proton energy distribution, the neutron time-of-flight measurement at zero degrees was then performed.

5.2 Neutron spectrum analysis

The neutron time-of-flight (nTOF) was acquired with the desktop digitizer DT5730SB coupled with the CoMPASS software (see Section 4.5). The signals from the capacitive pickup 2 and the one inch Li-glass detector were passed to the digitizer and a coincidence windows of 1.66 μs was set in the CoMPASS software. This coincidence value was calculated as the inverse of the frequency of the proton pulsed beam (1/600 kHz). An energy cut around the neutron peak in the detector pulse height spectra was applied in the software window, thereby eliminating most of the stray gamma events and thus reducing the count rate. The two dimensional plot Pulse height *vs* Time-of-Flight (TOF) is shown in Figure 5.3. In the figure, each black point represents a detected particle (neutron or gamma). For better visualization only 150000 events are shown in the figure. The vertical pattern, almost a line, are the γ rays that arrives first in time, since they travel with the speed of light. The neutrons are the horizontal band pattern that cover higher times. The remaining stray events (background) are not correlated neutrons with the capacitive pickup signal or γ rays that have pulse heights inside the neutron energy window. In offline data analysis another cut in pulse height was applied, represented in Figure 5.3 as the region between the two horizontal red lines. Forward analysis included the projection on the TOF axe to obtain the TOF histogram and an analysis of the gamma flash peak.

The obtained TOF histogram is shown in Figure 5.4. The neutrons are well discriminated from the prompt γ peak, ensured by the 72 cm detector flight path. At the same time, a low and constant background was detected and estimated as the average value in the TOF histogram, in the region between the γ flash and the fastest neutrons. The estimated level of background was almost equal to the level of background at long TOF and at very low TOF (prior to the γ flash peak). In the figure, the γ flash histogram is also zoomed in. The γ flash represents the time of the proton pulses and gives the measurement of the proton pulse width (time resolution of the beam). In the same distribution it is also reflected the 2 ns time resolution of the measurement instrument (DT5730SB). The FWHM of the Gaussian fit for the γ flash distribution give a value of 3.43 ± 0.05 ns ($\sigma = 1.46 \pm 0.02$ ns). Because of this, 4 ns was taken as the time resolution value for this measurement.

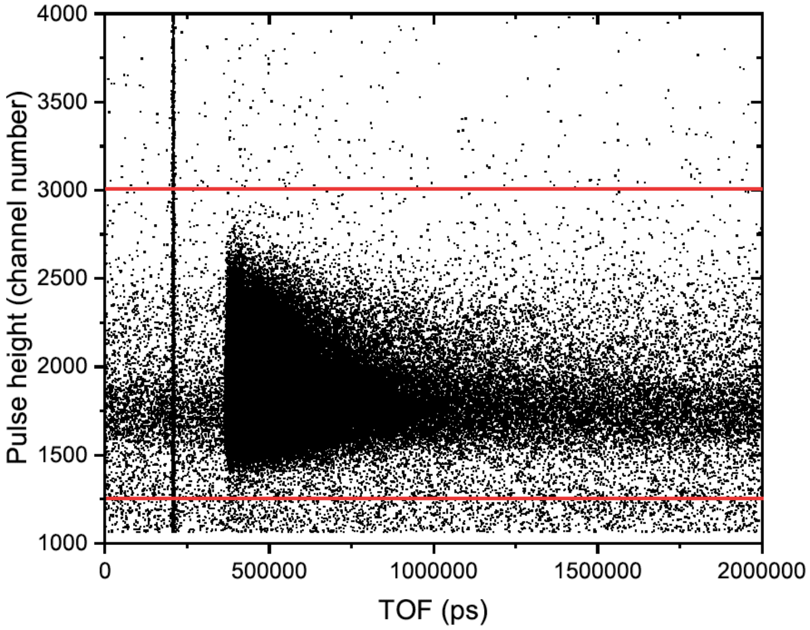

Figure 5.3: Two dimensional plot that shows the detector Pulse height *vs* Time-of-flight (TOF), with a proton energy of 1911.89 ± 0.73 keV.

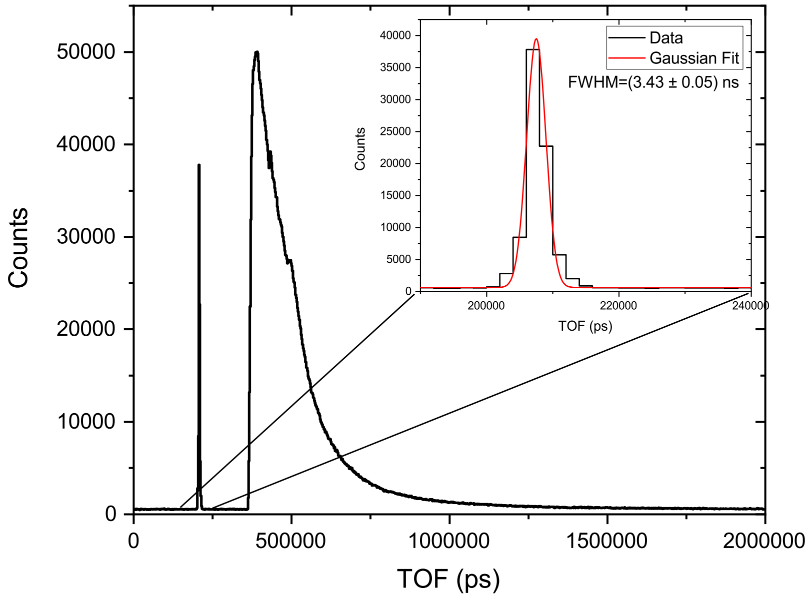

Figure 5.4: Time-of-flight histogram at zero degrees, measured with one inch thickness Li-glass detector at 72 cm from the target, obtained with E_p=1911.89 ± 0.73 keV.

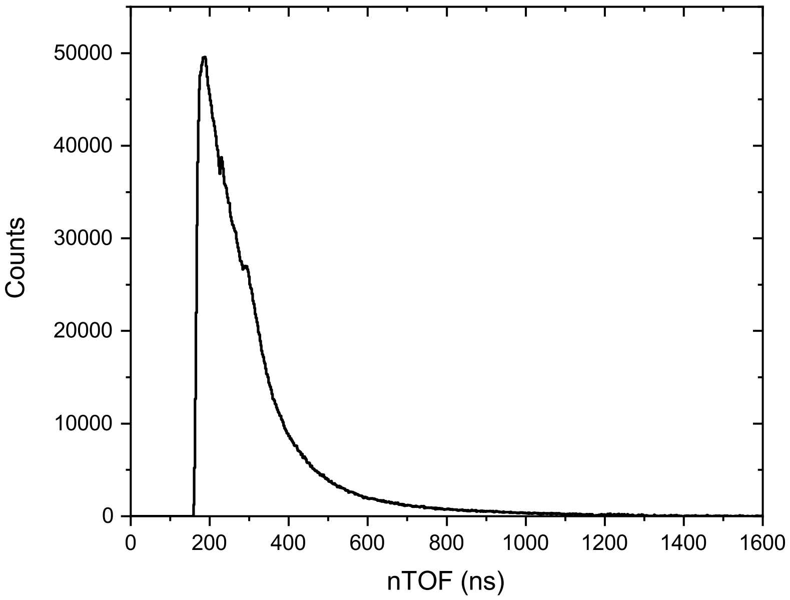

Figure 5.5: Neutron time-of-flight (nTOF) spectrum at zero degrees, acquired with a ^{6}Li-glass detector at 72 cm from the target with E_p=1911.89 $\pm$ 0.73 keV.

Figure 5.5 shows the final neutron TOF spectrum at zero degrees over a flight path of 72 cm. Each temporal bin in this shown spectrum was calculated as:

$$(n\mathrm{TOF})_i = (\mathrm{TOF})_i - (\mathrm{TOF})_\gamma + \mathrm{T}_\gamma \tag{5.1}$$

where $(\mathrm{TOF})_i$ is the TOF count in each temporal bin, $(\mathrm{TOF})_\gamma$ is the TOF where the γ flash peak appears (the mean energy in the distribution, Figure 5.4), and T_γ is the travelling time of γ rays over the 72 cm flight path (from the neutron production Li target to the Li-glass detector). The calculated background value was subtracted from the nTOF spectrum, obtaining the one shown in Figure 5.5. This spectrum is the one used in the conversion method from TOF to an energy spectrum.

Applying the method described in Chapter 3, employing the response matrix of the Li-glass detector, the neutron energy spectrum at zero degrees was obtained. The time bins were chosen to have almost the same counting statistic per bin. With the acquired statistics, it was possible to obtain the neutron energy spectrum with 40 energy bins, from 1 keV to 120 keV. The obtained neutron energy spectrum is shown in Figure 5.6. The most probable neutron energy is 30 keV and the maximum energy around 110 keV, as expected from the ^{7}Li(p,n)^{7}Be reaction kinematics. The higher part of the energy spectrum was obtained using 4 ns temporal bins, because

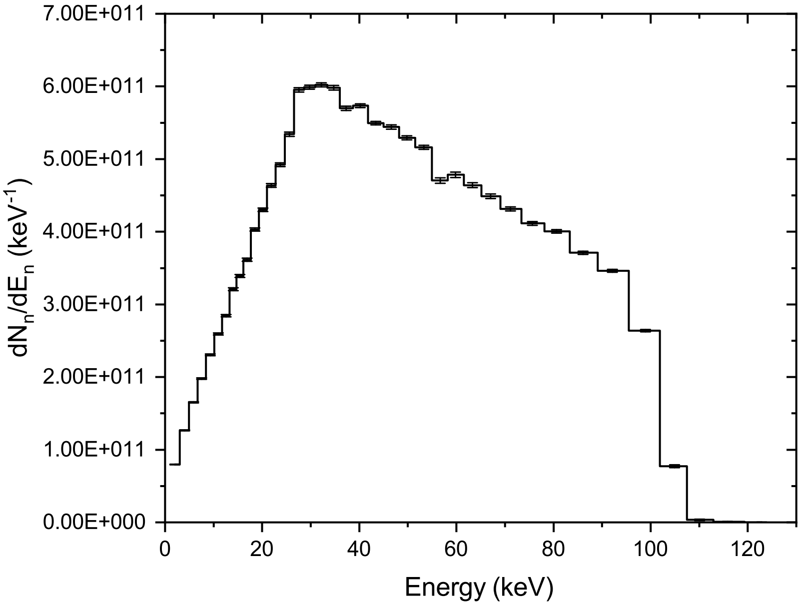

Figure 5.6: Experimental neutron time-of-flight spectrum at zero degrees obtained with proton energies of 1911.89 ± 0.73 keV.

of the already mentioned time resolution of the measurement. At lower energies the spectrum was obtained with energy bins of 2 keV. Less than 1% relative uncertainty were obtained.

Following the same procedure described in Chapter 3, a simulation of the neutron time-of-flight spectrum was performed, employing the Monte Carlo MCNPX [61] code. The obtained neutron energy spectrum (Figure 5.6) was employed as neutron source and was placed at 72 cm from the detector outer face. Thus, the experimental conditions of this measurement are reproduced. The comparison between the experimental neutron TOF spectrum with the one simulated employing the measured neutron energy spectrum (Figure 5.6) is shown in Figure 5.7. As observed in the figure, there is a good agreement between both spectra, having a relative error of less than 1% up to 400 ns, and less than 10% up to 600 ns. This comparison was performed as a crosscheck of the conversion method. It is important to remark that the conversion method proposed in this work reproduce the experimental data measured in the experiment, demonstrating the accuracy of the obtained neutron energy spectrum.

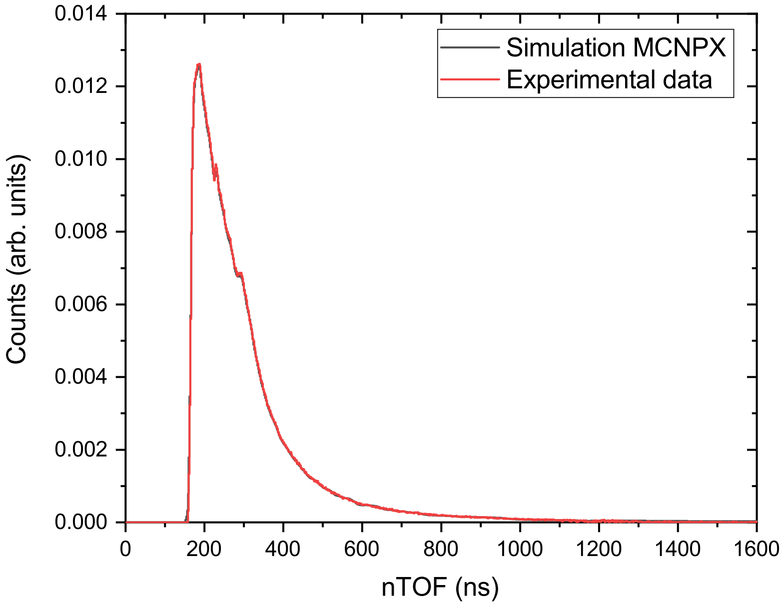

Figure 5.7: Experimental neutron spectrum at zero degrees compared to the simulated one, employing the measured neutron energy spectrum as neutron source.

5.3 Comparison with experimental data from the literature

The obtained experimental neutron energy spectrum at zero degrees reported in Section 5.2 was compared with the ones reported in the works of Lederer *et al.* [45] and Feinberg *et al.* [46]. The experimental data from these works were taken from the Experimental Nuclear Reaction Data (EXFOR) [53].

The work of Lederer *et al.* was performed in the 3.75 MV Van de Graaff accelerator of the Physikalisch-Technische Bundesanstalt (PTB) Institute [74]. A proton pulsed beam with a repetition rate of 625 kHz was employed. With a nominal energy of 1912 ± 1.2 keV and an average current of $0.5 - 0.8$ μA, their measurements were performed. A metallic lithium target was employed, and the nTOF measured with a 2.85 mm thickness ^{6}Li-glass detector. Based on a comparison with a code which generates neutron spectra, the authors reported that the proton energy of the accelerator was around 1910 keV rather than the nominal 1912 keV.

The work of Feinberg *et al.* was performed in the 7 MV Van de Graaff accelerator of the Institute of Reference Materials and Measurements (IRMM). In their experiment, a lithium fluoride (LiF) target was employed, and the neutrons were detected by a one inch thickness ^{6}Li-glass detector. A proton pulsed beam with 625 kHz frequency and a nominal energy of 1912 ± 1.5 keV was employed in their measurement.

Another nTOF measurement using the same reaction and the same proton energy is reported in the work of Macías *et al.* [47]. This measurement was carried out at the CNA facility in Seville, Spain. The results were obtained for different repetition rates and two different neutron flight path. A good agreement with the work of Lederer *et al.* was found, when both works results were compared.

A comparison of the experimental neutron energy spectrum at zero degrees from the present work and the ones obtained in the works of Lederer *et al.* and Feinberg *et al.* is shown in Figure 5.8. The neutron spectra from these works were re-binned to the same energy bins calculated for the present work.

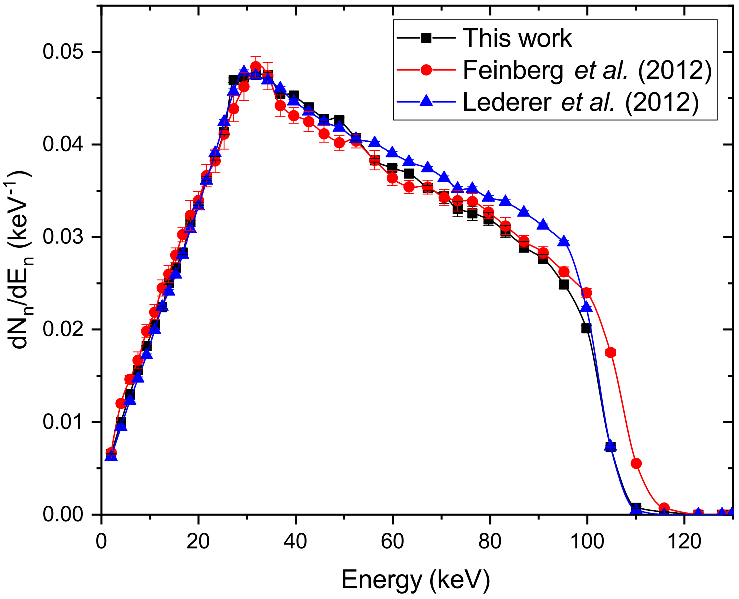

Figure 5.8: Experimental neutron spectrum obtained in the present work compared to the one obtained by Lederer *et al.* [45] and Feinberg *et al.* [46].

There is a good agreement between the shown spectra, except for the high energy region (between 50 keV and 100 keV). In general, the spectrum obtained in the present work agrees with the spectrum from Lederer *et al.*, except in the region between 60 and 100 keV. In this energy region, the spectrum obtained in this work agrees with the one obtained by Feinberg *et al.*. The difference between these spectra could be explained either (1) by the difference in the nominal proton energy (distribution mean energy and FWHM) between these measurements or (2) by a possible degradation in the Li target, as reported in the work of Lederer *et al.*. In any case, this comparison confirms the good performance of the conversion method from TOFs to energy spectrum proposed in this work.

Chapter 6

Maxwell-Boltzmann neutron spectrum measurement

In order to probe the possibility of producing a well defined Maxwell-Boltzmann neutron spectrum (MBNS), neutron time-of-flight (nTOF) technique was employed to measure the integrated neutron spectrum (from 0 to 90 degrees) from the ^{7}Li(p,n)^{7}Be reaction, using the proton energy shaper (see Chapter 2). In this measurement, the proton beam energy was set to 3170 keV, using the time-of-flight spectrometry of the proton pulsed beam (pTOF). As proton energy shaper, an aluminum (Al) foil with 50 μm thickness was placed just before the lithium target. The material and thickness of the proton energy shaper, as well as the value of the initial proton energy are the result of a study described in the Chapter 2. With this proton energy and the Al foil, a MBNS with a thermal temperature of 30 keV is expected to be obtained. With a 600 kHz proton pulsed beam and approximately 4 ns time width, the nTOF was then implemented to determine the neutron spectrum. During the measurement, an average current on target of 100 nA was measured.

The experimental setup for the MBNS measurement is shown in Figure 6.1. A specifically designed low mass goniometer, with movable stands for placing the detectors, made by carbon fiber and aluminum, was carefully aligned and positioned. A first alignment with the beamline was made with the light coming from a laser located in the opposite end side of the beam pipe. After placing the target, a second alignment was made locating the target at the center of a goniometer.

Four Li-glass detectors were simultaneously employed to measured different angles and to increase the statistic. The detectors were located at 49.97 ± 0.01 cm and at the same height from the center of the lithium target. This flight path and the selected repetition rate allowed to measure neutron energy down to 1 keV and ensured the presence of not overlapped neutrons coming from different proton bunches. As neutron monitor, the 3 mm thickness Li-glass detector was always kept at zero degrees. This monitor was used for spectrum normalization to a common denominator, the neutron production during each measurement. Besides, the monitor detector allowed to check the beam and target stability during the measurement. The other three detectors, described in Section 4.4, were moved around from 10 to 90 degrees in steps of 10 degrees. For data acquisition, the DT5730SB digitizer was used and controlled by the CoMPASS software [71]. The results for this measurement are reported in the following sections.

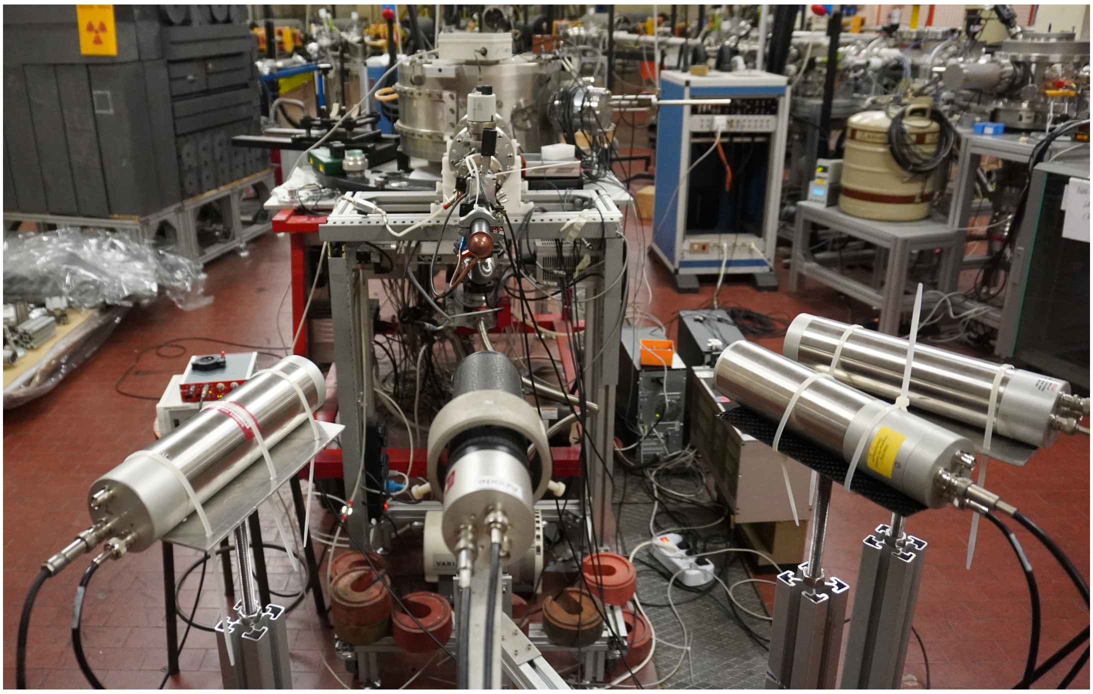

Figure 6.1: Experimental setup for the Maxwell-Boltzmann neutron spectrum (MBNS) measurement with a proton energy of 3170 keV. Detectors were located at 50 cm from the target at different angles to measure the neutron time-of-flight.

6.1 Proton time-of-flight spectrometry

A mean proton energy of 3170 keV was set with proton time-of-flight spectrometry (pTOF) (See Section 4.6). Using the Equation 4.2, the proton energy distribution was determined, employing as parameters the calculated flight path (see Section 4.7), the time-of-flight (TOF) distribution of protons, the speed of light and the proton mass at rest. To measure the TOF distribution, the signals from the capacitive pickups 1 and 2 were used as input to the desktop digitizer DT5751. The resulting proton energy distribution measured with pTOF is shown in Figure 6.2. Two plots

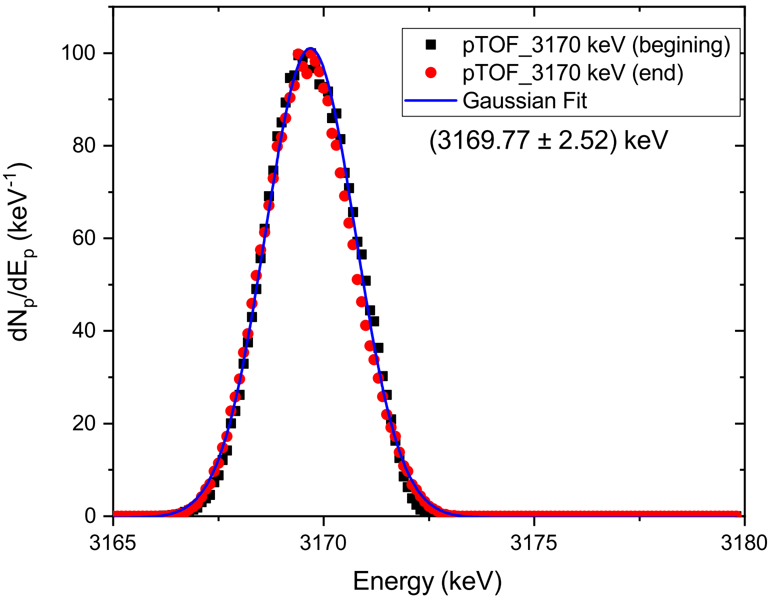

Figure 6.2: Proton energy distribution with a mean energy of 3169.77 keV and a FWHM of 2.52 keV, determined with proton time-of-flight (pTOF) spectrometry.

are included in the figure. The first one refers to the beginning of the measurement, before measuring the neutron time-of-flight (nTOF) spectrum. The second one was acquired at the end of the nTOF measurement. In this way the stability of the accelerator was crosschecked. The figure shows how stable the proton beam was, always giving the same proton distribution. The stability of the accelerator was also crosscheck with the γ flash time width distribution in the TOF spectrum (see Figures 6.4 and 6.5). This ensures that the emitted neutron spectrum is a product of the same proton beam. As result of the Gaussian fit for the distributions, a mean proton energy of 3169.77 keV with full with half maximum (FWHM) of 2.52 keV was obtained.

6.2 Neutron spectrum analysis

In the nTOF spectrum measurement, the goniometer allowed to move the three Li-glass detectors around to measure different angles, from 10° to 90°, in steps of 10°. The fourth Li-glass detector, used as neutron monitor, was always kept at zero degrees. A coincidence window of 1.66 μs (1/600kHz) was set in the CoMPASS software. The coincidence of signals of each detector with the signal of the capacitive pickup 2 was acquired and saved for post-processing data analysis. With the acquired time-of-flight (TOF) spectra measured for each angle, the same procedure explained in Section 5.2 was performed. First, each detector was set in the CoMPASS input windows. An energy cut around the neutron peak in each detector pulse height spectrum was applied, eliminating most of the stray gamma events, and thus reducing the count rate in the digitizer.

In the offline data analysis, another event selection in pulse height was applied reducing even more the stray gamma events and the uncorrelated background. The level for the neutron background was estimated at each angular detector position by determining the average background in the region between the γ flash peak and the fastest neutrons. Figure 6.3 shows the TOF histogram for the one inch detector at 30°. In the figure, a zoom at low TOF values is also plotted, in the region where the neutron background was calculated. The background level for each angle was always flat and, within the statistics, it had the same value (when normalized to monitor). This fact indicates that the background at each angle is not correlated with TOF and that a constant value can be subtracted from the neutron TOF spectrum. The value of background was subtracted in the neutron TOF spectrum for each angle detector position.

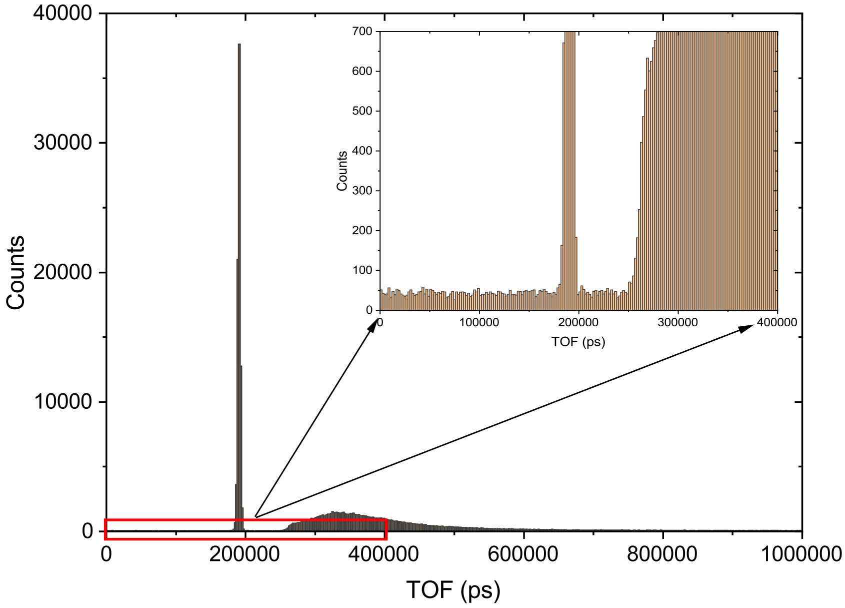

Figure 6.3: Time-of-flight histogram for the one inch detector, placed at 50 cm from the lithium target, measured at 30°.

The TOF histogram for the one inch detector, measured at three different angles, is shown in Figure 6.4. The TOF histogram for the monitor detector, measured at three different times is shown in Figure 6.5. The discrimination between the peaks corresponding to gamma rays and neutrons can be appreciated in both figures. The gamma flash peak gives direct information about the temporal distribution of the protons beam. The figures also show how the γ flash time width distribution was always the same, and therefore, the temporal distribution of the proton beam. The good stability of the accelerator is confirmed with these two plots. The FWHM of the γ flash peak distribution was around 4 ns for each detector. This value was taken as the temporal resolution value for the measurement.

6.3 Solid angle corrections

For the integrated neutron spectrum, a solid angle correction must be included in the calculation of each angle spectrum. This correction depends on the flight path between the detector and the target and the angle (α) where the detector is placed. The flight path was the same for each angle detector position. The neutron spectrum was measured in steps of 10°. Since the detector does not cover an angle of 10°, a

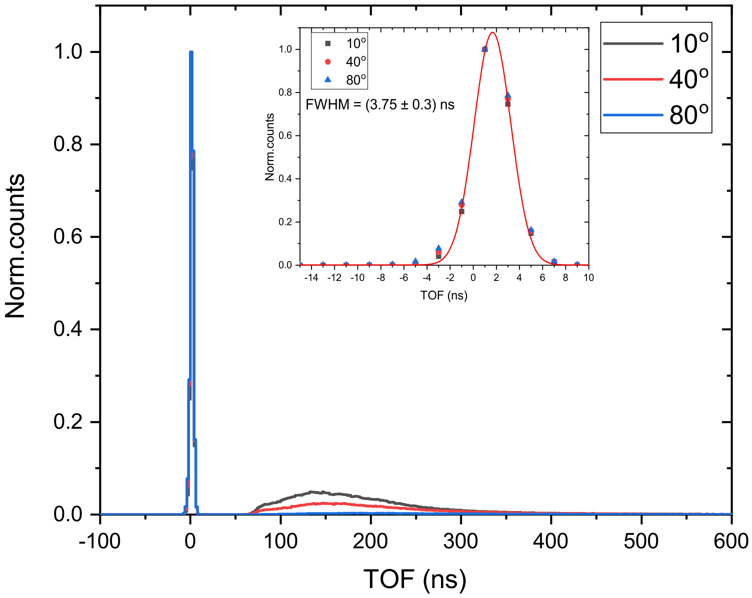

Figure 6.4: Time-of-flight histogram for the one inch detector, placed at 50 cm from the lithium target, measured at three different angles.

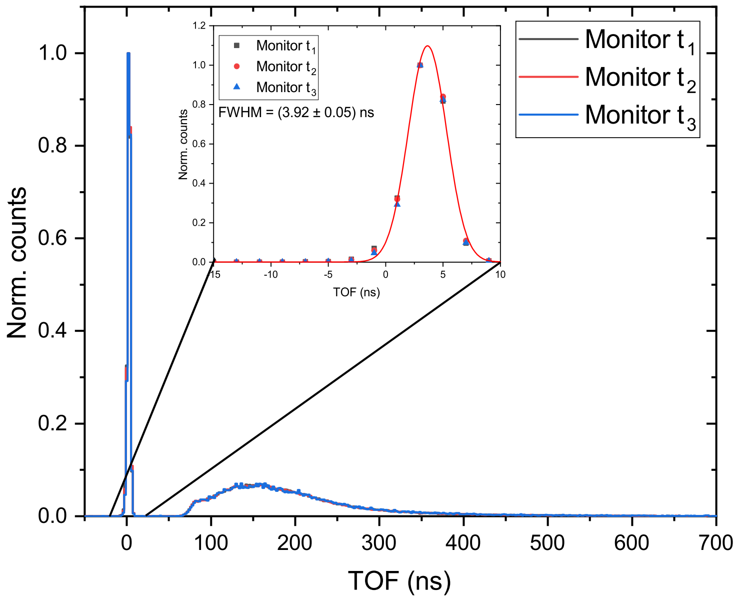

Figure 6.5: Time-of-flight histogram for the monitor detector, placed at zero degrees respect to the beam direction and at 50 cm from the lithium target, measured at three different times (the first (t_1), the last (t_2), and an intermediate (t_3) runs during the measurement).

first correction was made, employing the equation of the solid angle of a cone with 2θ angle aperture, $\Omega = 2\pi(1 - \cos\alpha)$. This factor is the same for each detector position and was calculated as:

$$f_1 = \frac{\Omega_1}{\Omega_3} = \frac{2\pi(1 - \cos 5^\circ)}{2\pi(1 - \cos\theta)} \tag{6.1}$$

where 2θ is the angle cover by the detector ($\theta \approx 3^\circ$). By multiplying each TOF spectrum with this factor the detector covers an angle of 10°.

A second factor proportional to the revolution area of the scaled detector around the axis from the center of the target to the center of the detector at zero degrees was calculated as:

$$\begin{aligned} f_2 = \frac{\Omega_2}{\Omega_1} &= \frac{2\pi[1 - \cos(\alpha + 5^\circ)] - 2\pi[1 - \cos(\alpha - 5^\circ)]}{2\pi(1 - \cos 5^\circ)} \\ &= \frac{\cos(\alpha - 5^\circ) - \cos(\alpha + 5^\circ)}{1 - \cos 5^\circ} \end{aligned} \tag{6.2}$$

where Ω_1 the solid angle subtend by the scaled detector, and Ω_2 is the difference of solid angles between two cones with angles $\alpha + 5^\circ$ and $\alpha - 5^\circ$, as shown in Figure 6.6. The corresponding factor for each detector position f_α is equals to the multiplication

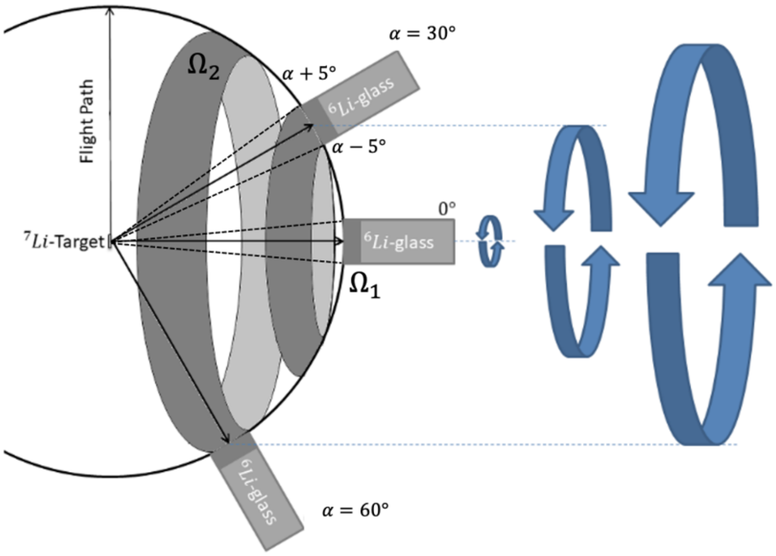

Figure 6.6: Bird's-eye view of the schematic experimental setup (non scaled figure)[75].

of f_1 and f_2.

Another method to calculate the corresponding factor, considering the solid angle of the individual angular positions, was reported in the work of Lederer *et al.* [45]. The factors were calculated using the following equation:

$$f_\alpha = (\cos(\alpha - 5^\circ))/(1 - \cos(60^\circ + 5^\circ)) \tag{6.3}$$

Both methods for the calculation of the correction factor gave the same results after normalization to the maximum value. Table 6.1 shows the values obtained for the correction factor.

Table 6.1: Solid angle correction factors. Values were normalized to the maxima. Each measured nTOF spectrum was multiplied by the corresponding factor.

Angle	10°	20°	30°	40°	50°	60°	70°	80°	90°
f_α	0.198	0.347	0.508	0.653	0.778	0.879	0.954	1.000	0.508

6.4 Neutron time-of-flight and angular spectra

Different glass thickness in the detectors implyes different moderation times, and therefore different time-of-flights (TOF), even in case of monoenergetic neutron beams. Because of this, two separated analysis were done, one for the half inch thickness detector and the other for the one inch thickness detectors. Since both one inch detectors are equals, a final spectrum as the sum of the neutron spectrum counts was obtained. In this way, more statistics were added to the measurement. The final neutron TOF spectrum for each angle detector position (from 10 to 90 degrees) over a 50 cm flight path, measured with a proton energy of 3170 keV and a 50 μm aluminum foil as proton beam shaper, is shown in Figure 6.7. Results are presented for the (a) half inch and (b) one inch lithium glass detectors, respectively. Each spectra was corrected by the solid angle factor (Section 6.3) and normalized to the neutron monitor counts (3 mm Li-glass detector).

The use of two different detectors implied the calculation of two response matrices and a different TOF-energy bins relationship, for the conversion method proposed in Chapter 2. Applying the method, each measured spectrum from Figure 6.7 was converted to an energy spectrum, employing the respective response function for the Li-glass detector. The time bins were chosen to have almost the same counting statistic per bin (about 1% relative errors). With the half inch thick detector acquired statistics, it was possible to obtain the neutron energy spectrum with 24 energy bins, from 1 keV to 470 keV. Moreover, with the one inch thick detector were obtained 37 energy bins from 1 keV to 470 keV. Figure 6.8 shows the angular neutron energy spectra obtained with (a) half inch, (b) one inch thickness Li-glass detectors after the conversion method employing the measured nTOF spectrum (Figure 6.7). The relative errors on each spectrum were less than 1%, except for the high energy part where the counting statistics is low.

6.5 Angle-integrated energy spectra

Figure 6.9 shows the 0°-90° angle-integrated neutron time-of-flight (TOF) spectrum obtained from the experiment with the one inch and half inch thickness Li-glass detectors. The difference between these two spectra is due to the different involved TOF and the detectors efficiency. These spectra were obtained by summing the weighted TOF spectra (Figure 6.7), from 10 up to 90 degrees for each detector. Each spectrum was then converted using the already mentioned response matrix for each detector and the relationship between TOF and energy bins. The resulted angle-integrated neutron energy spectrum for the measurement is shown in Figure 6.10. The relative errors on each spectrum are less than 1%. From the figure, it is possible to observe the good agreement between these spectra. This measurement was performed with two different detectors, and it is important to highlight that the

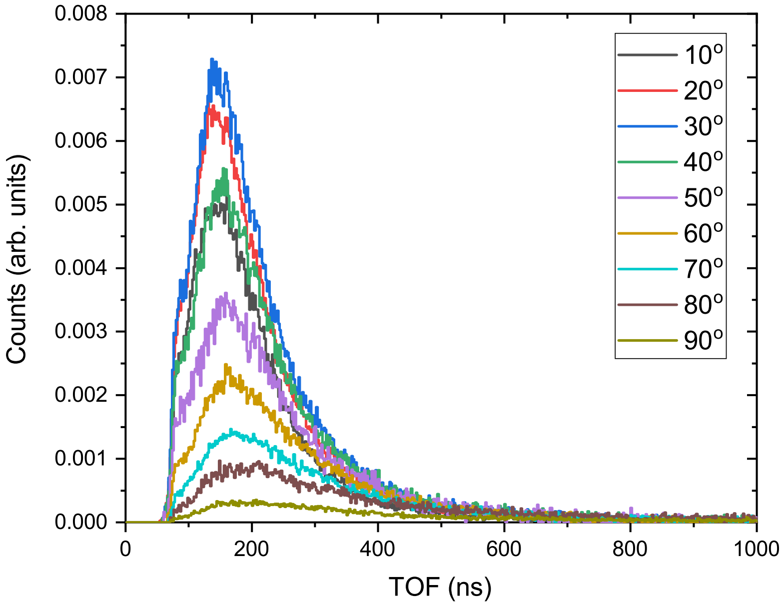

(a)

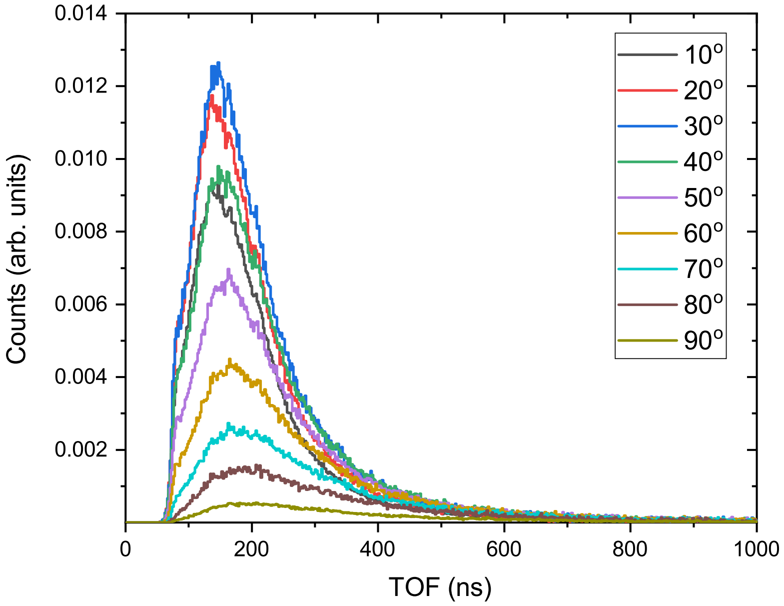

(b)

Figure 6.7: Angular neutron time-of-flight (TOF) spectra acquired with (a) half inch, (b) one inch thickness ^{6}Li-glass detectors over a flight path of 50 cm, from 10 to 90 degrees in steps of 10 degrees, with a proton energy of 3170 keV and the aluminum foil of 50 μm as proton beam shaper. Spectra are already normalized to the monitor counts and corrected for the solid angle factor.

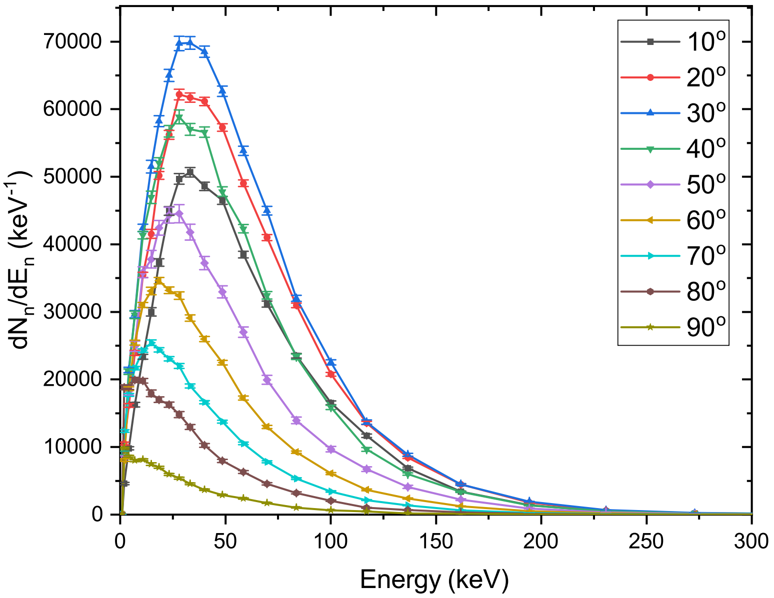

(a)

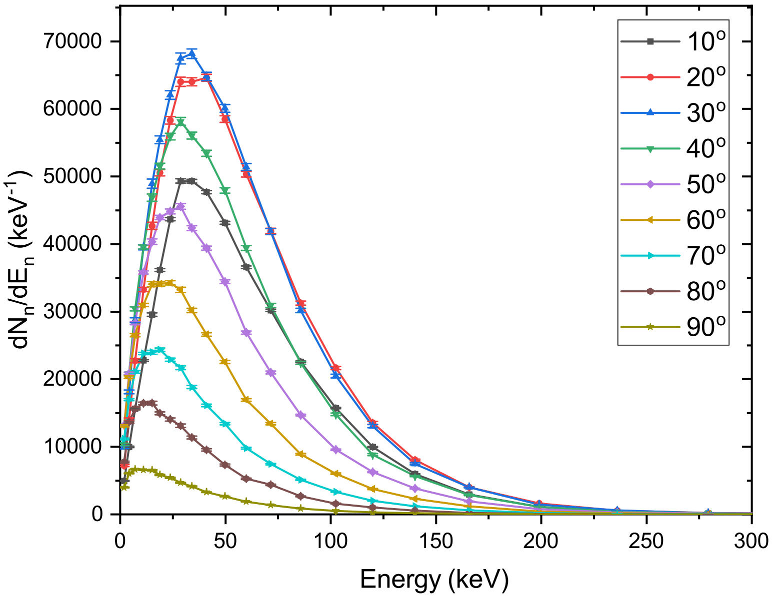

(b)

Figure 6.8: Angular neutron energy spectra with (a) half inch, (b) one inch thickness Li-glass detector, from 10 to 90 degrees in steps of 10 degrees, measured with a proton energy of 3170 keV and the aluminum foil of 50 μm as proton beam shaper. Spectra are already normalized to the monitor counts and corrected for the solid angle factor.

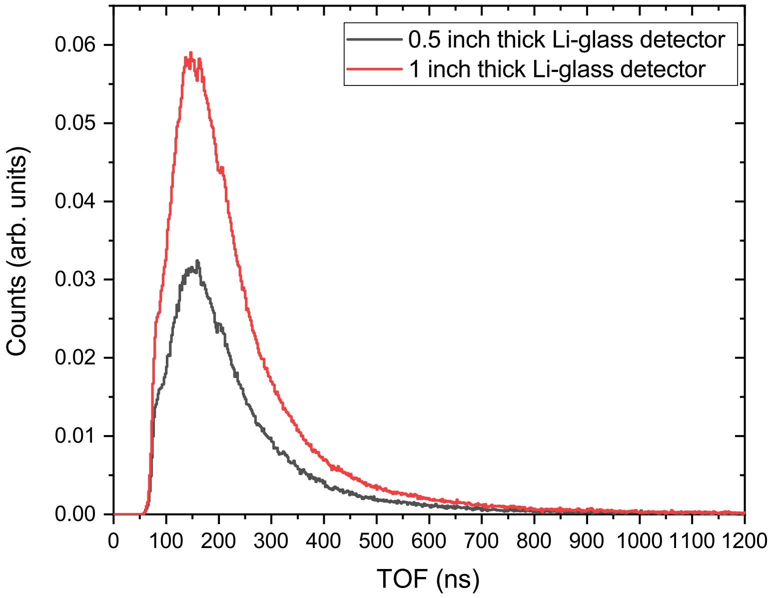

Figure 6.9: Angle-integrated neutron time-of-flight (TOF) spectrum, obtained by summing the weighted TOF spectra from 10 up to 90 degrees for each detector, presented in Figure 6.7.

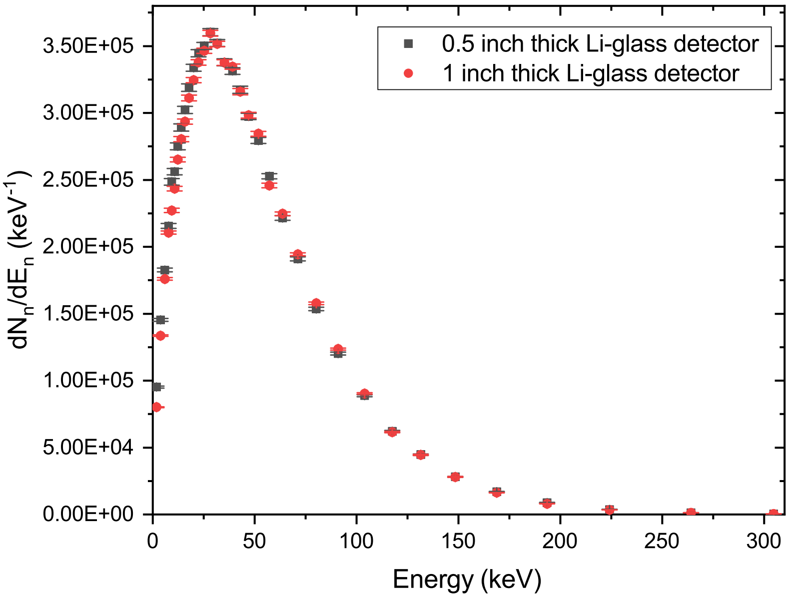

Figure 6.10: 0°-90° Angle-integrated neutron energy spectrum, obtained with the conversion method proposed in this work, for proton energies of 3170 keV and the aluminum foil of 50 μm as proton beam shaper.

same emitted neutron spectrum was measured (as should be). This fact validates, once again, the conversion method from TOF spectrum to energy spectrum proposed in this work, since different flight paths and detection efficiencies were involved in the process.

The final neutron energy spectrum obtained for the Maxwell-Boltzmann neutron spectrum (MBNS) measurement is shown in Figure 6.11. The final spectrum was calculated as the average between the values for each energy bin in Figure 6.10. The least squares fit to a Maxwell-Boltzmann distribution is also represented in the figure. The equation of this distribution is:

$$f(\mathrm{E}) = \frac{d\mathrm{N}}{d\mathrm{E}} = a \cdot \mathrm{E} \cdot \exp\left(\frac{-\mathrm{E}}{\mathrm{kT}}\right) \tag{6.4}$$

where a is a parameter that reflects the maximum value of the $f(\mathrm{E})$ distribution, and kT is the thermal temperature of the distribution (second parameter). The result of the fitting parameters are $a = (3.46 \pm 0.08) \times 10^4$ n/keV and $\mathrm{kT} = 28.35 \pm 0.29$ keV. In the figure, it is observed the good agreement between the experimental data and the Maxwell-Boltzmann fit, even in the high energy part of the spectrum where the Ratynski and Käppeler [43] work fails to reproduce.

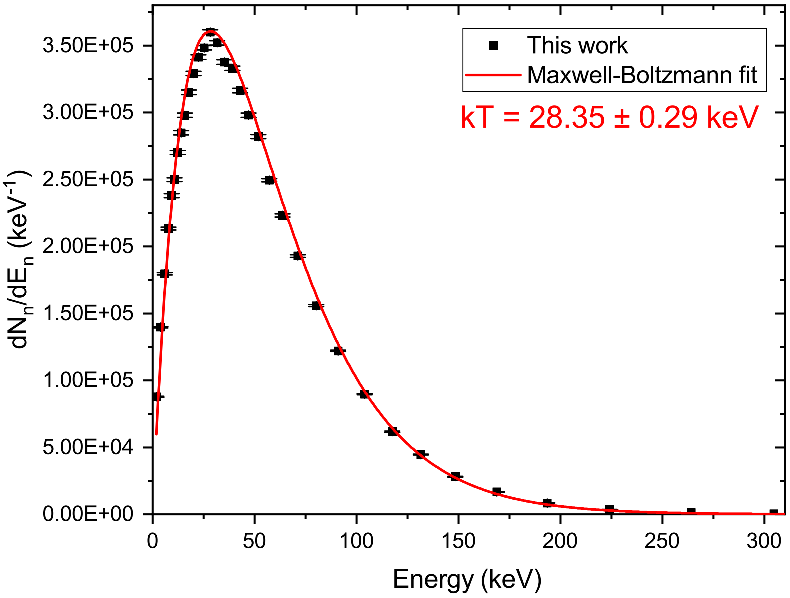

Figure 6.11: Final angle-integrated, from 0° to 90°, neutron energy spectrum and the least squares fit to a Maxwell-Boltzmann distribution.

With an initial proton energy of 3169.77 ± 2.52 keV and the aluminum foil of 50 μm thickness, the obtained MBNS has not the expected 30 keV thermal temperature. Since the accelerator was calibrated, the parameter that can change this result is the thickness of the aluminum foil. A study of the thickness of the aluminum foil was performed with a Scanning Electron Microscope (SEM). A small rectangular portion, of the original aluminum foil supplied by the Goodfellow Company [76], was cut with an electro-erosion machine for further thickness analysis. In this way, two edges of the aluminum rectangle foil portion were maintained morpho-structurally as provided by the supplier and the other two edges according to what happened after cutting with the electro-erosion machine. Results of SEM analysis of both type edges are shown in Figure 6.12 and in Table 6.2.

This measurement shows the uncertainty in the thickness estimation of the Al foil. The nominal thickness value reported by the Goodfellow company is 50 μm ± 15%, meaning 50.0 ± 7.5 μm. Both measurements performed with the SEM analysis are within the uncertainty reported from the Goodfellow company. To have a crosscheck estimation of the real thickness value the following calculations were performed. With the Stopping power and Range of Ions in Matter (SRIM 2013) software [60] the distributions of protons after passing different thickness of the aluminum foil

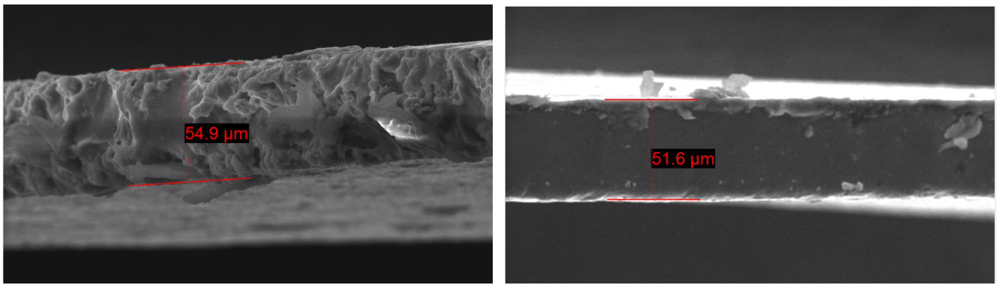

(a) (b)

Figure 6.12: Image of the thickness of the aluminum foil, taken on a scanning electron microscope (SEM), (a) edge of the aluminum rectangle foil portion after electro-erosion processing, (b) edge of the original aluminum rectangle foil portion as supplied by Goodfellow company.

Table 6.2: Thickness of the aluminum foil measured with a scanning electron microscope (SEM).

Edge from	Thickness [μm]			Avg ± STDV [μm]
Electro-erosion	54.9	54.9	55.9	55.2 ± 0.57
Goodfellow company	51.6	51.4	50.6	51.2 ± 0.58

(50-55 μm) were calculated. An initial proton energy of 3169.77 keV was considered. With the mean value and the FWHM of each Gaussian distribution, the theoretical neutron spectrum was calculated with the computer code developed to solve the differential neutron yield of the ^{7}Li(p,n)^{7}Be reaction (reported in Chapter 2). Each generated spectrum was then compared with the experimental one, and the R^2 coefficient determined (see Chapter 2). As result, with the best fit (highest R^2 value) the aluminum foil thickness was found to be 51 μm. The difference between the expected 30 keV stellar temperature value and the obtained kT = 28.35 ± 0.29 keV can be explained by a wrong estimation in the thickness of the aluminum foil.

To obtain the Maxwell average cross section (MACS) from an activation measurement, the neutron spectrum should correspond to the thermal spectrum in the stars. In the present work a neutron spectrum that follows a Maxwell-Boltzmann distribution with a thermal temperature of 28.35 ± 0.29 keV was measured. When a sample is irradiated with this neutron field no corrections (or a small ones) are necessary to be included to obtain the MACS from experimental measurements. Setting the same proton energy and employing the same aluminum foil, the MACS measurements for different isotopes will be calculated in a future experiment, knowing that the neutron spectrum will correspond to the stellar one with a kT of 28 keV.

Conclusions

In the experimental measurement, the neutron time-of-flight spectrometry (nTOF) was implemented to determine the neutron spectrum. As source of neutrons the ^{7}Li(p,n)^{7}Be nuclear reaction was employed, using a lithium metallic target and a 600 kHz proton pulsed beam from the Van de Graaff accelerator of the Legnaro National Laboratory of the National Institute of Physics Nuclear (LNL-INFN), in Padua, Italy.

To obtain a Maxwell-Boltzmann neutron spectrum (MBNS) with a desired kT, the method of using a proton energy shaper was employed. The proton energy shaper consisted in a foil of some material, where the proton beam passed through and, its energy distribution was shaped prior to impinge on the lithium target. A study of different materials and thickness of the proton energy shaper was performed. A Gaussian-like energy distribution (characterized by mean energy and the Full Width Half Maximum (FWHM)) was obtained after protons passed the aluminum foil. As a result, an aluminum foil was chosen as proton energy shaper. To determine the initial proton energy and the aluminum foil thickness, starting from the kinematics of the ^{7}Li(p,n)^{7}Be, a computer code that calculates the differential neutron yields was developed. A second code was developed to find the combination of mean proton energy and FWHM that fits best the neutron spectrum to a MBNS with a desired kT. To produce a MBNS with 30 keV of thermal temperature, an initial proton energy of 3170 keV and an aluminum foil of 50 μm thickness were obtained. With these configurations the MBNS measurement was performed.

A new approach to transform the measured time-of-flight (TOF) spectra into energy spectra was also implemented, to avoid the errors that direct conversion entails. The proposed conversion method uses the detector response matrix to account the time distribution of neutrons inside the detector, allowing to reproduce the emitted neutron energy spectrum from the TOF spectrum, with a unique solution. The method works in two steps. First, energy bins from temporal bins are calculated. Then, the time spectra correspondent to the chosen energy bins are obtained with MCNPX, implementing precisely the geometry of the setup. The temporal distribution inside the chosen bins becomes the rows of the response matrix. By inverting the response matrix, the energy spectrum is calculated.

In the experimental measurement, the energy of the proton pulsed beam coming from the accelerator was precisely determined with proton time-of-flight spectrometry (pTOF). To determine the flight path of protons between two capacitive pickups, the calibration of the accelerator was performed scanning the ^{7}Li(p,n)^{7}Be reaction, by measuring the neutrons emission for proton energies near the reaction energy threshold.

After the accelerator calibration, the neutron spectrum at zero degrees with 1912 keV energy protons was measured. In this measurement a Li-glass detector located at 72 cm from the Li target, at zero degrees with respect to the beam direction, was employed to measure the nTOF spectrum. The measured nTOF spectrum was transformed to an energy spectrum employing the proposed conversion method with the detector response matrix. This measurement was performed to experimentally validate the novel conversion method, comparing the resulted neutron energy spectrum with other experimental data found in the literature. A relatively good agreement was found when said comparison was done. Moreover, using the obtained energy spectrum the corresponding time spectrum was calculated with the MCNPX and compared with the measured TOF. A good agreement was found, supporting the robustness of the conversion method.

The Maxwell-Boltzmann neutron spectrum measurement with a proton energy of 3170 keV and the 50 μm thickness Al foil was performed. The neutron TOF spectrum was measured, from 0 to 90 degrees in steps of 10°. Two one inch thickness and one half inch thickness Li-glass detectors were employed. All detectors where precisely placed at 50 cm from the Li target and were moved around to measure different angles. For spectrum normalization, a fourth 3 mm thickness Li-glass was employed and always kept at zero degrees. Besides, this neutron monitor allowed to check the beam and target stability during the overall measurement. For each detector angle the measured TOF was converted to an energy spectrum and corrected by a solid angle correction factor and to the monitor counts. In this way, the angular energy spectra for each detector type (half inch and one inch thickness) were obtained. An integrated neutron energy spectrum was obtained by summing the weighted TOF spectra, for all angles from 0 to 90 degrees. After the conversion method was applied, a 0°-90° angle-integrated spectrum was obtained for each detector type. All neutron spectra were obtained with less than 1% relative errors. As should be, the neutron energy spectrum detected with two different detectors were the same within the statistic uncertainties. A final neutron integrated energy spectrum was determined with the average spectrum value from both detectors for each energy bin. A least squares fit of the final measured integrated neutron spectrum to a Maxwell-Boltzmann distribution yielded a stellar temperature value of kT= 28.35 ± 0.29 keV, with a factor $R^2 = 0.99$. The kT value obtained from this fitting disagree with the 30 keV expected one. The difference in the thermal temperature values were associated to a wrong estimation of the Al foil thickness. Instead of the nominal 50 μm provided by the selling company, a value of 51 μm was estimated and checked with a Scanning Electron Microscope (SEM) analysis.

In conclusion, in this work a novel method to convert from TOF spectrum to energy spectrum was proposed and validated. Its application to any temporal TOF spectrum allows to reproduce in a very accurate form the emitted neutron energy spectrum. The most important achievement from this work is that a well reproduced Maxwell-Boltzmann neutron spectrum with a thermal temperature of 28.35 ± 0.29 keV was measured. Irradiating a sample with this neutron field, a very accurate measurement of the MACS at kT=28 keV can be performed. In a future experiment, setting the same proton energy (3170 MeV) and using the same aluminum foil the neutron activation method will be employed to this purpose.

Acknowledgements

There are many people who helped me along the way on this journey. I want to take a moment to thank them.

First, I would like to thank my supervisor, Dr. Pierfrancesco Mastinu, for all the support and encouragement he gave me, during this three years. Without his guidance and constant feedback this PhD would not have been achievable. I want to thank him for his support and for all the opportunities I was given to further my research.

I would like to acknowledge my colleagues from the INFN-LNL for their wonderful collaboration, in particular to my office colleagues and friends: Lisa, Alberto and Massimo. Also to the accelerator technicians at the CN: Luca, Alberto and Daniele for their support in the experiments.

I would also like to thank my former tutor, Guido Martín Hernández, for his valuable guidance throughout my studies.

I could not have completed this dissertation without the support of my friends, Annie, Arturo and Dariel, who provided stimulating discussions as well as happy distractions to rest my mind outside of my research.

Last but not least, I would like to thank my parents, my entire family and my love Rogelio for their wise counsel and sympathetic ear. You are always there for me!

Bibliography

[1] J. José and C. Iliadis. Nuclear astrophysics: the unfinished quest for the origin of the elements. *Reports on Progress in Physics*, 74(9):096901, Aug 2011. ISSN 1361-6633. doi: 10.1088/0034-4885/74/9/096901. URL `http://dx.doi.org/10.1088/0034-4885/74/9/096901`.

[2] Nuclear astrophysics. Technical report, French Alternative Energies and Atomic Energy Commission (CEA), 2015.

[3] R. A. Alpher, H. Bethe, and G. Gamow. The origin of chemical elements. *Phys. Rev.*, 73:803–804, Apr 1948. doi: 10.1103/PhysRev.73.803. URL `https://link.aps.org/doi/10.1103/PhysRev.73.803`.

[4] E. M. Burbidge, G. R. Burbidge, W. A. Fowler, and F. Hoyle. Synthesis of the elements in stars. *Rev. Mod. Phys.*, 29:547–650, Oct 1957. doi: 10.1103/RevModPhys.29.547. URL `https://link.aps.org/doi/10.1103/RevModPhys.29.547`.

[5] A. Lépine-Szily and P. Descouvemont. Nuclear astrophysics: Nucleosynthesis in the Universe. *International Journal of Astrobiology*, 11(4):243–250, 2012. ISSN 14735504. doi: 10.1017/S1473550412000158.

[6] Opportunities in Nuclear Astrophysics. Technical report, Joint Institute for Nuclear Astrophysics Michigan State University and the University of Notre Dame, 1999.

[7] The universe is made up of protons and neutrons - What is a table of nuclides? URL `https://www.nishina.riken.jp/research/nucleus_e.html`.

[8] S. Mellema. The Cosmic Universe, 2019.

[9] C. Iliadis. *Nuclear Physics of Stars*. 2015.

[10] H. E. Suess and H. C. Urey. Abundances of the elements. *Rev. Mod. Phys.*, 28: 53–74, Jan 1956. doi: 10.1103/RevModPhys.28.53. URL `https://link.aps.org/doi/10.1103/RevModPhys.28.53`.

[11] B. Povh, K. Rith, C. Scholz, F. Zetsche, and W. Rodejohann. *Particles and Nuclei.* Graduate Texts in Physics. Springer Berlin Heidelberg, Berlin, Heidelberg, 2015. ISBN 978-3-662-46320-8. doi: 10.1007/978-3-662-46321-5. URL `http://link.springer.com/10.1007/978-3-662-46321-5`.

[12] A. Coc and E. Vangioni. Primordial nucleosynthesis. *International Journal of Modern Physics E*, 26(8), jul 2017. doi: 10.1142/S0218301317410026. URL `http://arxiv.org/abs/1707.01004http://dx.doi.org/10.1142/S0218301317410026`.

[13] G. Martín-Hernández, P. Mastinu, E. Musacchio González, R. Capote, H. Lubián, and M. Macías. ^{7}Li(p,n)^{7}Be cross section from threshold to 1960 keV and precise measurement of the ^{197}Au(n,γ) spectrum-averaged cross section at 30 keV. *Physical Review C*, 99(3):1–10, 2019. doi: 10.1103/PhysRevC.99.034616.

[14] M. Barbagallo, A. Musumarra, L. Cosentino, E. Maugeri, S. Heinitz, A. Mengoni, R. Dressler, D. Schumann, F. Käppeler, and N Colonna. ^{7}Be(n,α)^{4}He Reaction and the Cosmological Lithium Problem: Measurement of the Cross Section in a Wide Energy Range at n_TOF at CERN. *Physical Review Letters*, 117(15):1–7, 2016. ISSN 10797114. doi: 10.1103/PhysRevLett.117.152701.

[15] L. Damone, M. Barbagallo, M. Mastromarco, A. Mengoni, L. Cosentino, E. Maugeri, S. Heinitz, D. Schumann, R. Dressler, and F. Käppeler. ^{7}Be(n,p)^{7}Li Reaction and the Cosmological Lithium Problem: Measurement of the Cross Section in a Wide Energy Range at n_TOF at CERN. *Phys. Rev. Lett.*, 121:042701, Jul 2018. doi: 10.1103/PhysRevLett.121.042701. URL `https://link.aps.org/doi/10.1103/PhysRevLett.121.042701`.

[16] COSMOS - The SAO Encyclopedia of Astronomy › Stellar Evolution. URL `https://astronomy.swin.edu.au/cosmos/S/Stellar+Evolution`.

[17] Classifying Stars - the Hertzsprung-Russell Diagram. URL `https://www.atnf.csiro.au/outreach/education/senior/cosmicengine/stars_hrdiagram.html`.

[18] J. Emsley. *Nature's building blocks: an A-Z guide to the elements.* 2001.

[19] R. Reifarth, C. Lederer, and F. Käppeler. Neutron reactions in astrophysics. *Journal of Physics G: Nuclear and Particle Physics*, 41(5), mar 2014. ISSN 13616471. doi: 10.1088/0954-3899/41/5/053101. URL `http://arxiv.org/abs/1403.5670http://dx.doi.org/10.1088/0954-3899/41/5/053101`.

[20] K.H. Beckurts and K. Wirtz. *Neutron Physics*. Springer, 1964. URL `https://books.google.it/books?id=ByNRAAAAMAAJ`.

[21] D. Clayton. Principles of stellar evolution and nucleosynthesis. University of Chicago Press, 1983.

[22] Karlsruhe Astrophysical Database of Nucleosynthesis in Stars, April, 2021. URL `https://exp-astro.de/kadonis1.0/`.

[23] Z. Y. Bao, H. Beer, F. Käppeler, F. Voss, K. Wisshak, and T. Rauscher. Neutron cross sections for nucleosynthesis studies. *Atomic Data and Nuclear Data Tables*, 76(1):70–154, 2000. ISSN 0092640X. doi: 10.1006/adnd.2000.0838.

[24] F. Käppeler. Stellar neutron capture rates - Key data for the s process. *EPJ Web of Conferences*, 63, 2013. ISSN 21016275. doi: 10.1051/epjconf/20136303002.

[25] F. Käppeler I. Dillmann, R. Plag and T. Rauscher. KADoNiS v0.3 - The third update of the Karlsruhe Astrophysical Database of Nucleosynthesis in Stars, in EFNUDAT Fast Neutrons, Sci. . *Workshop on Neutron Measurements, Theory, and Applications, edited by F.J. Hambsch*, z:55–58, dec 2010. doi: 10.1088/1742-6596/1643/1/012033. URL `http://www.kadonis.org`.

[26] International Atomic Energy Agency (IAEA), 2021. URL `https://www.iaea.org`.

[27] IAEA, Research Reactor Database (RRDB), 2021. URL `https://nucleus.iaea.org/RRDB/RR/ReactorSearch.aspx`.

[28] Institut Laue-Langevin (ILL), 2021. URL `https://www.ill.eu`.

[29] C. Andreani, I. S. Anderson, J. M. Carpenter, G. Festa, G. Gorini, C. K. Loong, and R. Senesi. Applications of compact accelerator-driven neutron sources: An updated assessment from the perspective of materials research in Italy. In *Physics Procedia*, volume 60, pages 228–237. Elsevier B.V., jan 2014. doi: 10.1016/j.phpro.2014.11.032.

[30] Neutron Generator, January, 2021. URL `https://phoenixwi.com/neutron-generators/`.

[31] IAEA- Spallation sources, January, 2021. URL `https://www.iaea.org/topics/nuclear-science/nuclear-research/accelerators/spallation-sources`.

[32] Interactive Map of Accelerators in the World, 2021. URL `https://nucleus.iaea.org/sites/accelerators/Pages/default.aspx`.

[33] Geel Electron Linear Accelerator (GELINA), 2021. URL `https://ec.europa.eu/jrc/en/research-facility/open-access/relevance-driven/2019-1-rd-eufrat-gelina`.

[34] n_TOF, The neutron time of flight facility at CERN, 2021. URL `https://ntof-exp.web.cern.ch`.

[35] European Organization for Nuclear Research (CERN), 2021. URL `https://home.cern/`.

[36] HISPANoS: pulsed and continuous neutron source at CNA, 2021. URL `https://cna.us.es/index.php/en/facilities/financed-feder-funds/equipments/78-neutron-line`.

[37] Centro Nacional de Aceleradores (CNA), 2021. URL `https://cna.us.es/index.php/en/`.

[38] Legnaro National Laboratories (LNL), 2021. URL `https://www.lnl.infn.it/index.php/en/`.

[39] Collaboration N_TOF. The neutron Time-Of-Flight facility, n_TOF, at CERN (I): Technical Description. (I), 2013.

[40] Neutrons in full flight at CERN's n_TOF facility, March, 2016. URL `https://cerncourier.com/a/neutrons-in-full-flight-at-cerns-n-tof-facility/`.

[41] B. Fernández, M. Macías, C. Guerrero, M. A Millán-Callado, T. Rodríiguez-Gonzalez, J. M. Quesada, J. Gómez-Camacho, and J. Praena. HiSPANoS facility and the new neutron beam line for TOF measurements at the Spanish National Accelerator Lab (CNA). *Journal of Physics: Conference Series*, 1643:12033, dec 2020. doi: 10.1088/1742-6596/1643/1/012033. URL `https://doi.org/10.1088/1742-6596/1643/1/012033`.

[42] Macías, Miguel, Fernández, Begoña, and Praena, Javier. Neutron beam line for tof measurements at the spanish national accelerator lab (cna). *EPJ Web Conf.*, 239:17014, 2020. doi: 10.1051/epjconf/202023917014. URL `https://doi.org/10.1051/epjconf/202023917014`.

[43] F. Käppeler. The origin of the heavy elements: The s process. *Progress in Particle and Nuclear Physics*, 43(March):419–483, 1999. ISSN 01466410. doi: 10.1016/s0146-6410(99)00098-8.

[44] W. Ratynski and F. Käppeler. Neutron capture cross section of Au197: A standard for stellar nucleosynthesis. *Physical Review C*, 37(2):595–604, 1988. ISSN 05562813. doi: 10.1103/PhysRevC.37.595.

[45] C. Lederer, F. Käppeler, M. Mosconi, R. Nolte, M. Heil, R. Reifarth, S. Schmidt, I. Dillmann, U. Giesen, A. Mengoni, and A. Wallner. Definition of a standard neutron field with the 7Li(p,n)7Be reaction. *Physical Review C - Nuclear Physics*, 85(5):1–8, 2012. ISSN 1089490X. doi: 10.1103/PhysRevC.85.055809.

[46] G. Feinberg, M. Friedman, A. Krása, A. Shor, Y. Eisen, D. Berkovits, D. Cohen, G. Giorginis, T. Hirsh, M. Paul, A. J.M. Plompen, and E. Tsuk. Quasi-stellar neutrons from the 7Li(p,n)7Be reaction with an energy-broadened proton beam. *Physical Review C - Nuclear Physics*, 85(5):1–12, 2012. ISSN 1089490X. doi: 10.1103/PhysRevC.85.055810.

[47] M. Macías, B. Fernández, and J. Praena. The first neutron time-of-flight line in Spain: Commissioning and new data for the definition of a neutron standard field. *Radiation Physics and Chemistry*, 168:108538, 2020. ISSN 0969-806X. doi: https://doi.org/10.1016/j.radphyschem.2019.108538. URL `https://www.sciencedirect.com/science/article/pii/S0969806X19302968`.

[48] P. F. Mastinu, G. Martín Hernández, and J. Praena. A method to obtain a Maxwell-Boltzmann neutron spectrum at kT=30 keV for nuclear astrophysics studies. *Nuclear Instruments and Methods in Physics Research, Section A: Accelerators, Spectrometers, Detectors and Associated Equipment*, 601(3):333–338, 2009. ISSN 01689002. doi: 10.1016/j.nima.2009.01.005.

[49] C. Lederer, N. Colonna, C. Domingo-Pardo, F. Gunsing, F. Käppeler, C. Massimi, A. Mengoni, A. Wallner, U. Abbondanno, and G. Aerts. ^{197}Au(n, γ) cross section in the unresolved resonance region. *Phys. Rev. C*, 83:034608, Mar 2011. doi: 10.1103/PhysRevC.83.034608. URL `https://link.aps.org/doi/10.1103/PhysRevC.83.034608`.

[50] C. Massimi, B. Becker, E. Dupont, S. Kopecky, C. Lampoudis, R. Massarczyk, M. Moxon, V. Pronyaev, P. Schillebeeckx, I. Sirakov, and R. Wynants. Neutron capture cross section measurements for 197Au from 3.5 to 84 keV at GELINA. *The European Physical Journal A*, 50(8):124, 2014. ISSN 1434-601X. doi: 10.1140/epja/i2014-14124-8. URL `https://doi.org/10.1140/epja/i2014-14124-8`.

[51] Karlsruhe Astrophysical Database of Nucleosynthesis in Stars, January, 2021. URL `https://exp-astro.de/kadonis1.0/selementquery.php?isotope=197Au`.

[52] R. B. Firestone. Table of Isotopes, eigth ed. March 1996.

[53] Experimental Nuclear Reaction Data (EXFOR) Database Version of 2020-12-19. URL `https://www-nds.iaea.org/exfor/`.

[54] S. G. Mashnik, M. B. Chadwick, H. G. Hughes, R. C. Little, R. E. MacFarlane, L. S. Waters, and P. G. Young. 7-Li(p,n) Nuclear Data Library for Incident Proton Energies to 150 MeV. 2008. URL `http://arxiv.org/abs/nucl-th/0011066`.

[55] C. L. Lee and X.L. Zhou. Thick target neutron yields for the ^{7}Li(p,n)^{7}Be reaction near threshold. Technical report.

[56] H. Liskien and A. Paulsen. ATOMIC DATA AND NUCLEAR DATA TABLES. 15(I):57–84, 1975.

[57] J. F. Ziegler and J. P. Biersack. *The Stopping and Range of Ions in Matter*, pages 93–129. Springer US, Boston, MA, 1985. ISBN 978-1-4615-8103-1. doi: 10.1007/978-1-4615-8103-1_3. URL `https://doi.org/10.1007/978-1-4615-8103-1{_}3`.

[58] J. H. Gibbons and R. L. Macklin. Total Neutron Yields from Light Elements under Proton and Alpha Bombardment. *Physical Review*, 114(2), 1959.

[59] A. Savidou, X. Aslanoglou, T. Paradellis, and M. Pilakouta. Proton induced thick target γ-ray yields of light nuclei at the energy region Ep = 1.0-4.1 MeV. *Nuclear Instruments and Methods in Physics Research, Section B: Beam Interactions with Materials and Atoms*, 152(1):12–18, 1999. ISSN 0168583X. doi: 10.1016/S0168-583X(98)00962-8.

[60] J. F. Ziegler. SRIM - The Stopping and Range of Ions in Matter. URL `http://www.srim.org`.

[61] D.B. Pelowitz. MCNPX Users Manual Version 2.7.0. *LA-CP-11-00438*, 2011.

[62] N. Colonna, A. Tsinganis, R. Vlastou, N. Patronis, M. Diakaki, S. Amaducci, M. Barbagallo, S. Bennett, E. Berthoumieux, M. Bacak, and G. Cosentino. The fission experimental programme at the CERN n_TOF facility: status and perspectives. *European Physical Journal A*, 56(2):1–49, 2020. ISSN 1434601X. doi: 10.1140/epja/s10050-020-00037-8. URL `https://doi.org/10.1140/epja/s10050-020-00037-8`.

[63] F. Mingrone, C. Massimi, G. Vannini, N. Colonna, F. Gunsing, P. Žugec, S. Altstadt, J. Andrzejewski, L. Audouin, and M Barbagallo. Neutron capture cross section measurement of U 238 at the CERN n-TOF facility in the energy region from 1 eV to 700 keV. *Physical Review C*, 95(3):1–14, 2017. ISSN 24699993. doi: 10.1103/PhysRevC.95.034604.

[64] CN accelerator at INFN-LNL. URL `https://www.lnl.infn.it/index.php/en/accelerators-3/cn`.

[65] Behlke website. URL `http://www.behlke.com`.

[66] SCIONIX- Dedicated Scintillation Detectors. URL `https://scionix.nl`.

[67] ET Enterprises electron tubes, ET Enterprises, Ltd. URL `https://et-enterprises.com`.

[68] Evaluated Nuclear Data File (ENDF) . URL `https://www-nds.iaea.org/exfor/endf.htm`.

[69] CAEN Tools for discovery. URL `https://www.caen.it`.

[70] CAEN WaveDump. CAEN Digitizer readout application. URL `https://www.caen.it/products/caen-wavedump/`.

[71] CoMPASS Multiparametric DAQ Software for Physics Applications. URL `https://www.caen.it/products/compass/`.

[72] Electronic Instrumentation. Caen DT5730/DT5725 User Manual. 2020. ISSN 02650096.

[73] P. Forck. Lecture Notes on Beam Instrumentation and Diagnostics. *Joint University Accelerator School*, pages 0–152, 2011.

[74] Physikalisch-Technische Bundesanstalt (PTB) institute. URL `https://www.ptb.de/cms/`.

[75] M. Macias. *HiSPANoS (HiSPAlis Neutron Source) at CNA: installation and commissioning of the first neutron time of flight beamline in Spain*. PhD thesis, 2019.

[76] Goodfellow company. URL `http://www.goodfellow.com/`.